PARTICLE IMAGE VELOCIMETRY IN AN ADVANCED, SERPENTINE JET ENGINE INLET DUCT

A Thesis

by

NATHAN RYAN TICHENOR

Submitted to the Office of Graduate Studies of
Texas A&M University
in partial fulfillment of the requirements for the degree of

MASTER OF SCIENCE

August 2007

Major Subject: Aerospace Engineering

PARTICLE IMAGE VELOCIMETRY IN AN ADVANCED, SERPENTINE JET ENGINE INLET DUCT

A Thesis

by

NATHAN RYAN TICHENOR

Submitted to the Office of Graduate Studies of
Texas A&M University
in partial fulfillment of the requirements for the degree of

MASTER OF SCIENCE

Approved by:

Chair of Committee,	Rodney D.W. Bowersox
Committee Members,	Simon W. North
	Othon K. Rediniotis
Head of Department,	Helen L. Reed

August 2007

Major Subject: Aerospace Engineering

ABSTRACT

Particle Image Velocimetry in an Advanced, Serpentine Jet
Engine Inlet Duct. (August 2007)
Nathan Ryan Tichenor, B.S., Texas A&M University
Chair of Advisory Committee: Dr. Rodney D.W. Bowersox

The overarching objective of this research project was to gain improved basic understanding of the fluid mechanisms governing the development of secondary flow structures in complex, three-dimensional inlet ducts. To accomplish this objective, particle image velocimetry measurements were employed to document the mean and turbulent flow properties within the complex flow regions. Complimentary, surface oil flow visualizations and static pressures were obtained to aid in the interpretation of the PIV data. Using these diagnostic techniques, the formation of a pair of counter-rotating vortices was revealed.

Two-dimensional PIV measurements were conducted along 20 planes near the two bends of the duct model. All data was collected with an incoming freestream of 40 m/s. Over 2000 image pairs were collected for each measurement location, which were then processed and averaged to generate mean velocity, variance intensity, and velocity gradient statistics. The data was analyzed and it was determined that the experimental PIV data corresponded well with the qualitative flow visualization.

This research will contribute to the particle image velocimetry database and subsequent analyses, which will provide additional insight into the flow structure and provide a new database for numerical model validation.

DEDICATION

I dedicate this thesis to my mother, Diane and to all of my family and friends who have guided and supported me throughout my education.

ACKNOWLEDGMENTS

Firstly, I would like to thank my advisor, Dr. Rodney Bowersox for continually guiding me and supporting me throughout my education and research. I also thank my committee members, Dr. Othon Rediniotis and Dr. Simon North, for their support and advice throughout this project

I would also like to thank to my fellow graduate students involved in this project, Aaron Kirk and Abhinav Kumar, as well as Isaac Ekoto whose knowledge of Particle Image Velocimetry proved to be invaluable.

I thank Josh Wiemar, for his help in the fabrication of the many parts during the course of this project.

Finally, I would like to thank Dr. Rhett Jeffries from the Air Force Office of Scientific Research for the generous grant that allowed this research to be possible.

TABLE OF CONTENTS

Page

LIST OF FIGURES

Page

Page

Page

Page

LIST OF TABLES

INTRODUCTION

General

As aerospace systems advance further into the 21st century, the United States military and its allies must improve the stealth capabilities of its aircraft in order to maintain air superiority over the battlefield. Due to improving antiaircraft technology, future warplanes will be designed to minimize their detectability and improve their overall performance[1]. The propulsion systems within these aircraft will be paramount in determining the effectiveness and survivability of the warplanes. In efforts to meet the design criteria of tomorrow, a new breed of inlet ducts are being developed that will improve the stealth characteristics of future aircraft.

This thesis presents a study performed to gain a better understanding of the flow conditions within compact, serpentine jet engine inlet ducts. By using several methods, including a survey of previous literature on the topic, surface flow visualization, wall static tap experiments at various locations, and particle image velocimetry measurements at various locations, the internal flow characteristics of a serpentine jet engine inlet duct was observed. The data gathered from the experiments described in this study are to be used as real world verifications for computational fluid dynamics codes and turbulence models developed for serpentine inlet ducts.

This thesis follows the format of the *AIAA Journal.*

Serpentine Inlet Ducts

Traditional engine intakes create large radar reflections by allowing radar waves to contact the engine face and reflect back out. Serpentine inlet ducts, or S-ducts, however, do not provide a direct line of sight to the compressor blades, thus hiding the engine from incoming radar waves. The radar signal becomes trapped inside the duct and dissipates[1,2]. Because S-ducts are smaller than traditional inlets, they can easily be merged into the airframe to allow a highly integrated system with a lower radar and infrared signature[3,4].

In addition to improving to the overall stealth capabilities of the aircraft, highly compact serpentine inlet ducts allow lightweight, tightly packaged, low volume inlet systems that enable increased aircraft design possibilities[5]. The benefits of using S-ducts are most useful in the design of unmanned aerial vehicles (UAV's) where the size of the aircraft is of the utmost importance and is largely determined by the size of the propulsion system. A scaling analysis performed by engineers at Lockheed Martin showed that reducing duct length by one duct diameter can decrease the empty weight of UAV's by 15%[6]. If the weight of the aircraft can be reduced by using a serpentine inlet duct, then the manufacturing and operating costs of the vehicle will be reduced. This would make the aircraft more economical and attractive for further development.

Although there are size and cost advantages by using serpentine inlet ducts, these ducts generally do not exhibit the aerodynamic qualities necessary to allow optimal engine performance. Ideally, inlets should decelerate incoming flow, minimize pressure loss and provide, clean, uniform air to the compressor blades[7,8]. However, S-ducts typically do not exhibit these properties to acceptable standards. Due to the centerline curvature, serpentine ducts usually generate significant secondary flow structures which lead to large amounts of pressure loss and flow distortion at the engine face[9,10]. These secondary flow structures are characterized by cross flow, a pair of large, counter-rotating vortices and large areas of separation[2,4,6,7,8]. As the core flow negotiates a bend, it accelerates due to a centrifugal force. At the same time, the flow separates in the inner region of the bend, thus producing a pressure gradient where the inner pressure is lower than the pressure at the outside of the bend. Within the boundary layer, this pressure difference creates a transverse or cross-stream flow towards the center of the duct, where the merging flow is pushed away from the wall and back towards the outside of the bend[5,8]. As the cross-stream flow merges, two counter-rotating vortices lift-off of the surface[2,6,8]. An illustration of the development of the secondary flow structures is shown in Figure 1.

Serpentine inlet ducts typically exhibit excessive engine face distortion, pressure loss and turbulence because of the separation and vortical structures created from the cross-stream flow[3,5]. As the pressure gradients are ingested into the engine, the compressor blades must pass through regions with varying flow conditions. These instabilities induce possible vibrations and increased wear that can result in structural fatigue and failure[3]. In the low pressure areas, the compressor blades experience an increased incidence angle which causes the flow to separate. This is called rotor blade aerodynamic stall and usually lowers engine surge and stall limits[3,5,9,10]. Additionally, the flow separation contributes to flow blockage which reduces the pressure recovery at the engine face and therefore reduces the overall engine performance and fuel efficiency[6,8]. A visual and quantitative view of the above discussion regarding secondary flow development is provided below in the Results and Discussion section of this document,

Particle Image Velocimetry

There are several techniques currently being employed to measure instantaneous flow fields in real world applications, including laser speckle velocimetry (LSV), particle image velocimetry (PIV) and holographic particle image velocimetry (HPIV) [11,12,13,14]. In LSV, the velocity field is determined by measuring the velocities of the visible speckles. These speckles are formed when the seeding particle densities are so high that interference from scattering light is visible[15]. From a practical standpoint, PIV and LSV are essentially the same. The same ideas drive both methods; however, because LSV calculates velocities based on groups of particles within the field of view, it is inherently less accurate than PIV. HPIV potentially provides the best solution to volumetric measurements of complex 3-D flows, however, this diagnostic technique is complicated and difficult to implement into complex geometries. Also, a HPIV system was not easily available at the time of this project.

Particle image velocimetry, or PIV, is a well-accepted, modern technique for measuring a wide range of flow properties. Although the concepts of PIV have been around for over twenty years, with recent technological advances, PIV has become more efficient and easier to use[11]. PIV can accurately measure a large range of scales as well as low speed and high speed applications. In the most basic form, PIV is a non-intrusive, planar velocity field diagnostic technique which creates an entire instantaneous velocity field. Tracer particles are illuminated by a light source (usually a laser) and digital cameras record the position of the particles in two successive images. The tracer particles can be as small as one micron in diameter, however they need to accurately follow the flow within the flow field [16,17,18,19,20,21,22,23]. The short time between the images is possible with short pulse lasers and high speed interline transfer cameras. Usually the cameras are double exposed to achieve this [18]. Today, all digital image processing is available using a PC [21]. For planar PIV, a two-dimensional cross correlation of the image intensities produces a correlation map. The correlation map peaks correspond to the average displacement of the pixels within a particular interrogation window. Various filters and correlation techniques can produce more accurate results. Typically, an interpolation function will determine if smaller interrogation windows will improve the results and reduce errors. Several iterations with decreasing interrogation window sizes are common in most PIV applications today. Planar PIV is a valuable technique for 2-D quantitative flow analysis, however, planar PIV has inherent errors. Any velocities out of plane with the laser sheet are measured as error. Only the projection of the true velocity onto the laser plane are measured [24,25,26]. In order to improve upon the accuracy of PIV measurements, stereoscopic particle image velocimetry has been developed and is quickly becoming more commonplace. With increased computing power and technology, two high speed cameras can be coupled together to produce two image pairs. The two images from each camera are then simultaneously processed using a similar cross correlation technique described above. By adjusting the angle between the cameras and the laser sheet thickness, the third component of the velocity field can be calculated within a reasonable error. The accuracy of the method increases as seeding particle density increases[25]. Because of the complex geometry of the duct model, planar PIV was used to determine 2-D velocity fields along specific measurement planes.

Contributions from the Present Study

The specific contributions of this Master's Thesis are the particle image velocimetry database and subsequent analyses, which will provide additional insight into the flow structure and provide a new database for numerical model validation.

EXPERIMENTAL SETUP AND PROCEDURES

In this section, the experimental equipment utilized for this project is described. The features of a serpentine jet engine inlet are discussed, followed by an explanation of the methods used to obtain and manufacture the duct models. Finally, the wind tunnel test facilities are presented with a look at the data acquisition hardware and software.

Compact, Serpentine Jet Engine Inlet Duct

Duct Geometry

For the current project, an axially compact, three-dimensional S-duct was used. This particular duct geometry was designed at Lockheed Martin for use in future next-generation UAV applications, and was the test article of the study reported by Hamstra et al[6]. The inlet model, which can be viewed in Figure 2, features two, approximately 45 degree bends, and an elliptical-to-circular, diffusing exit section. The exit diameter is 25.4 cm and the overall duct length is 63.5 cm, yielding a length-to-diameter ratio (L/D) of 2.5. This inlet duct model is approximately 40-50% scale for a typical UAV. A biconvex entrance section measuring 25.4 cm in length with an aspect ratio of 4 was added upstream of the first bend to simulate the boundary layer development over a fuselage forebody. Also, for smooth ingestion of the ambient air, a bellmouth contraction with an area ratio of 7.4 was implemented. The addition of the bellmouth prevents flow separation over the inlet lip as air enters the duct, therefore producing a more uniform flowfield.

Baseline Duct Model

Initial testing was performed on a baseline duct model donated to the Texas A&M University Aerospace Engineering Department by Lockheed Martin Aeronautics Company in Ft. Worth, Texas. The duct was fabricated through a laser stereo-lithography (SLA) process and consists completely of hardened resin[6]. The model is split into seven modules to accommodate interchangeable configurations. Each module has two flanges that allow them to be bolted together for quick assembly and disassembly of the duct model. Pressure taps incorporated along the centerline of both the top and bottom walls allow surface static pressures to be measured. A photograph of this SLA constructed, resin inlet duct model is shown in Figure 3.

PIV Duct Model

In order to perform the particle image velocimetry measurements, a duct model with optical access was needed. Rebuilding the inlet duct model was chosen over modifying the existing sections due to the difficulty of machining the brittle resin. Also, it was preferred to retain the donated duct model completely intact as a safeguard. Several technologies were considered for the fabrication of the replica, including rapid prototyping by stereo-lithography or fused deposition modeling, computer numerical control (CNC) machining, injection molding, and sheet metal forming. However, because of budget concerns, a more economical method involving fiberglass with wood reinforcement was selected.

To begin the manufacturing process, reusable fiberglass molds were created from the Lockheed Martin duct model. Clear packaging tape was applied to the inner surface of each resin module to create a layer of separation and to prevent the fiberglass epoxy from adhering to the resin walls. Layers of woven fiberglass cloth were then spread over the taped surface and a two-part epoxy compound was brushed into the cloth. To ensure that the shape of the cured fiberglass would hold after being removed from the duct walls, three layers of fiberglass cloth were used. After hardening, imperfections in the fiberglass pieces were repaired with body filler and sanded until smooth. As a finishing step in preparing the molds, several coats of primer were sprayed on the surfaces and wet sanded until a smooth finished was achieved. This process was repeated for the top and bottom surfaces of each module. Then the halves of the molds were joined and plastic extensions for the fabrication of flanges were added. The finished molds are shown in Figure 4.

The focus of the PIV measurements were near the two bends of the duct, where the flow was expected to separate. In order to eliminate any joints near these areas, the PIV duct model was created in larger modules with fewer seams. The fiberglass molds described above were taped together with clear packaging tape to form two larger molds. Wax and polyvinyl alcohol (PVA) release film were then applied to the molds. These products were used to ensure the fiberglass parts would easily separate from the molds. Approximately six layers of fiberglass cloth followed by four layers of unstructured fiberglass matting were applied to the molds. A final layer of fiberglass cloth on top of the matting helped to press all of the fibers of the matting into the resin and provided a more uniform and aesthetically pleasing final surface for the duct model. The PIV duct model was created many layers of fiberglass so that it would be sufficiently strong to endure the pressure forces exerted on the walls without the need for wood supports. Because wood supports were not used, the optical access locations could be created without interference. Wood flanges were integrated into the fiberglass structure to enable the PIV duct model to connect to adjacent sections. Once the fiberglass was allowed to fully cure, the PIV duct model modules were removed from the fiberglass molds. Four fiberglass pieces were created. Two module halves of the PIV duct model are shown in Figure 5 and a completed fiberglass module is shown in Figure 6. The increased number of layers of fiberglass along with added stiffness of the wood flanges proved to make the duct model sufficiently strong. The inner surface of the model was roughly sanded then any imperfections were filled with body filler and sanded smooth.

PIV measurements were wanted near the bends of the duct. In order to allow both camera and laser sheet access to the areas, a simple ray tracing technique was used to determine the necessary window locations. A total of sixteen camera window locations were chosen, eight near each bend. The combination of all of the window locations allowed a wide viewable area near the bends of the duct. CAD drawings of the window locations are show in Figure 7 and Figure 8.

These windows were designed to be 50 mm in diameter and were made of UV fused silica in order to provide excellent optical clarity as well as exhibit excellent environmental durability. Working from the CAD drawings of the inlet duct, window holders were designed in SolidWorks to hold the ten centimeter windows. A

SolidWorks drawing of one of the designed window holders can be seen in Figure 9. The holders featured a conformal inner surface that preserved the inner shape of the duct. Along with the window holders, solid window “blanks” were designed to fill the window holders when they are not being used. All of the rapid prototype parts are shown in Figure 10.

Because of the small size and the complex inner surfaces of the window holders, it was decided to create them using a fused deposition modeling, rapid prototype machine. When the window holders were completed, they were sanded to remove any large distortions. Sixteen 2 ¼” holes were drilled in the predetermined locations in the fiberglass PIV duct model. The two fiberglass modules with the window holders in the correct locations are shown in Figure 11 and Figure 12. The window holders were placed in the proper locations and secured with epoxy. The inner surface of the window holders were sanded smooth to match the inner surface of the duct model and body filler was applied to fill any seams or gaps. The entire assembly was sanded smooth to provide a clean and seamless interface between the fiberglass duct model and each window holder.

To allow laser sheet access to the desired areas of the duct, windows were needed in PIC duct model near the duct bends. The main concern in determining the locations for the laser sheet access windows was the incident angle between the laser sheet and the window. If the angle is too steep, a large percentage of the laser power will simply reflect off the window and therefore not enter the duct. This would increase the difficulty of the PIV measurements. Allowable incident angles were calculated and the final laser sheet access locations were determined. Thin rectangular areas were cut out of the fiberglass in the desired locations and the edges of the cutouts were sanded down to allow the windows to sit flush with the inner surface of the duct. Pieces of 1/8" acrylic were slowly heated with a heat gun and molded to the duct curvature. Several attempts were needed to produce optically clear windows. The final windows were mounted to the fiberglass using epoxy and silicone was applied to the edges of the acrylic to provide an air tight seal.

After the window holders and laser sheet access windows were mounted, the four fiberglass pieces were joined to create two larger sections, each composing of an entire side of the duct model. To allow for a smooth joint, rubber gasket material was first attached to the flanges with spray adhesive and then the flanges were tightly bolted together. Because of the thickness of the gasket material, there was a gap in the inner surface of the duct. Body filler was used to fill in the gap and any other small blemished on the inner surface. The entire inner surface was then sanded smooth to provide seamless surface throughout the entire length of the duct. With the inner surface of the duct model sufficiently smooth, it along with the inner surfaces of the window "blanks" were painted with flat black spray paint to help minimize reflections from the PIV lasers. The outer surfaces of the duct modules as well as the outer surfaces of the window "blanks" were painted blue to match the duct support frame. Rubber gasket material was applied to the long streamwise flanges of one side of the model as well as to the end flanges of both modules. Bolt holes were drilled into the flanges on both modules to ensure proper placement and alignment during assembly. The two modules were attached to each other and mounted to the remaining modules of the duct to ensure the inner surfaces align sufficiently well. With this verified, the PIV duct model construction was complete.

Wind Tunnel Facilities

For testing, the inlet duct models were integrated into an open-circuit, suck-down wind tunnel with a 0.4572 m x 0.4572 m, square cross-section. To connect the circular exit of the inlet duct to the square wind tunnel, a fiberglass diffuser was constructed. Upstream of the diffuser, a rubber pipe coupler was utilized to isolate the duct from vibrations produced by the wind tunnel fan and motor. The coupler was clamped to a steel pipe to which the exit section of the duct was mounted. The pipe rested upon an adjustable pipe stand, thus providing vertical support for the downstream portion of the inlet duct model. To add a rigid brace to the upstream portion of the duct model, a steel frame was designed to be bolted between the flanges of the bellmouth and first entrance modules. The frame legs consisted of two inch by two inch square pipe, and were welded to a quarter-inch steel plate that was machined via CNC to conform to the inner surface of the duct and corresponding hole locations of the flanges. In Figure 13, the serpentine inlet experimental setup is pictured.

Flow through the tunnel was driven by a large, centrifugal blower measuring 0.6096 m in diameter. Maximum velocity through the duct, measured with a Pitot tube in the second entrance module, was approximately 65 m/s. This value corresponds to a

Mach number of 0.19, a Reynolds number based on exit diameter of 1.1×10^6, and a mass flow rate of 3.3 kg/s.

Data Acquisition

Electronic Pressure Scanner

Pressure data was collected through the use of a miniature, 32-port, electrically scanned pressure (ESP) device from Pressure Systems, Inc. The ESP scanner, shown in Figure 14, was used to measure the pressures from the wall static taps. The advantage of this sensor array is the rapid acquisition of all 32 ports. The sensors of the pressure scanner are digitally multiplexed at rates up to 20,000 Hz. Therefore, over 600 samples of the entire array can be obtained every second. Additionally, the ESP features a pneumatically actuated manifold inside the device that connects all 32 sensors to a single port to allow quick and easy calibration. The uncertainty in the pressure measurements obtained by the pressure scanner is 0.019 torr. Special hardware provided by the Aeroprobe Corporation was used to interface with the ESP scanner.

Acquisition Software

Aeroprobe Corporation also supplied software for use with the pressure scanner and associated hardware. This powerful program, called AeroAcquire, allows the user to control the acquisition of pressures from the ESP system or from individual sensors. It also performs automated calibration and, periodically, zero-offset adjustments for the sensors. Within the program, sampling rate and the number of samples can be adjusted, as can the number of ports to address. Unless otherwise stated, all pressure data gathered for this study was done so for 10 seconds at 256 Hz sampling rate. The software can accommodate multiple ESP scanners.

Static Pressure Taps

Surface static pressure can provide a great deal of insight into determining the regions of separated and attached flow. Therefore, the aforementioned pressure taps integrated into both duct models were utilized in determining the nature of the near-wall flow along the center of the duct model. Tygon tubing connected the taps to the ESP pressure scanner, allowing the simultaneous collection of static pressures from the entire top or bottom surface.

Particle Seeding System

The flow through the duct model was seeded using a Rosco 1600 fog machine, shown in Figure 15. This fog machine consumes a maximum of 2.5 liters of fluid per hour and produces particles between 0.25 - 60 microns in size. The machine also features a remote control on a 15 foot cord which allows easy operation from a distance. The control has two settings, a momentary on switch that provides a puff of smoke, and a constant on switch that continually produces smoke. The control has a dial that allows the operator to roughly control the volume of smoke that is produced, however, this did not to produce a constant stream of particles which is needed for accurate PIV measurements.

To improve and regulate the smoke output from the Rosco fog machine, a simple plywood box was constructed s seen in Figure 16. An outlet port was mounted to the side of the box and a flexible plastic hose was clamped to the port. A spreading nozzle was constructed on the end of the hose from thin plywood to allow a more even distribution of particles. The fog machine was placed in the box and all of the seams were sealed with silicone to produce an air tight enclosure. Regulated compressed air was fed into the box, with a maximum input pressure of five psi.

When the fog machine was turned on inside of the pressurized wood box, a constant, even stream of smoke was produced though the thin nozzle opening. The nozzle was mounted to a standard camera tripod to allow the smoke stream to be inserted into the duct flow at any location. With the tripod setup, the PIV experiments could be conducted by one person and guaranteed a constant supply of seeded particles to the area of interest. The seeding delivery system is shown in Figure 17. This flexibility proved to be extremely valuable while taking the PIV measurements.

Particle Image Velocimetry System

For this project, the seeding particles were illuminated in the duct model using a dual port/dual head New-Wave Solo 120XT PIV laser system. This system is designed to provide a highly stable green light source at wavelength of 532 nm for PIV applications. For this system, the maximum energy output is 120 mJ at 532 nm per head, the pulse width is 4 ns with a ± 1 ns jitter and the maximum frequency is 15 Hz. Perpendicular polarization of the beam coming out of Laser 2 was achieved by using a half wave plate made of crystal quartz, designed to differentially retard the phase of a polarized beam. In front of Laser 1 there was a high energy polarizing cube beamsplitter that provided efficient narrowband polarization. This polarizer consists of a pair of precision right-angle prisms optically contacted together and has a damage threshold up to 10 J/cm^2. A high energy mirror was used to reflect Laser 1 into the high energy polarizing cube beamsplitter. After the beams were aligned through the polarizing cube beamsplitter, there were two coincident beams; one with parallel polarization (Laser 1) and the other with perpendicular polarization (Laser 2).

The laser beams were guided into the duct using a 90º bending prism made of BK7 glass with an antireflection (AR) coating. A BK7 focusing lens with a focal length of 500 mm was used to focus the beam so that the waist was located near the bottom of the inner duct surface. A laser sheet that is approximately 10 cm wide and 1 mm thick is formed in the duct model using a BK7 Plano-concave cylindrical lens. The entire PIV laser system is shown in Figure 18.

The cameras used were Cooke Corp. PCO 1600 high dynamic 14bit cooled interline-transfer CCD camera systems with 1600 x 1200 maximum pixel resolution, and the ability to perform image windowing. These systems feature thermo-electrical cooling at -50°C below the ambient which is capable of a maximum dynamic range of 70dB. The image memory is integrated into the cameras enabling image recording at 160MB/s and the image data are transferred to the computer via IEEE 1394 (firewire) camera links. The cameras had an intrinsic delay time of 5.3 μs and a trigger delay time of 200 ns ± 13 ns. The camera triggers, laser Q-switch and laser flashlamps are all controlled by a Quantum Composers Model 9618 pulse generator. The camera frame grabbing software was Camware version 2.13. Nikon 60 mm lenses were used to focus the cameras onto the illuminated particles within the duct model. For this project, only one camera collected data at a time, however, two cameras were mounted in two measurement locations to save setup and calibration time. The camera setup is shown in Figure 19.

In order to reduce reflections from the inner surface of the duct model, the fiberglass was spray painted flat black. Also, a rhodamine dye solution was painted on the inner surface where the laser sheet makes contact with the fiberglass. The purpose of the rhodamine dye is to further reduce wall reflections. The rhodamine solution is shown in Figure 20 and is painted on a piece of aluminum in Figure 21.

When the laser sheet comes in contact with the rhodamine solution, the light is scattered more and wavelength of the reflected light is changed. The reflected energy appears red, thus coupled with a camera lens filter that only passes the wavelength of 532nm (the wavelength of the lasers), most of the reflections are filtered out. The lens filter is shown in Figure 22.

Physical scale of the images was determined using a dot card made of aluminum. The dot card was positioned in the laser sheet prior to each run and an image was taken of the illuminated dot card. In the post processing, the dot card image was used to determine the pixels/mm resolution of each image. The dot card is shown in Figure 23 and Figure 24.

Post Processing

Velocity fields were created by calculating the displacements of particle ensembles from consecutive images using Innovative Scientific Solutions dPIV 32-bit Analysis Code. A three-step adaptive correlation calculation using successive interrogation window sizes of 128×64, 64×32, and 32×16 pixels, respectively, with 50% overlap was used to determine the velocity vectors. In order to enhance the intensity of correlation peaks relative to random noise, a correlation multiplication process filter with all four correlation maps was turned on. A consistency post processing filter and a nearest neighbor dependency filter were also turned on to improve the adaptive correlation calculation during the first and second passes and to eliminate incorrect vectors during the third pass.

First and second order turbulent statistics were created using an in house computer code written with the Matlab software package. This code ensemble averages the velocity vector fields. In order to minimize the effects of fluctuations in total temperature and pressure while the tunnel is running, the program bins the average velocity data and computes the fluctuating velocities relative to the average velocity from in the corresponding bin. The equation for the bin mean velocity is given below, where n is the number of samples per bin, and J_{max} is the total number of bins.

$$\bar{u}_{bin,j} = \frac{1}{n} \sum_{i=(j-1)n+1}^{j \cdot n} u_i, \quad j = 1 \ldots J_{\max} \tag{1}$$

The computed mean velocity is the ensemble average of the *bin* velocity:

$$\bar{u} = \frac{1}{J_{\max}} \sum_{j=1}^{J_{\max}} \bar{u}_{bin,j} \tag{2}$$

And the fluctuating velocity is given as:

$$\begin{gathered} \overline{u'u'} = \frac{1}{N-1} \sum_{i}^{N} \left(u_i - \bar{u}_{bin,j} \right)^2, \\ 1 \le i \le n \Rightarrow j = 1, \ldots, (J_{\max} - 1)n + 1 \le i \le J_{\max} n \Rightarrow j = J_{\max} \end{gathered} \tag{3}$$

$$\begin{gathered} \overline{u'v'} = \frac{1}{N-1} \sum_{i}^{N} \left(u_i - \bar{u}_{bin,j} \right) \left(v_i - \bar{v}_{bin,j} \right), \\ 1 \le i \le n \Rightarrow j = 1, \ldots, (J_{\max} - 1)n + 1 \le i \le J_{\max} n \Rightarrow j = J_{\max} \end{gathered} \tag{4}$$

RESULTS AND DISCUSSION

The primary objective of this study was to identify and quantify internal flow structures in a highly serpentine inlet duct and to provide concise data for CFD comparison. To achieve this goal, surface flow visualizations and planar particle image velocimetry measurements were performed near the two internal bends of the duct on several measurement planes. The procedure for obtaining the data is presented in detail in the above section. The first sub-section below, **Surface Flow Visualization**, describes the qualitative results obtained from the surface flow visualization test runs. The second sub-section, **Surface Static Pressure Taps**, presents the results of the static pressure taps along the centerline of the Lockheed Martin resin duct model. The next sub-section, **Measurement Plane Locations**, presents the measurement plane locations within the duct geometry. The next two sub-sections, **First Bend PIV Results** and **Second Bend PIV Results**, present the particle image velocimetry results from the first and second bend of the duct respectively. Finally, in the **PIV Error Analysis** sub-section, a discussion of the errors associated with the Particle Image Velocimetry measurements is presented.

Surface Flow Visualization

For a qualitative study of the mechanisms governing the secondary flow formation, flow visualization on the walls of the duct model was carried out. A mixture of titanium dioxide, kerosene, mineral oil, and oleic acid was used for this task. The titanium dioxide, a heavy white powder, becomes suspended in the compound and then was painted onto the inner surface of the inlet duct model. When the flow is activated, shear stresses at the wall force the liquid components of the mixture to migrate downstream, leaving behind the tiny particles of titanium dioxide. In Figure 25 and Figure 26, photographs of the first and second bends of the duct, respectively, are shown after undergoing an application of the titanium dioxide compound. The viewpoint of the first bend picture is upstream, looking at the bottom wall. In the second bend photograph, the top wall is the focus from a downstream location. Merging near-wall flow is evident, as are the locations of vortex lift-off points. In the first bend flow visualization photograph, a line indicating the point of flow separation can be seen. A comparison of the two bends indicates that the second bend vortices are much stronger than those of the first bend. This is evident from the thick pooling of liquid at the first bend vortex cores, where too little flow energy exists to pull the mixture off the duct surface.

Surface Static Pressure Taps

Quantifying the formation of secondary flows in this S-duct model began with an experiment involving surface static pressures. Using the data presented in Figure 27, regions of accelerating and decelerating flow were identified, as were areas of flow separation. Both the bottom and top surfaces are represented in the static pressure plot of Figure 27. For spatial reference, the duct geometry was included as the background image of the graph. These static tap tests were run at an inlet Mach number of 0.18 with a Reynolds number of 1.03 x 10^6. In the plot, P_{ref} is the total pressure measured by the Pitot tube located in the second entrance module of the duct.

Measurement Plane Locations

Particle image velocimetry was used to obtain planar flow measurements within the complex duct flow. As mentioned above, the main areas of interest were near the two internal bends of the duct, where large separation and strong flow structures appear. Two sets of optical access windows were positioned near these bends to allow accurate PIV measurements for a wide internal flow area. A numbering system for the window locations was introduced and is presented in Figure 28 and Figure 29. This system was used throughout the project and the results and data are organized by location and plane number.

Based on the observations of the quantitative flow visualization performed on the duct model, symmetrical flow was assumed. This allowed for fewer measurements and greatly reduced the time needed for testing. Because of the assumption, only have of the window locations were used. For the first bend windows set, only locations 1,2,5, and 6 were used to take data. For the second bend windows, only locations 9, 10, 13, and 14 were used. A total of 20 sets of data were taken using the above eight window locations on 15 different measurement planes.

The PIV data was collected along specific planes within the duct flow. The locations of these measurement planes were determined by using a wood template that mounted to an adjoining duct module. Laser burn paper was attached to the template in the area of the laser sheet. When the lasers were activated, they scorched a line into the burn paper. This line was then measured from specific known points on the duct module to determine the exact laser sheet position within the duct geometry. The wood template for the second bend is shown in Figure 30. The location of the PIV measurements is crucial in providing tight, well defined experimental data for CFD code validation.

In order to take measurements near the walls of the duct, several planes were angled slightly. The maximum angle from vertical for any plane was two degrees. The small angles allowed nearly parallel plane comparisons, yet allowed near wall measurements. Each laser measurement plane scribed a line into the laser burn paper located at the centerline of the duct. To describe the location of these laser lines, several reference points were defined for each bend. The reference points are shown in Figure 31. For the first bend measurement planes, the reference points were the top and bottom corners as well as the midpoint of the connecting line. All three of these points correspond to the seam between the fiberglass duct model and the adjoining straight resin duct module. For the second bend measurement planes, a similar concept was incorporated. However, the three reference points were located on the engine face plane at the duct model exit. Table 1 and Table 2 show the distances in centimeters from the various reference points to two characteristic points along each measurement plane's laser line. A sketch of the characteristic laser points is shown in Figure 31. The angle between the measurement plane and the vertical plane is also given in the tables. Again, all distances are along the centerline plane of the duct model.

Measured Quantities

Using the PIV techniques described above, contour plots were produced for both $\overline{u}$ and $\overline{v}$ velocity components. The velocity components were normalized by the reference velocity $\left(1/U_{ref}\right)$, which was the freestream velocity at the duct entrance. For this set of data, the reference velocity was measured to be 40 m/s. The length scales when calculating the data were normalized by a characteristic length, which in this case was the width of the duct along the centerline at the entrance plane. The characteristic length was measured to be 12.25 cm for the given duct geometry. Each plot is presented in an individual window coordinate system, but can be accurately located within the duct based on the measurement plane locations described above. Also from the PIV data, the variance intensities were determined by subtracting the instantaneous velocity fields from the mean velocity field measurements. Contour plots were created by taking the square root of the variance intensities and then normalizing by the reference velocity $\left(1/U_{ref}\right)$. The turbulent stress data were measured using PIV and were normalized by the square of the reference velocity $\left(1/U_{ref}^2\right)$ to create contour plots. Finally, velocity gradient and vorticity contours were created using the PIV data. Using a second order explicit forward differencing scheme, streamwise and transverse velocity gradients of the $\overline{u}$ and $\overline{v}$ velocity components were calculated. From the gradients, the vorticity was calculated. Contour plots of vorticity, $d\overline{u}/dx$, $d\overline{v}/dx$, $d\overline{u}/dy$, $d\overline{v}/dy$, and $d\overline{w}/dz$ were created for each measurement location. All values were normalized by the reference length and the reference velocity described above. It should be noted that the circular areas seen in the contour plots represent the optical window and is the only valid data for each location. The outer colored region does not represent valid data and should be omitted from observation for all plots. For the majority of the shown contour plots, the boundaries between the valid and invalid regions are not clear cut. The boundaries are generally jagged and non uniform do to numerical errors, boundary reflections, and image processing approximations. The invalid regions of the boundaries are typically represented as dark blue or bright red areas and should be omitted from observation. Any large, solid areas of dark blue or bright red within the valid data region are more than likely due to measurement error or numerical error and should also not be considered.

First Bend PIV Results

This sub-section discusses the result from the set of data taken near the first bend of the duct model. In this area of the duct model, a total of seven planes of data were collected. The first plane of data was collected from window location 1 on measurement plane 1 and was just upstream of the first bend. The contour plots from this plane are presented in Figure 32 and Figure 33. Due to several dead pixels on the PIV camera CCD, an area of the flow field contains a large error. This area is seen in the $\overline{u}$ contour plot as a dark blue area near the right edge of the valid data area. This error region should be omitted for all contour plots at this measurement location. The $\overline{u}$ velocity contour plot shows expected results of a nearly uniform velocity field at approximately the same to the incoming freestream velocity. There is only a slight gradient as the flow approaches the first bend. The $\overline{v}$ velocity plot shows velocities an order of magnitude lower than the $\overline{u}$ velocity plot. The variance intensities are less than 5% for the majority of the flow field and the turbulent shear stress and vorticity is negligible. The $d\overline{u}/dx$, $d\overline{v}/dx$ and $d\overline{u}/dy$ values are mostly uniform and near zero, but the $d\overline{v}/dy$ and $d\overline{w}/dz$ plots show an interesting positive and negative formation. The formations are due to the small gradient in the $\overline{v}$ velocity plot.

The second set of data was taken at window location 1 on measurement plane 2. This plane is close to the local horizontal centerline of the duct. The contour plots for this data are presented in Figure 34 and Figure 35. This set of data has more noise around the window boundary, but a large area of valid data is still present. Like the previous set of data, the $\overline{u}$ velocity is nearly uniform and slightly slows as it approaches the first bend. The $\overline{v}$ velocity is much smaller and the variance intensities and turbulent shear stress are nearly zero for the majority of the flow field. The $d\overline{u}/dx$, $d\overline{v}/dx$, $d\overline{u}/dy$, $d\overline{v}/dy$, and $d\overline{w}/dz$ contour plots show very small fluctuations across the window and are fairly uniform.

The next set of data was taken at window location 2 on measurement plane 1. This window location is closer to the center of the duct compared to window location 1. The contour plots of the data are shown in Figure 36 and Figure 37. As with the previous two data sets, the $\overline{u}$ displays a slight gradient as it approaches the first bend. The $\overline{v}$ velocity is practically zero and the variance intensities are less than 2%. The turbulent shear stress, vorticity and all of the gradients plots also show negligible values.

After the qualitative flow visualization was performed, the uninteresting result in this region of the flow was expected. The measurement location is near the center of the duct and should not display any strong flow structures.

The next set of data was taken at window location 2 on measurement plane 2. The plots from this location are presented in Figure 38 and 39. The $\bar{u}$ velocity again shows the gradient seen in the above plots. However, for this location, the gradient is at an angle. Also, the $\bar{v}$ velocity also depicts a weak gradient at an angle. This angular trend is present in all of the contour plots for this location. Despite this interesting aspect, the variance intensities are a maximum of 2.5% of the freestream and the turbulent shear stress and vorticity are nearly zero. The velocity gradients exhibit the same general aspects of previous data sets. Very small fluctuations are present, but for all practical purposes, the gradients are uniform and negligible.

The first set of data located just downstream of the first bend was taken at window location 5 on measurement plane 5. The contour plots from this data set are presented in Figure 40 and Figure 41. Window location 5 is close to the corner of the duct inner wall. Based on the flow visualization described above, the measurement location should be approaching separated flow, but should not necessarily be within the strong flow structures. From the PIV data, it was observed that the flow is fairly uniform and does not exhibit strong gradients. The $\bar{u}$ velocity is more uniform than any previous data set, and the $\bar{v}$ velocity plots show only a slight vertical gradient. Similarly to previous data sets, the variance intensities are a maximum of 2% of the freestream velocity and the turbulent shear stress and vorticity are uniform and nearly zero. Again, all of the velocity gradients display some minor fluctuations, however, these fluctuations are very small and the gradients are negligible.

The next set of data was taken at window location 6 on measurement plane 6, just downstream of the first bend. This location is closer to the middle of the duct than location 5 described above. The contour plots from this data are presented in Figure 42 and Figure 43. Due to the lack of uniform seeding particles throughout the field of view, the lower portion of the contour plots display a large error and do not contain valid data below the y = 25mm line. The remaining portions of the plot however, provide excellent data as expected. It can be easily observed that the $\bar{u}$ velocity accelerates while the $\bar{v}$ velocity decelerates after the first bend. The $\bar{v}$ velocity deceleration could represent the edge of a region with vortices present. In the area nearest the bend, the variance intensities are as high as 12% but quickly dissipate to less than 2% as the flow continues to move away from the bend. The strong change in the variance intensities could be another sign that the left half of the window is in a separated region of the flow, but the right half is not. Near the bend, the turbulent shear stress is at the highest levels yet to be measured. The vorticity contour plot indicates that there are vortices present in the flow. In the contour plots for the gradients, similar signs verify that something interesting in occurring in this area. For this set of data, the upstream half of the window is a region with vortices and separated flow, but the downstream half of the window, the flow is reattached and cleaner. This explanation agrees with all of the contour plots as well as with the initial flow visualizations in the duct model. This window location was designed to allow optical access to the large vortices and separated region after the first bend. It appears that data was taken on the edge of this region.

The last set of data taken near the first bend was at window location 6 on measurement plane 7. The contour plots for this data are presented in Figure 44 and Figure 45. Similarly to the previous data set, the $\bar{u}$ velocity accelerates while the $\bar{v}$ velocity shows a spanwise gradient after the first bend. However, there is not a easily defined transition line between an area of separation and attached flow. The variance intensities show alternating areas of higher and lower intensities that correspond well to the $\bar{u}$ velocity and the $\bar{v}$ velocity plots. The turbulent shear stress plot shows an area of increased stress downstream of the bend. In the vorticity contour plot, displays similar trends as the previous set. The fluctuations are small but signify that there are weaker vortical structures in this plane compared to the previous set. This result can be expected because measurement plane 7 is closer to the center of the duct than plane 6. The gradients for this set of data show fluctuating regions of positive and negative gradient values again verifying that there are vortices and separation in this plane. However, the structures are not as defined as in the previous set.

Second Bend PIV Results

The first data set near the second bend was taken in window location 9 on measurement plane 8. This location is slightly upstream from the second bend and farthest away from the center of the duct, near the corner. The measurement plane is fair near the upper wall of the duct model and the contour plots are shown in Figure 46 and

Figure 47. Around the window border there is significant noise due to surface reflections. Any solid blue or red regions should be ignored. The $\overline{u}$ velocity plot shows a slight acceleration as the flow approaches the second bend. The $\overline{v}$ velocity plot displays a similar trend but is more significant. The variance intensities are nearly uniform and are negligible throughout the viewable area. The turbulent shear stress and vorticity are also very uniform and negligible over the entire area. Additional noise appears in the contour plots for the gradients because of numerical errors. However, from the regions with valid data, the gradients do not display anything interested. All are nearly uniform and very small. There are no significant flow structures at this measurement location.

The next data set near the second bend was taken in window location 9 on measurement plane 11. The plots for this location are shown in Figure 48 and Figure 49. Plane 11 is closer to the center of the duct than plane 8, but most of the plots are similar for the two data sets. The $\overline{u}$ velocity accelerates slightly in a diagonal direction. The $\overline{v}$ velocity also accelerates slightly towards the bend, however most of the field of view is uniform. Both of the variance intensities show an area of lower intensity near the top of the window. This is very near the corner of the duct where the flow is very straight which agrees with the flow visualizations described above. A maximum variance intensity of 6% was measured near the lower portion of the window. The contour plot of the turbulent shear stress displays a streamwise streak of increased shear stress, but the increase is fairly small. A similar pattern is present in the vorticity plot. Most of the gradients are fairly uniform and uninteresting throughout. The $d\overline{v}/dx$ gradient does exhibit the same streak visible in earlier plots. The fluctuation is very small though. Overall, this plane of data is mostly uniform. It appears that the flow is close to freestream in this area.

The next set of data was measured at window location 10 on measurement plane 8 and the resulting plots are presented in Figure 50 and Figure 51. This location is upstream of the second bend, close to the center of the duct. The measurement plane is nearer the bottom wall of the duct. The $\bar{u}$ velocity plot shows a slight deceleration towards the corner of the duct while the $\bar{v}$ velocity contour displays a slight acceleration in the same direction. Very weak gradients are visible in the variance intensities plots as well as in the turbulent shear stress contour. The vorticity plot exhibits a steak of more negative vorticity, however almost the entire window has a negative vorticity. The gradients for this location are uniform throughout the field of view. Based on the plots discussed above, this measurement location has some slight velocity gradients and low fluctuations.

The next set of data was taken at window location 10 on measurement plane 9. This plane is much nearer to the top wall and just upstream of where the flow is predicted to separate. The contour plots from this data set are shown in Figure 52 and Figure 53. The lower right portions of the plots contain a region of invalid data that can be seen in the $\bar{u}$ velocity plot at a dark blue cutout of the circular window of data. This region plots erroneous data and should not be included in analysis. The $\bar{u}$ velocity plot shows a significant acceleration while the $\bar{v}$ velocity contour depicts a deceleration. The variance intensities are on the order of 5% throughout the field of view and the turbulent shear stress is near zero. The vorticity appears to be uniformly zero as well. In the contours for the gradients, small fluctuations appear however there is no discernable pattern that would suggest an area of separation or vorticity. This location displays some minor velocity acceleration but uniform variance intensities.

The next data set was taken at window location 10 on measurement plane 10. Plane 10 is slightly farther from the top than plane 9 is and they are parallel. The plots from this set are presented in Figure 54 and Figure 55. In the lower right portion of the plots, there is an error region caused by a few dead pixels of the camera's CCD. The affected area is easily spotted on the $\overline{u}$ velocity plot as a blue spot in the yellow to red region. This area does not contain valid data for any plot in this data set and should be omitted from observation. When comparing this data set to the previous one, both the $\overline{u}$ and $\overline{v}$ velocity contours are similar except the location of the maximum $\overline{v}$ velocity. The variance intensities are slightly stronger but display a similar pattern within the field of view. The turbulent shear stress and vorticity are both very nearly zero throughout. The velocity gradients all display similar patterns to the previous data set. Small fluctuations are shown in the plots, but do not present any interesting characteristics.

The final set of data upstream of the second bend was taken at window location 10 measurement plane 11. This plane is near the center of the duct and the contour plots are presented in Figure 56 and Figure 57. The $\overline{u}$ velocity shows a vertical gradient which measured higher velocity towards the centerline of the duct. The $\overline{v}$ velocity contour depicts a largely uniform field except a slightly stronger area near the top of the window. Both variance intensities exhibit a gradient from the strongest at top of the window with a maximum of 2.5% and weakest intensities at the bottom of the window. The turbulent shear stress plot shows another vertical gradient with the more negative value at the top of the window. The vorticity and all of the gradients are uniform across the window area and they all are near zero.

The first data set downstream of the second bend was taken at window location 13 on measurement plane 12. The plots from these data are given in Figure 58 and Figure 59. Plane 12 is very near the centerline of the duct. In this set of data, there is n invalid spot within the window area. On the $\overline{u}$ velocity plot, the area can be seen as the small dark blue area within the valid circle of data. This bad data should not be considered. The $\overline{u}$ velocity and the $\overline{v}$ velocity accelerate as the flow exits the bend. This result is similar to the data sets downstream of the first bend. The variance intensities show a gradient as well with the maximum values of 5% of the freestream velocity near the bottom of the window. The turbulent shear stress contour plot displays a fairly uniform field of view while the vorticity plot shows a narrow area of negative vorticity sandwiched by areas of slightly less negative vorticity. This pattern could indicate that some vortical structures may be present. All of the gradients exhibit minor fluctuations, and are fairly uniform over the entire area. Based on the above plots, this measurement location does not look to have captured any interesting flow characteristics.

The next set of data was taken at window location 13 on measurement plane 14. Plane 14 is nearer to the top wall than previous planes. The contour plots from this set of data are shown in Figure 60 and Figure 61 and they seem to present interesting results. The $\bar{u}$ velocity and the $\bar{v}$ velocity plots both exhibit a spanwise gradient with the highest velocities at the top of the window, towards the corner of the duct. An interesting observation of the $\bar{v}$ velocity plot is in the lower right corner of the window, the velocity is very negative, almost 50% of freestream. This very fast spanwise velocity suggests that a strong vortex is present in this location. The optical window locations were determined based on the location of the vortices that were seen in the flow visualization. To this point, it appears that this window location is in the correct location to observe some of these flow structures. The plots of the variance intensities show higher intensities downstream, reaching as high at 18% in some locations. From the contour plots it is easily seen that variance intensities increase as the flow propagates, indicating a separated or vortical region in this area. The areas of highest variance intensities correspond well to the area of large $\bar{v}$ velocity, thus reinforcing the interpretation of a vortex in the flow. The turbulent shear stress plot shows a similar trend to the variance intensities with the highest values downstream. The vorticity plot shows that the vorticity is essentially zero at the far left edge of the observation window, and gradually becomes more negative as the flow exits the second bend. At the far right edge of the window the vorticity is the strongest and suggests separated flow. All of the velocity gradients exhibit similar trends, however the $d\bar{u}/dx$ and the $d\bar{u}/dy$ plots are more closely matching while the $d\bar{v}/dx$ and the $d\bar{v}/dy$ contours agree very well. The $d\bar{u}/dx$ and the $d\bar{u}/dy$ plots show stronger gradient in the upstream portion of the flow. This makes sense because the $\bar{u}$ velocity is fastest in this region. As the flow begins to turn, the $\bar{u}$ velocity becomes much smaller and does not vary much. The $d\bar{u}/dx$ and the $d\bar{u}/dy$ contours pick up on the slowing $\bar{u}$ velocity and show the regions of lower gradients. The opposite is true for the $d\bar{v}/dx$ and the $d\bar{v}/dy$ gradients. As the $\bar{u}$ velocity decreases, the $\bar{v}$ velocity increases thus indicating spanwise flow. The $d\bar{v}/dx$ and the $d\bar{v}/dy$ gradients clearly show increases in the $\bar{v}$ velocity in this region. The $d\bar{w}/dz$ plot shows a negative area on the left side of the window and slightly positive area on the right side. This structure indicates that the flow is not uniform and straight. Some flow characteristics are showing through that prove that the flow is experiencing vortices and separation.

The next set of data was taken at window location 13 on measurement plane 15. The contour plots are presented in Figure 62 and Figure 63. Plane 15 is slightly farther away from the upper surface of the duct wall than plane 14. Many of the same patterns are present in this data set. It should be noted that there are several small areas of invalid data scattered about the lower half of the interrogation window. These areas can be distinguished by the solid blue or red shading that does not coincide with surrounding the surrounding area. The $\bar{u}$ velocity and the $\bar{v}$ velocity contours look very similar to the previous set. The both velocities increase as the flow approaches the corner of the duct while the $\bar{v}$ velocity shows an area strong negative velocity near the bottom right corner of the window. This agrees with the previous data set in suggesting a vortex formation in the area. The variance intensities both show similar trends with higher intensities near the vortex region of the flow, further suggesting the presence of vortices. The turbulent shear stress displays a slightly smaller high stress region than the previous data, but follows the same pattern, as does the vorticity contour plot. All of the gradients follow the same trend as the last set of data, further confirming the location of the interesting flow characteristics. One observation for this data set however, is that the contour areas indicating the vortices are not as strong as in the previous data set. This suggests that this plane is not as enveloped into the vortex region as the previous one.

The first set of data taken at window location 14 was on measurement plane 12. The results from this data set are presented in Figure 64 and Figure 65. The $\bar{u}$ velocity plot shows a similar vertical gradient that is present in several other locations. The highest velocity is near the bottom of the window, closest to the centerline of the duct. The $\bar{v}$ velocity contour exhibits some interesting effects. In the area farthest upstream, the $\bar{v}$ velocity is negative, but in the downstream region it becomes positive. This suggests that the flow is curving, likely due to vortices in the flow. The variance intensities transition from high intensities at the top of the window to slightly lower intensities at the bottom. The intensities range from 11% to 19% everywhere. The Turbulent shear stress contour appears to be fairly uniform throughout the window, as does the vorticity plot. It can be seen that there is a slightly lower vorticity near the center of the duct. The contour plots of the velocity gradients exhibit fairly uniform properties across the entire window area. There are minor fluctuations due to the averaging process. Overall there are some interesting patterns that suggest vortices in the flow, however, the vorticity and velocity gradients do not show this. These results suggest that the measurement plane is too far from the wall to detect the large vortical flow regions.

The next data set was taken at window location 14 on measurement plane 13. The contours are presented in Figure 66 and Figure 67. Plane 13 is close to the upper surface of the duct and is angled 2 degrees from the horizontal plane. This allows the laser sheet to be closer to the wall in the area of interest. The $\bar{u}$ velocity contour shows a slight acceleration near the top of the window and a very small deceleration near the bottom of the window. The $\bar{v}$ velocity contour plot exhibits similar characteristics; however, the regions of different velocities are much larger and well defined. The variance intensities show slight decreasing gradients along the flow. The maximum intensity is 7% of the freestream and occurs near the upstream edge of the window view. The turbulent shear stress depicts a nearly uniform field of view except an area of slightly increased shear stress near the bottom of the interrogation window. The vorticity contour plot shows a alternating pattern of positive and negative regions. This suggests that the flow is separated and experiencing some significant flow structures. The $d\bar{u}/dx$ and the $d\bar{u}/dy$ contour plots show very small fluctuations throughout the window field. Both are close to zero. The $d\bar{v}/dx$ and the $d\bar{v}/dy$ gradients are also mostly close to zero, however they do show a moderate area of increased activity. These areas correspond to the defined fluctuations in the $\bar{v}$ velocity contour plot discussed above. The $d\bar{w}/dz$ shows an alternating pattern of positive and negative regions along the lines of the vorticity plot. This further suggests that the flow is rolling over the bend and separating.

The next data set was taken at window location 14 on measurement plane 14. The contour plots are presented in Figure 68 and Figure 69. Plane 14 is closer to the wall than plane 13 and it is not angled with respect to the horizontal plane. Most of the contour plots from this set correspond well with the plots from the previous data set. The areas of weak and strong velocities are magnified and larger in this set. The variance intensities show larger regions of low intensity compared to the previous data set while the turbulent shear stress contour plot shows a larger high shear stress region in the bottom half the window field of view. The vorticity plot is almost identical to the previous data set. The plots of the velocity gradients correlate very well with the plots from the previous set, however, it appears that the high and low points are accentuated in the current set. By combining the results from these two data sets, there is strong evidence that the flow is experiencing some separation and vorticity after the second bend of the duct.

The final set of data near the second bend of the duct was taken at window location 14 on measurement plane 15. This plane is closer to the centerline of the duct than the previous two planes and therefore should generally exhibit more uniform flow. The contour plots are presented in Figure 70 and Figure 71. The $\bar{u}$ velocity contour plot shows a pattern similar to the previous two data sets, however the maximum velocity is less than before. The $\bar{v}$ velocity contour plot shows a nearly uniform field that is very close to zero. This suggests that the flow along this plane is generally in the streamwise direction. The variance intensities show a semi-uniform are with a maximum intensity of 5.5% and a minimum of 3%. It appears to be a smooth transition across the field of view. The turbulent shear stress contour plot depicts a nearly uniform region with a small negative area near the top of the window and a smaller high area near the bottom. Both of these areas may be attributed to numerical error generated from the cross correlation algorithm used to process the PIV images. The vorticity contour plot contains a thin streak of negative vorticity similar to the previous two data sets. However, this streak is less well defined. It could suggest a weak three dimensionality in the flow characteristics. Like the vorticity, the velocity gradients display similar patterns to the gradients from the previous two data sets. In this set though, the gradients are more uniform and more near zero than before. The trends are the same but on a much smaller scale. The evidence provided by the contour plots for this data set suggest that the measurement plane is located outside of the strong separated region and is closer to the centerline flow region.

PIV Error Analysis

There are two types of error associated with measurement of instantaneous velocity fields: experimental and experimenter. For particle image velocimetry, experimental errors include correlation mapping error and the conversion error resulting from the conversion of pixel spacing to dimensional measurements. These errors have been estimated to be approximately 1%. Experimenter error is a result of the experimental data collection techniques. For particle image velocimetry, common experimenter errors include non-uniform seeding density, laser reflections, window glare, and seeding fluid accumulation on the windows. Unlike experimental error, experimenter errors cannot be quantified. However, post-processing filtering accounted for most of this error. The filters did reduce the total number of vectors per run is instances. Therefore all error analysis estimates are assuming a low number of valid samples. A complete error analysis for this PIV system was performed by Ekoto[58]. The estimator variances and PIV propagation error values are presented in Table 3 and Table 4 respectively.

CONCLUSIONS AND RECOMMENDATIONS

Within this final section, a summary of the results obtained in this document will be presented. Conclusions will be derived from the work, and a set of recommendations for future efforts relating to the research project will be discussed.

Conclusions

A study was performed to gain an understanding of the development of the secondary flows within a compact, serpentine inlet. Several methods of analysis were employed to characterize the flow mechanics before an investigation was launched to determine the effects of various flow control technologies on the duct performance. The advantages provided by S-shaped inlets include reduced radar cross-section and smaller, lighter, and cheaper air vehicles. The benefits of this study could allow future unmanned aircraft to incorporate this type of jet engine inlet without sacrificing fuel efficiency, engine performance, and longevity.

The main focus of the particle image velocimetry aspect of this project was to gain a quantitative understanding of the complex flow properties within a highly compact, serpentine inlet as well as to provide tight, well defined experimental data for computational fluid dynamics code validation. An inlet duct model was constructed using fiberglass to closely match a duct model provided by Lockheed Martin. Based on flow visualization experiments it was determined that the flow separates around the bends of the duct and creates strong vortices. With this in mind, a particle image velocimetry experiment was devised to measure the flow field near these separation areas. A series of optical access windows were mounted into the fiberglass model near the two bends. A particle seeding delivery system was constructed to inject a steady stream of tracer particles into the flow in specific locations for PIV measurements. Using a well-known planar PIV technique, instantaneous velocity fields were captured in 20 locations and planes just upstream and downstream of the two bends. All data was collected with an incoming freestream of 40 m/s. Over 2000 image pairs were collected for each measurement location, which were then processed and averaged to generate mean velocity, variance intensity, and velocity gradient statistics.

The data was analyzed and it was determined that the experimental PIV data corresponded well with the qualitative flow visualization. Prior to the first bend, the flow is fairly uniform and clean, traveling near the freestream velocity. However, after the first bend, the flow separated and vortices were created. This was seen in the PIV data taken after the first bend. The variance intensities showed significant increases, the vorticity displayed positive and negative regions, and the velocity gradients depicted both streamwise and spanwise acceleration. Just upstream of the second bend, the flow is fairly clean again. After the second bend, the measured quantities again showed that the flow was separated and that vortices were present. All of the PIV results were as predicted and will be a valuable reference for future computational fluid dynamics code validation.

Recommendations

Throughout the course of this project, several observations were made that could possibly improve upon the results. Firstly, the duct model should be created using a process more accurate than fiberglass. The fiberglass duct worked for this project, but it added many hours of additional work to create sufficiently smooth inner surfaces, seams and joints. Even then, it was created by hand to the highest accuracy possible and it did not exactly match the resin duct model provided by Lockheed Martin.

A more reliable particle seeding system should be developed to allow a broader distribution of tracer particles. The system that was constructed for this project proved to be a huge improvement over the stand alone fog machine. However, the output was limited to a small area and it was difficult at times to achieve a sufficient particle seeding density in the area of measurement. A more robust deliver system would speed up testing and improve the results.

In this project, flat windows were used to gain optical access to the flow within the duct. By being constrained to a few discrete access locations, only limited measurement planes could be captured. For future projects, considerations to make a full duct module out of a transparent material would be beneficial and highly versatile in performing measurements on a wide range of planes.

Finally, because the flow within the duct is highly complex and three dimensional, stereoscopic particle image velocimetry would be a valuable option for future work. Stereoscopic particle image velocimetry would allow the third velocity component to be calculated within a reasonable error and would greatly reduce the inherent error present in the other two velocity components. SPIV would provide another set of experimental data that could be used to validate computational fluid dynamics codes.

REFERENCES

[1] Fulghum, D. A., “Stealth Retains Value, But It’s Monopoly Wanes,” *Aviation Week & Space Technology*, Vol. 154, No. 6, pp 53, February 2001.

[2] Tormalm, M., “Design and Analysis of Compact UAV Ducts,” AIAA Paper 2006-2828, June 2006.

[3] Anabtawi, A. J., Blackwelder, R. F., Lissaman, P. B. S. and Liebeck, R. H., “An Experimental Study of Vortex Generators in Boundary Layer Ingesting Diffusers with a Centerline Offset,” AIAA Paper 99-2110, June 1999.

[4] Anabtawi, A. J., Blackwelder, R. F., Liebeck, R. H. and Lissaman, P. B. S., “Experimental Investigation of Boundary Layer Ingesting Diffusers of a Semi-Circular Cross Section,” AIAA Paper 98-0945, January 1998.

[5] Tindell, R. H., “Highly Compact Inlet Diffuser Technology,” *Journal of Propulsion*, Vol. 4, No. 6, pp 557-563, 1988.

[6] Hamstra, J. W., Miller, D. N., Truax, P. P., Anderson, B. A. and Wendt, B. J., “Active Inlet Flow Control Technology Demonstration,” ICAS Paper 2000-6.11.2, August 2000.

[7] Wellborn, S. R., Reichert, B. A., and Okiishi, T. J., “An Experimental Investigation of the Flow in a Diffusing S-Duct,” AIAA Paper 92-3622, July 1992.

[8] Reichert, B. A. and Wendt, B. J., “Improving Diffusing S-Duct Performance by Secondary Flow Control,” AIAA Paper 94-0365, January 1994.

[9] Anderson, B. H. and Gibb, J., “Study on Vortex Generator Flow Control for the Management of Inlet Distortion,” *Journal of Propulsion and Power*, Vol. 9, No. 3, pp 422-430, 1993.

[10] Anderson, B. H. and Gibb, J., “Vortex-Generator Installation Studies on Steady-State and Dynamic Distortion,” *Journal of Aircraft*, Vol. 35, No. 4, pp 513-520, 1998.

[11] Willert, C. E., and Gharib, M., “Digital Particle Image Velocimetry,” *Experiments in Fluids*, Vol. 10, pp 181-193, 1991.

[12] Meng, H., Pan, G., Pu, Y., and Woodward, S. H., “Holographic Particle Image Velocimetry: From Film to Digital Recording,” *Measurement Science and Technology*, Vol. 15, pp 673-685, 2004.

[13] Alcock, R. D., Garner, C. P., Halliwell, N. A. and Coupland, J. M., “An Enhanced HPIV Configuration for Flow Measurement Through Thick Distorting Windows,” *Measurement Science and Technology*, Vol. 15, pp 631-638, 2004.

[14] Adrian, R. J., “Twenty Years of Particle Image Velocimetry,” *Experiments in Fluids*, Vol. 39, pp 159-169, 2005.

[15] Qian, M., Liu, J., Yan,M., et.al, “Investigation on Utilizing Laser Speckle Velocimetry to Measure the Velocities of Nanoparticles in Nanofluids,” *Optics Express*, Vol. 14, No. 17, 2006.

[16] Sinha, S. K., “Improving the Accuracy and Resolution of Particle Image or Laser Speckle Velocimetry,” *Experiments in Fluids*, Vol. 6, pp 67-68, 1988.

[17] Lawson, N. J., and Wu, J., “Three-Dimensional Particle Image Velocimetry: Error Analysis of Stereoscopic Techniques,” *Measurement Science and Technology*, Vol. 8, pp 894-900, 1997.

[18] Willert, C., “Stereoscopic Digital Particle Image Velocimetry for Application in Wind Tunnel Flows,” *Measurement Science and Technology*, Vol. 8, pp 1465-1479, 1997.

[19] Willert, C., Raffel, M., Kompenhans, J., Stasicki, B., and Kahler, C., “Recent Applications of Particle Image Velocimetry in Aerodynamic Research,” *Flow Measurement and Instrumentation*, Vol. 7, No. ¾, pp 247-256, 1996.

[20] Yoon, J.-H. and Lee, S.-J., “Direct Comparison of 2D PIV and Stereoscopic PIV Measurements,” *Measurement Science and Technology*, Vol. 13, pp 1631-1642, 2002.

[21] Lawson, N. J., and Wu, J., “Three-Dimensional Particle Image Velocimetry: Experimental Error Analysis of a Digital Angular Stereoscopic System,” *Measurement Science and Technology*, Vol. 8, pp 1455-1464, 1997.

[22] Huang, H. T., Fiedler, H. E., and Wang, J. J., “Limitation and Improvement of PIV,” *Experiments in Fluids*, Vol. 15, pp 168-174, 1993.

[23] Roesgen, T., and Totaro, R., “Two-Dimensional On-Line Particle Imaging Velocimetry,” *Experiments in Fluids*, Vol. 19, pp 188-193, 1995.

[24] Andres, N., Arroy, M. P., Zahn, H., Hinrichs, H., “Application of Digital Speckle Pattern Interferometry for Fluid Velocimetry in Wind Tunnel Flows,” *Experiments in Fluids*, Vol. 30, pp. 562-567, 2000.

[25] Hart, D. P., “PIV Error Correction,” *Experiments in Fluids*, Vol. 29, pp 13-22, 2000.

[26] Arroyo, M. P., and Greated, C. A., "Stereoscopic Particle Image Velocimetry," *Measurement Science and Technology*, Vol. 2, pp 1181-1186, 1991.

[27] Ekoto, I., "Supersonic Turbulent Boundary Layers With Periodic Mechanical Non-Equilibrium," PhD Dissertation, Aerospace Engineering Department, Texas A&M University, College Station, TX, May 2000.

APPENDIX A

Table 1: First Bend Measurement Plane Locations

	Point 1			Point 2			
Plane	**Top (cm)**	**Middle (cm)**	**Bottom (cm)**	**Top (cm)**	**Middle (cm)**	**Bottom (cm)**	**Angle (deg)**
1	5.10	3.35	8.45	15.50	12.85	12.75	0
2	7.20	3.50	6.85	16.50	13.30	12.50	2
3	8.05	2.30	4.60	17.40	13.15	10.95	2
4	8.55	2.60	3.85	18.65	14.50	12.10	0
5	13.85	10.90	11.00	22.85	19.50	17.65	0
6	13.30	8.40	6.30	26.10	21.65	18.20	0
7	13.40	9.10	7.75	23.50	19.30	16.35	1

Table 2: Second Bend Measurement Plane Locations

	Point 1			Point 2			
Plane	**Top (cm)**	**Middle (cm)**	**Bottom (cm)**	**Top (cm)**	**Middle (cm)**	**Bottom (cm)**	**Angle (deg)**
8	32.15	24.70	22.65	38.65	33.65	33.20	0
9	26.80	21.30	22.70	36.25	33.30	35.20	0
10	28.45	22.90	23.75	36.60	33.35	34.75	0
11	30.09	24.05	23.00	38.20	33.90	33.90	2
12	26.85	19.60	19.35	34.70	29.55	29.40	2
13	23.50	17.40	19.50	33.00	29.10	30.04	2
14	23.10	17.50	20.10	33.50	30.10	31.85	0
15	24.00	17.80	19.60	33.70	29.75	31.00	0

Table 3: Estimator Variances Multiplied by N and Maximum Interval[27]

Statistic	Variance	Maximum Interval
$\overline{u}$	$\overline{u'u'}$	±1.0%
$\sqrt{\overline{u'^2}}$	$\frac{\overline{u'^2}}{2}$	±1.0%
$\sqrt{\overline{v'^2}}$	$\frac{\overline{v'^2}}{2}$	±4.4%
$\overline{u'v'}$	$\left(\overline{u'u'}\right)\left(\overline{v'v'}\right)+\left(\overline{u'v'}\right)^2$	±8.0%

Table 4: PIV Propagation Error Values[27]

Variable	% Error
$d\bar{u}/dx$	1.9%
$d\bar{u}/dy$	1.9%
$d\bar{v}/dx$	3.1%
$d\bar{v}/dy$	3.1%

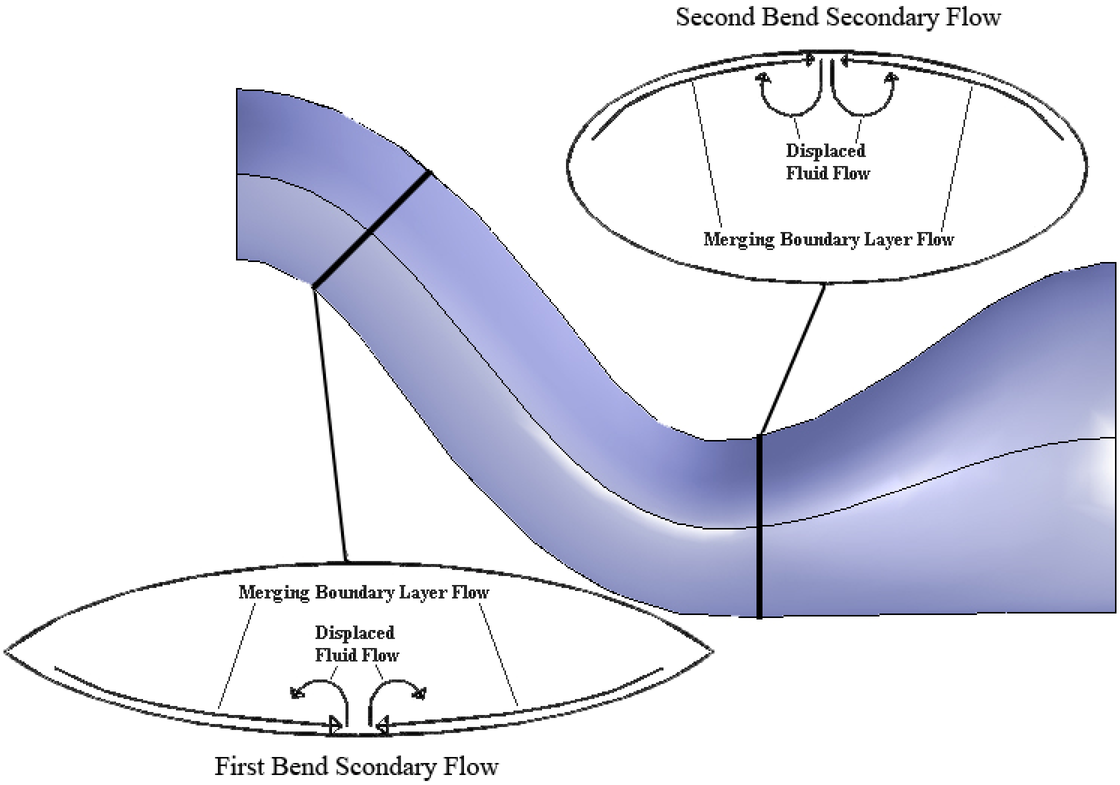

Figure 1: Secondary Flow Development at the Bends of a Serpentine Jet Inlet Duct

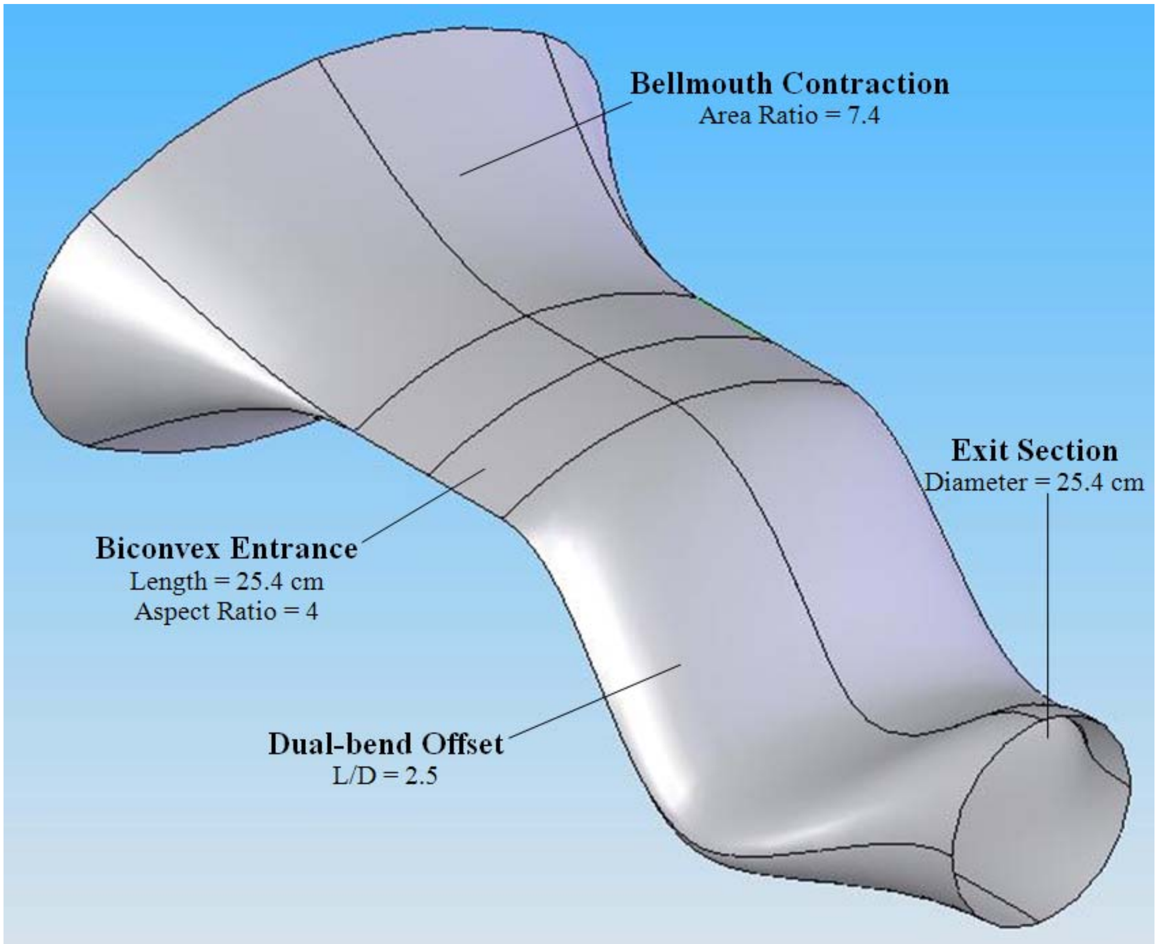

Figure 2: Geometry of the Compact, Serpentine Inlet Model Used in This Study

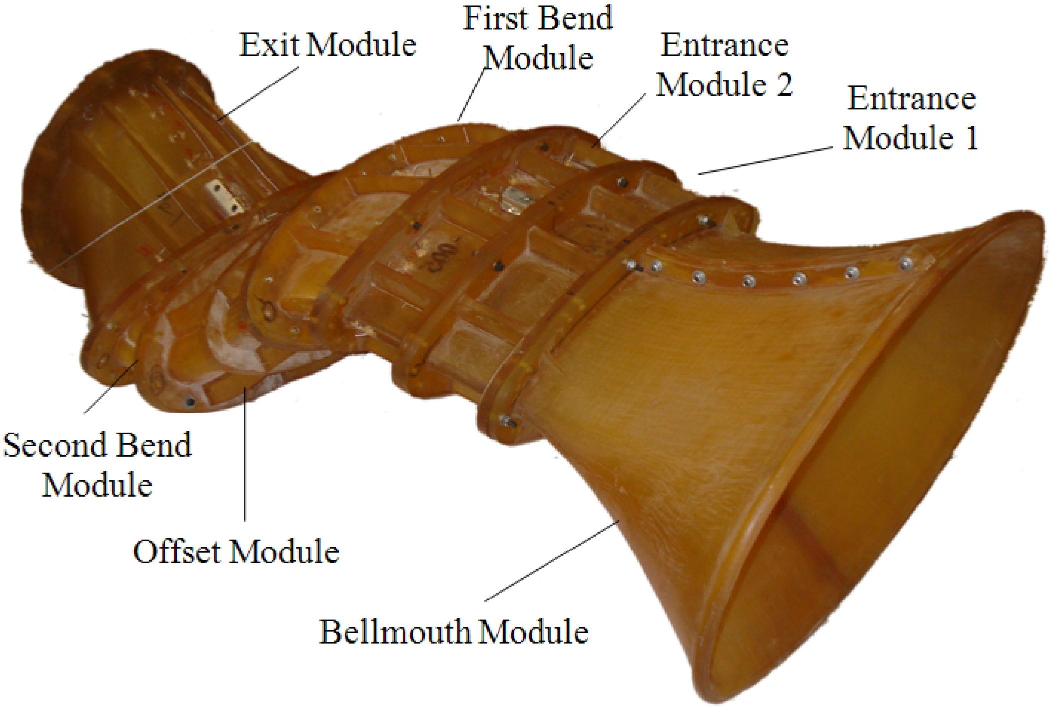

Figure 3: Baseline Duct Model

Figure 4: Molds Employed to Create Fiberglass Reproductions of the Inlet Duct

Figure 5: Fiberglass Module halves of the PIV Duct Model

Figure 6: Complete Fiberglass Module of the PIV Duct Model

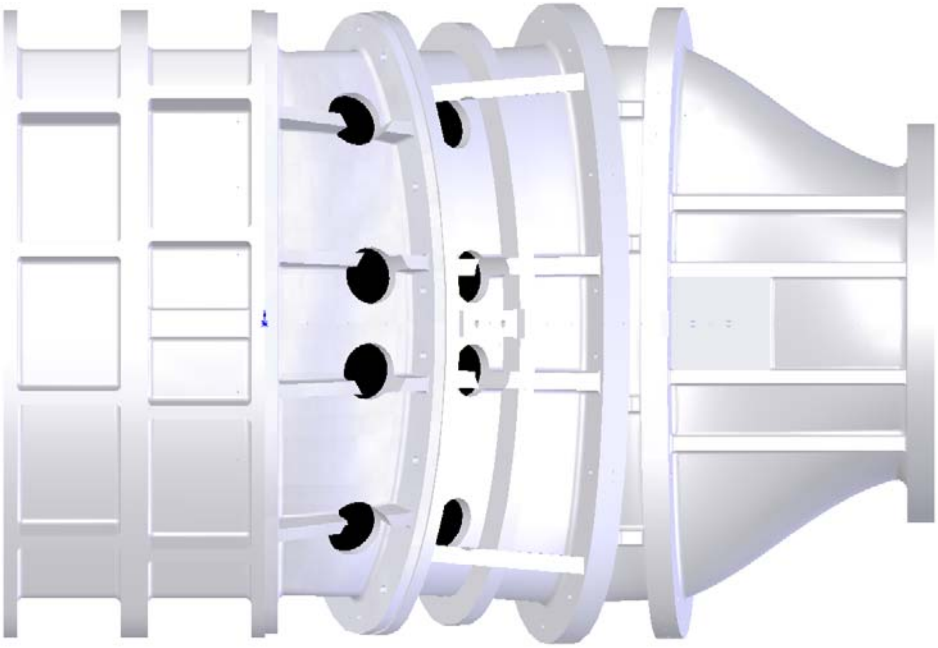

Figure 7: SolidWorks Drawing of First Bend Window Locations

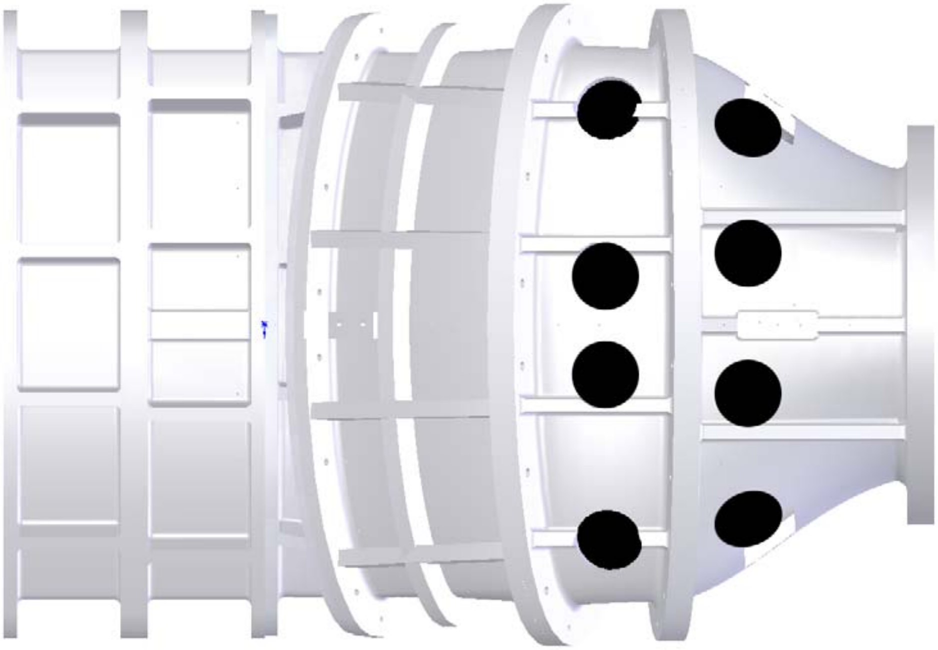

Figure 8: SolidWorks Drawing of Second Bend Window Locations

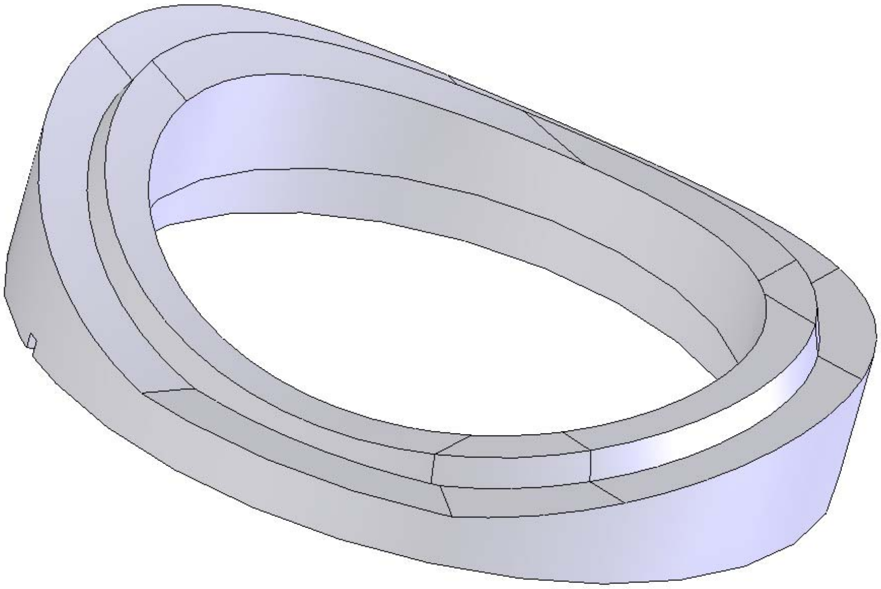

Figure 9: SolidWorks Drawing of a Window Holder

Figure 10: Rapid Prototype Window Holders and Window "Blanks"

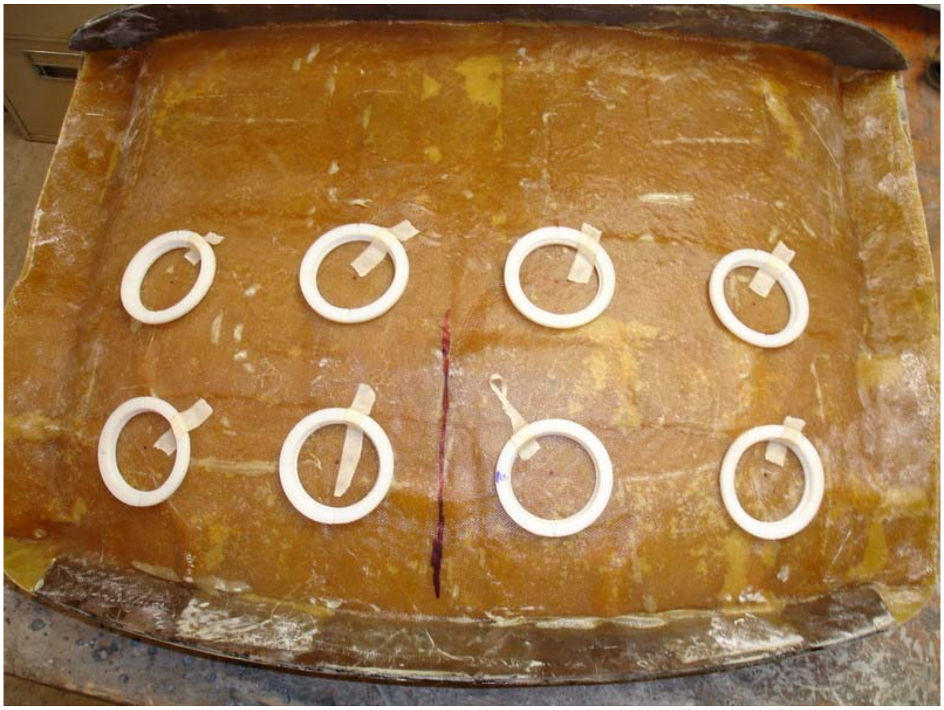

Figure 11: First Bend Window Holder Locations

Figure 12: Second Bend Window Holder Locations

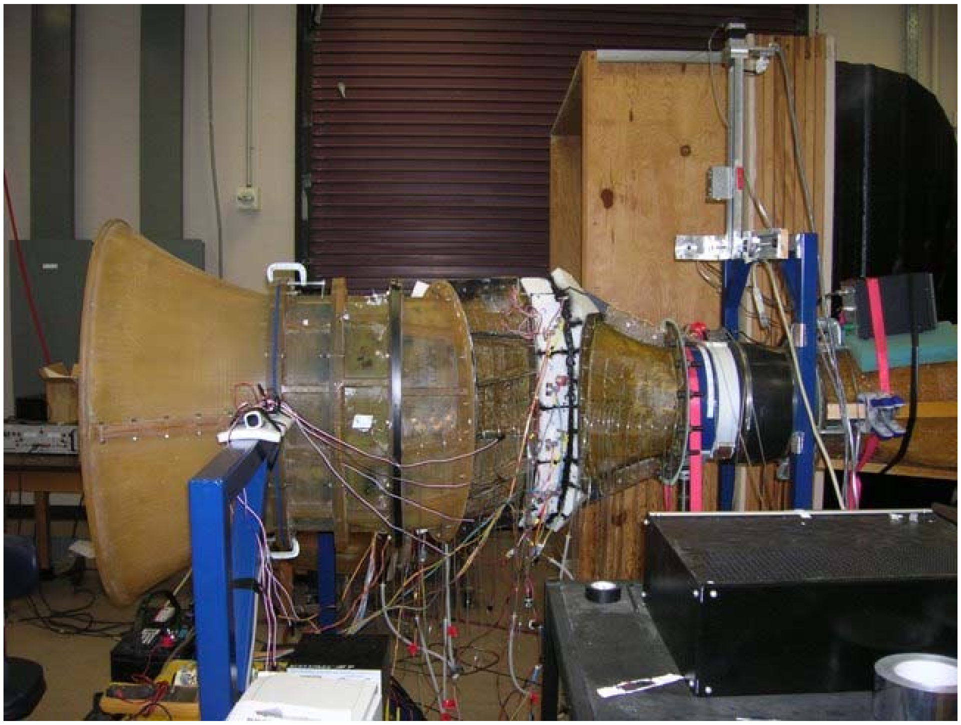

Figure 13: Experimental Setup for Duct Testing

Figure 14: ESP Pressure Scanner for the Rapid Acquisition of Multiple Pressures

Figure 15: Rosco 1600 Fog Machine

Figure 16: Plywood Fog Machine Enclosure

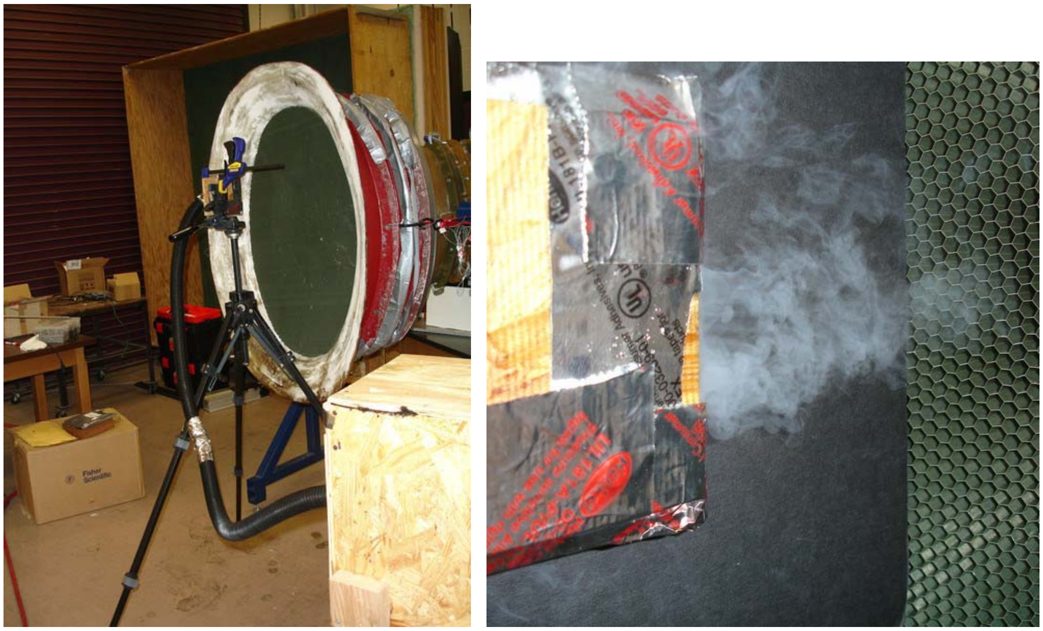

Figure 17: Plywood Fog Machine Enclosure and Seeding Delivery System

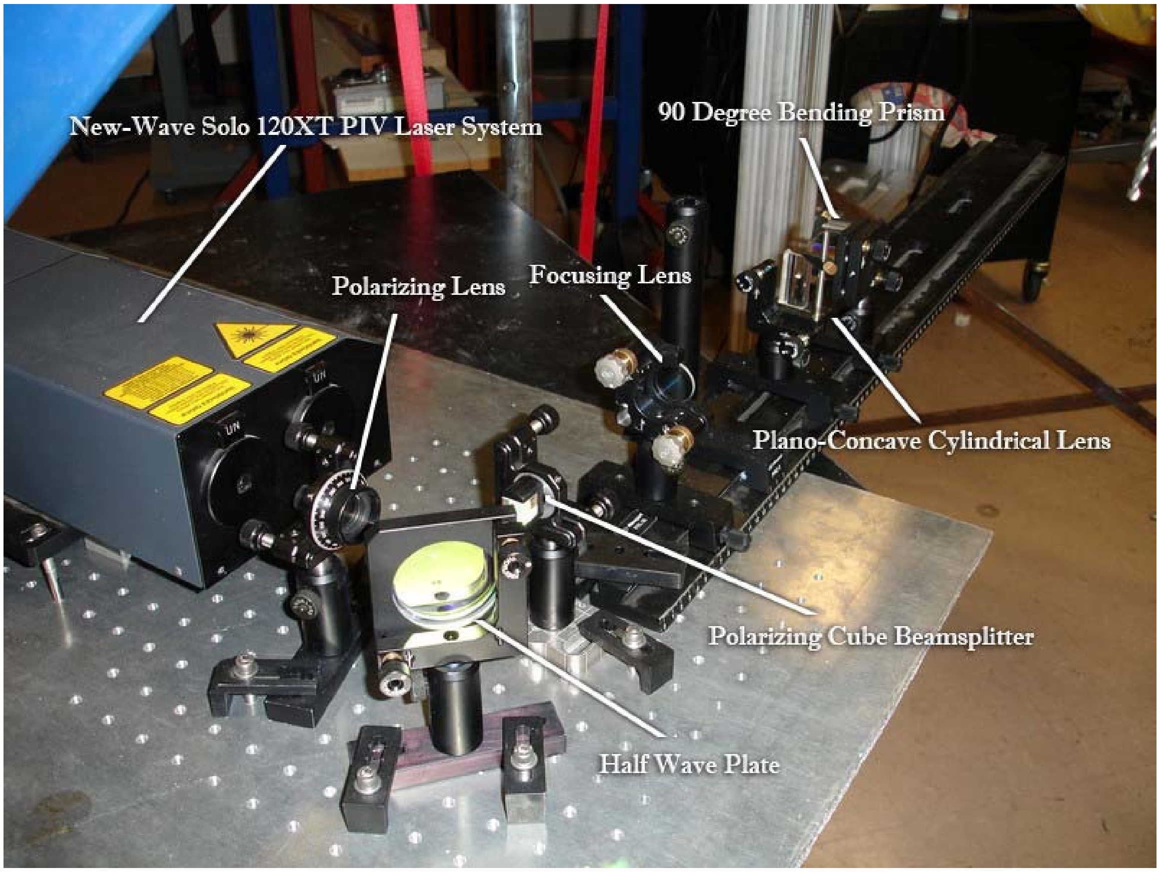

Figure 18: PIV Laser System Configuration

Figure 19: PIV Camera System Configuration

Figure 20: Rhodamine Dye Solution

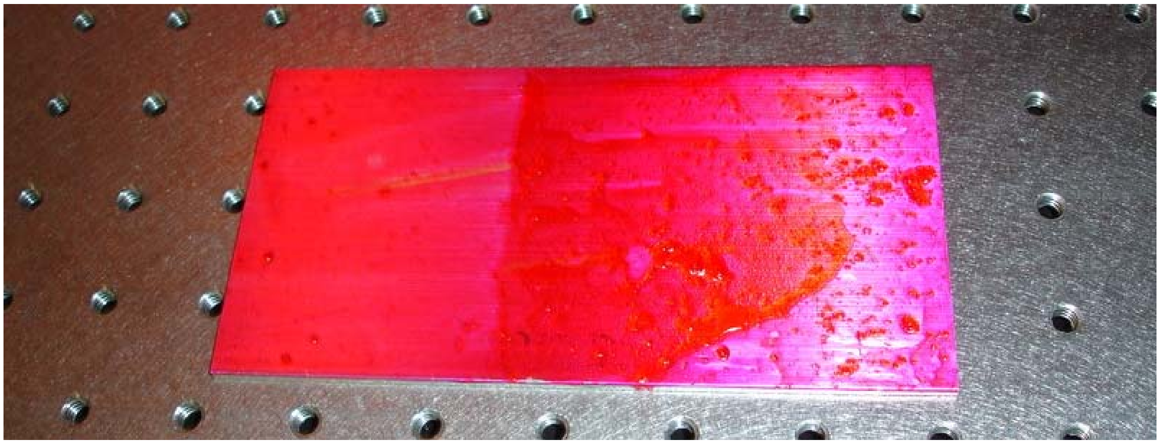

Figure 21: Rhodamine Dye Painted on Aluminum

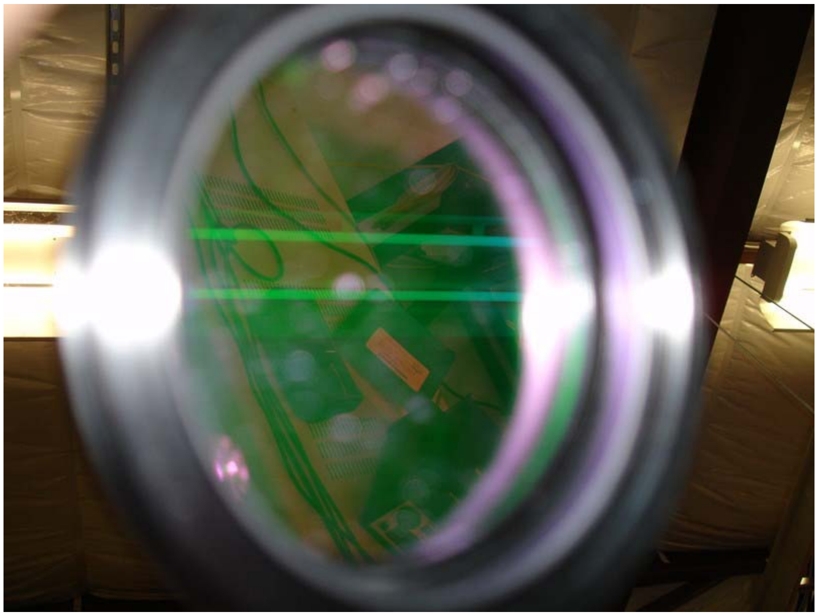

Figure 22: 532nm Camera Lens Filter

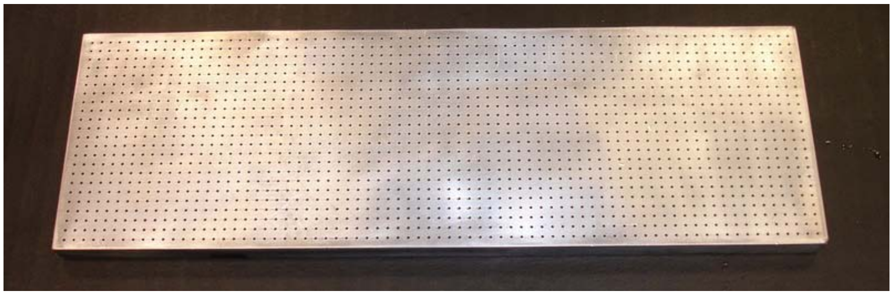

Figure 23: Aluminum Dot Card

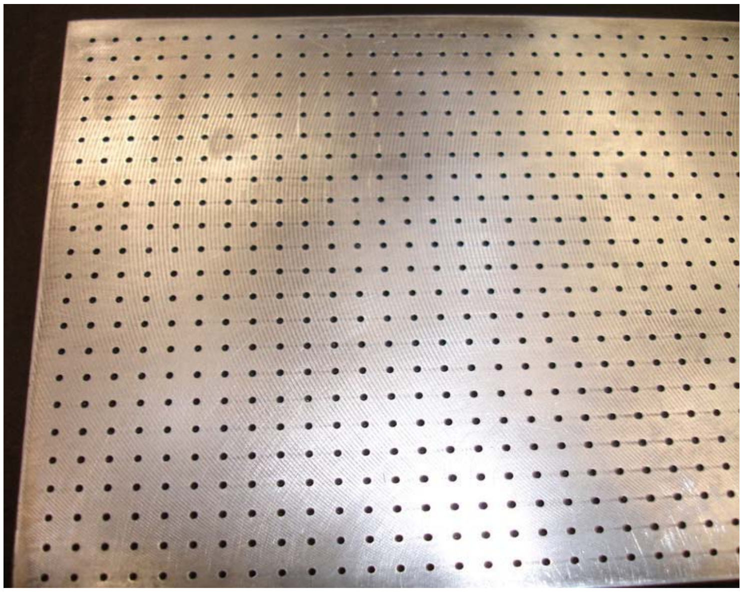

Figure 24: Close Up of Aluminum Dot Card

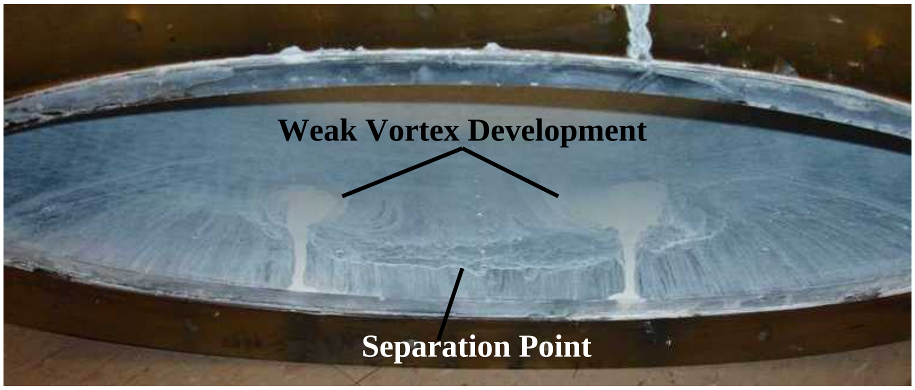

Figure 25: First Bend Surface Flow Visualization

Figure 26: Second Bend Surface Flow Visualization

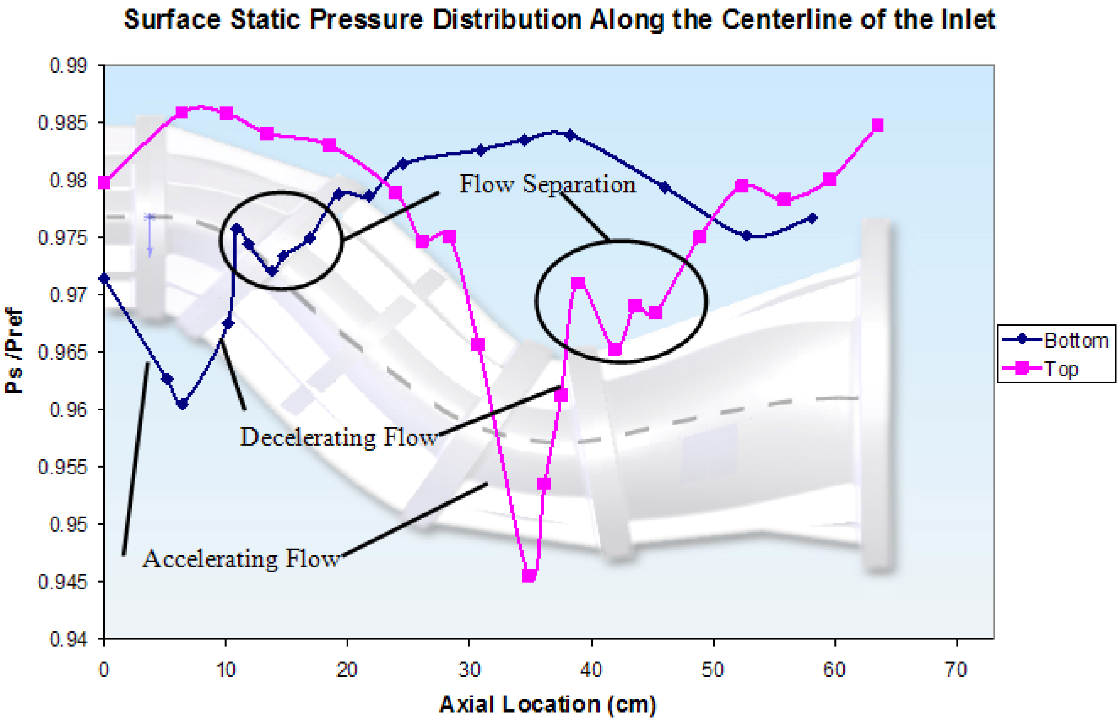

Figure 27: Wall Static Pressures of the Baseline Duct Model

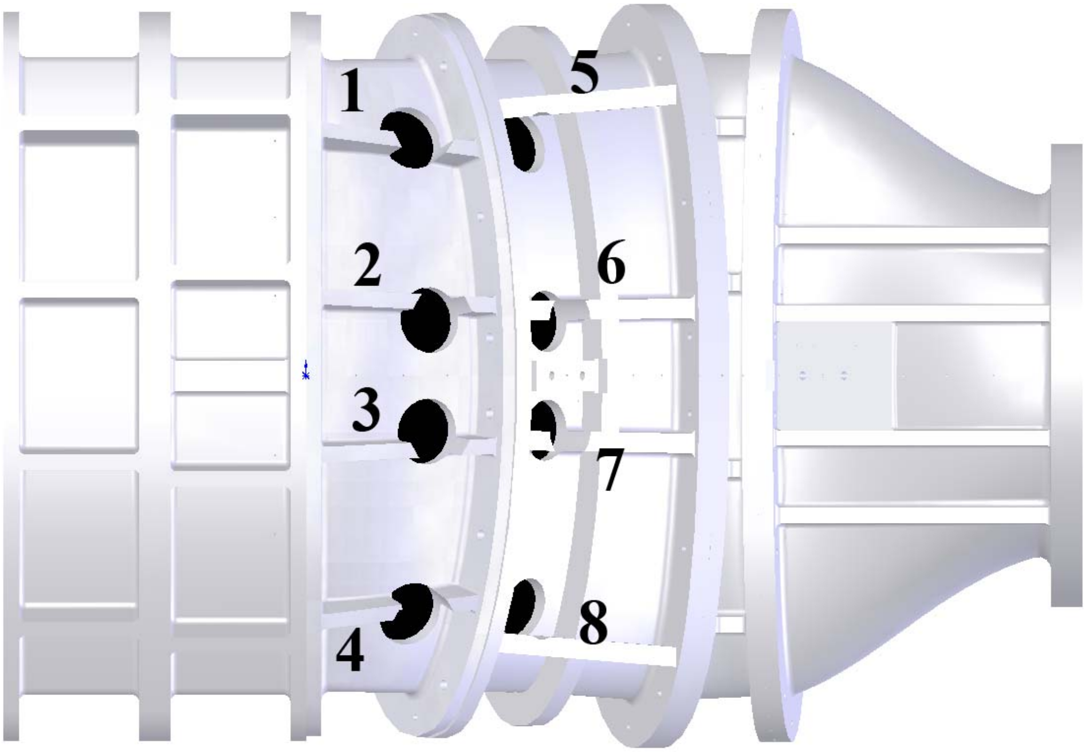

Figure 28: First Bend Window Location Numbers

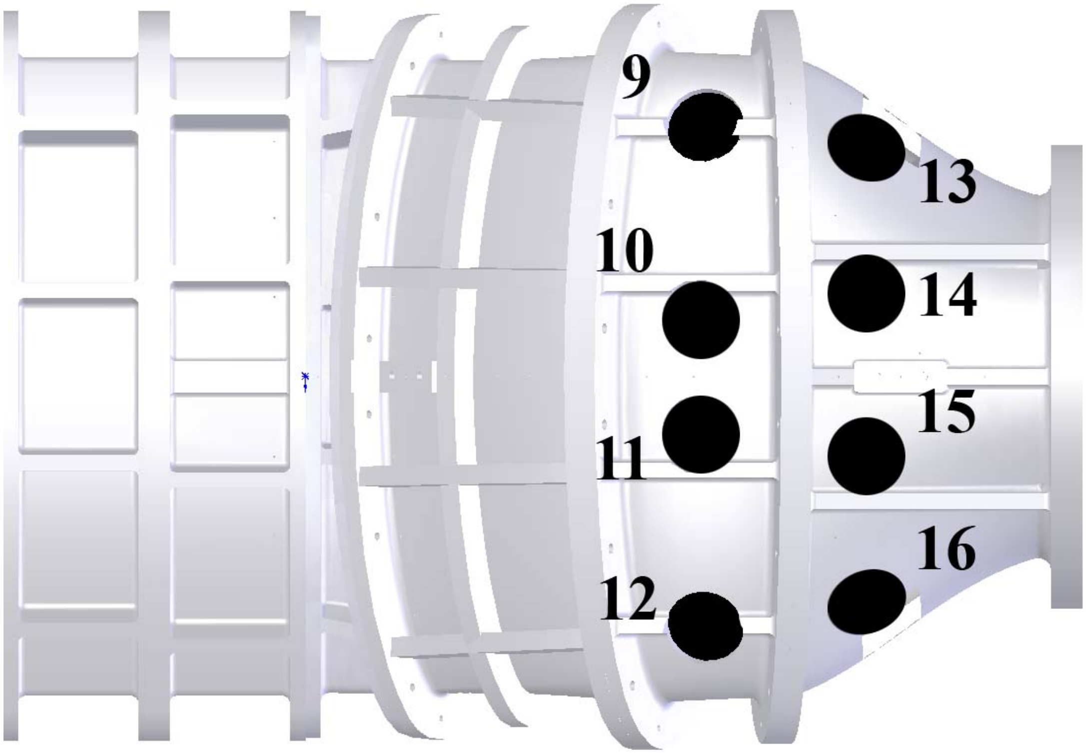

Figure 29: Second Bend Window Location Numbers

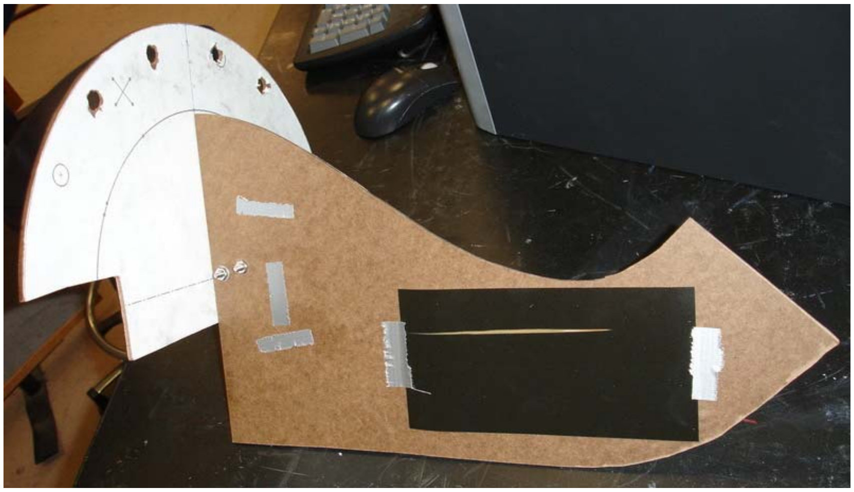

Figure 30: Wood Template to Locate Measurement Planes

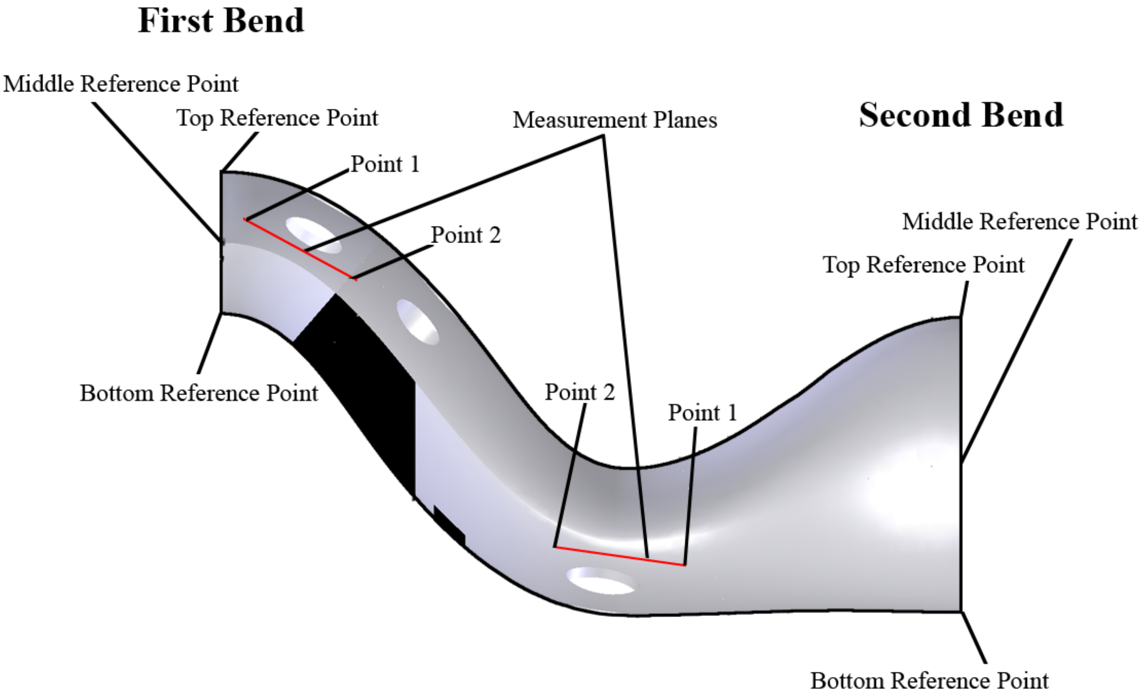

Figure 31: PIV Measurement Plane Reference Points

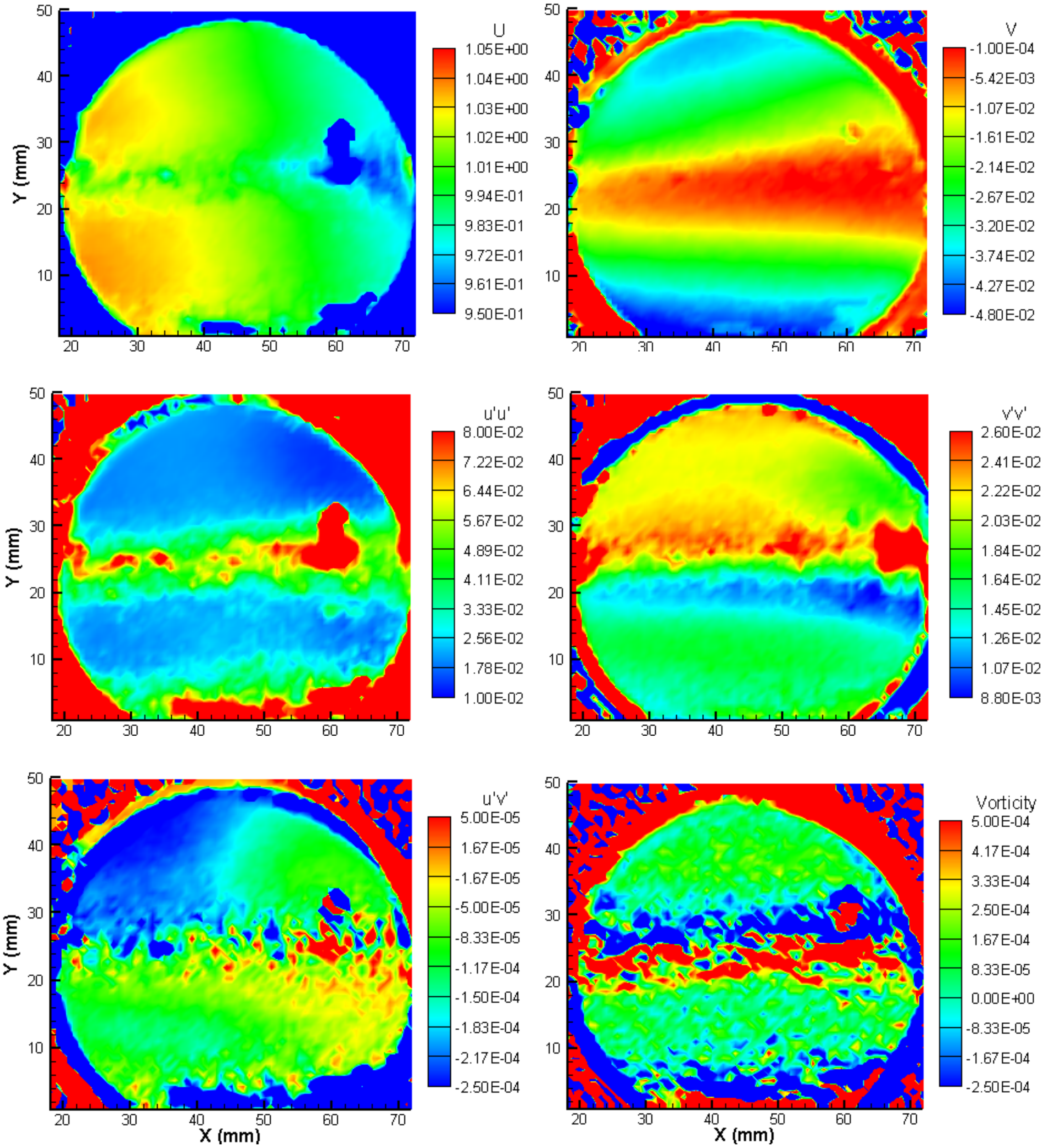

Figure 32: Location 1 Plane 1 Mean Velocities, Fluctuating Velocities, and Vorticity

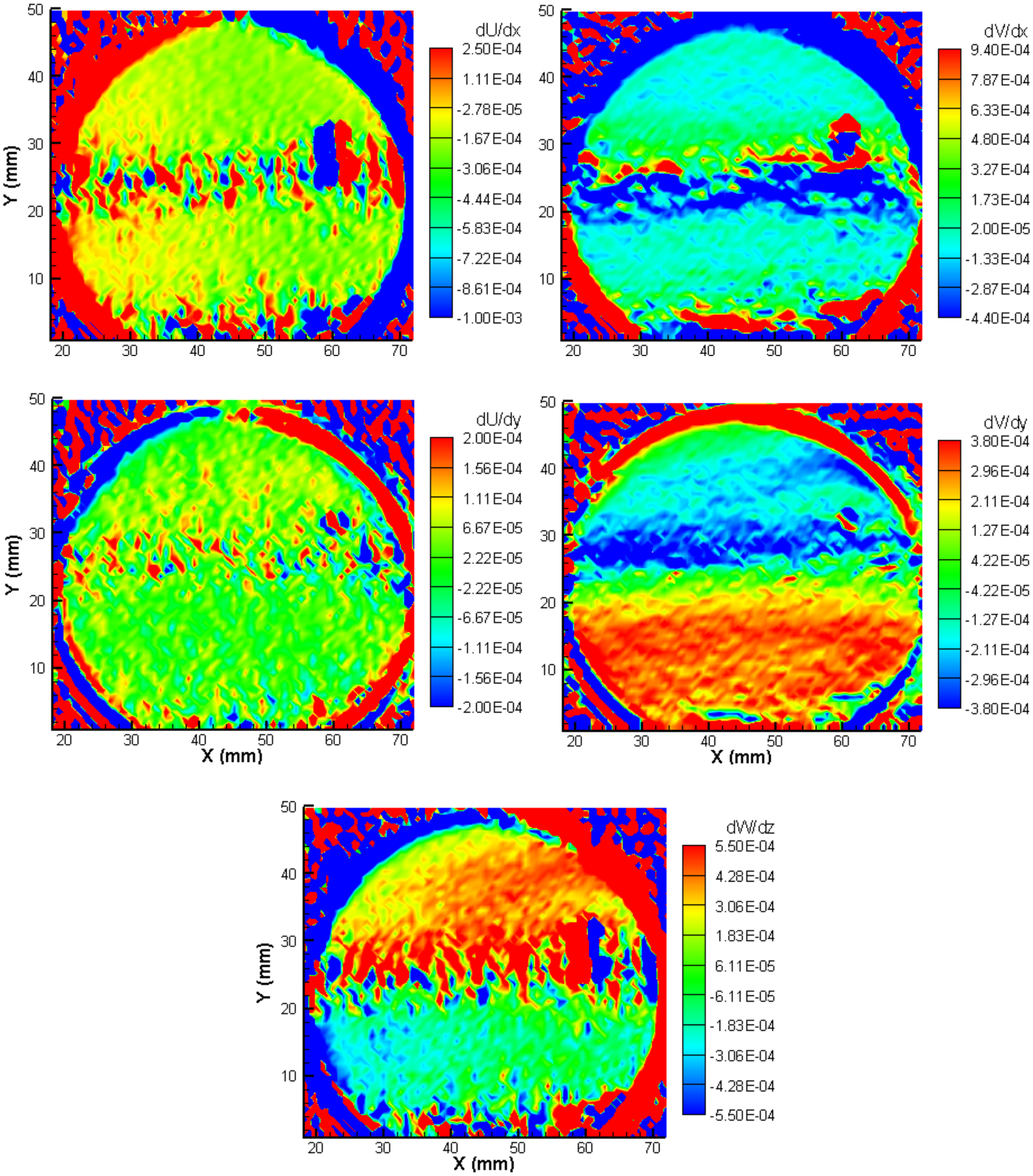

Figure 33: Location 1 Plane 1 Velocity Gradients

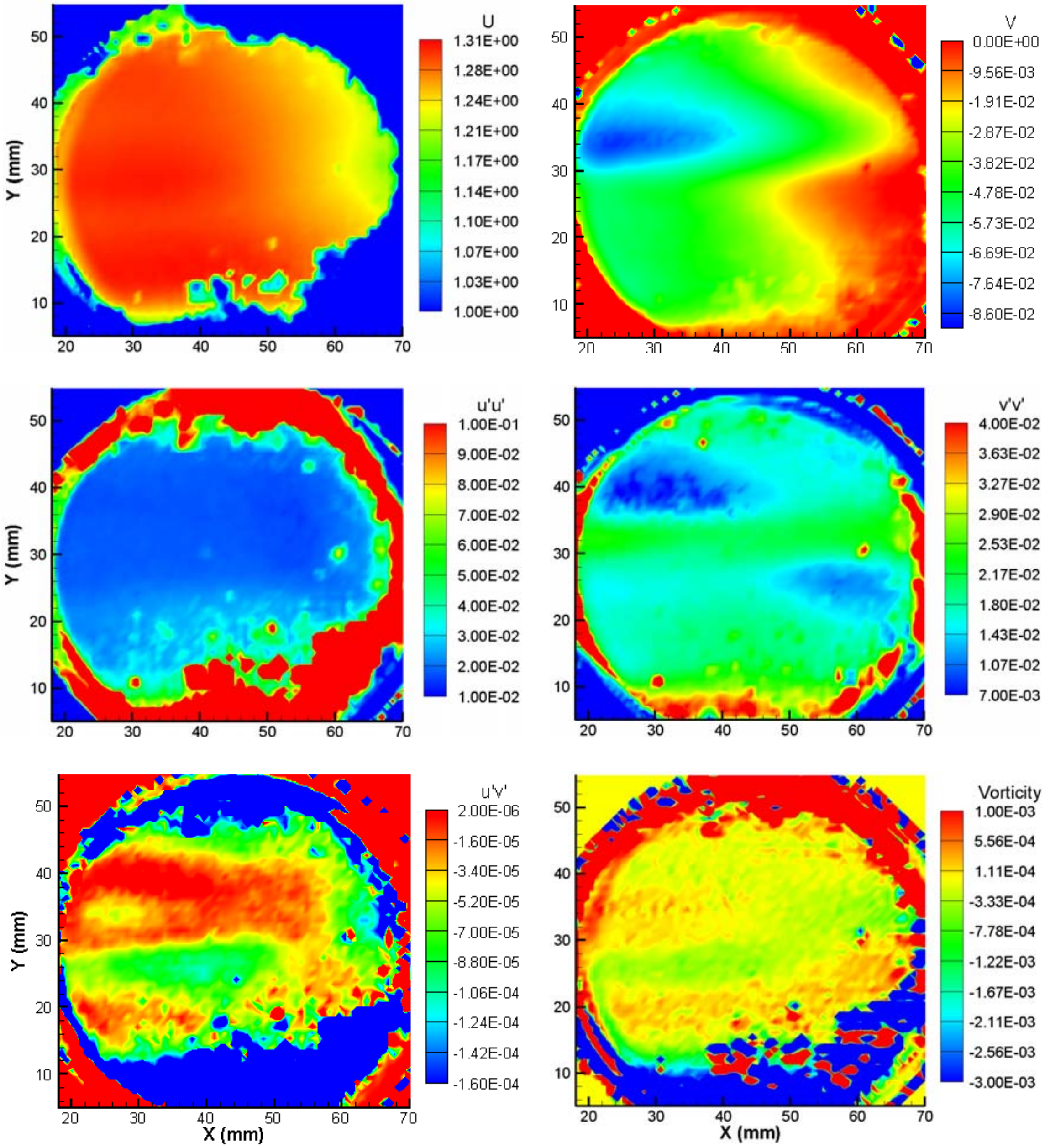

Figure 34: Location 1 Plane 2 Mean Velocities, Fluctuating Velocities, and Vorticity

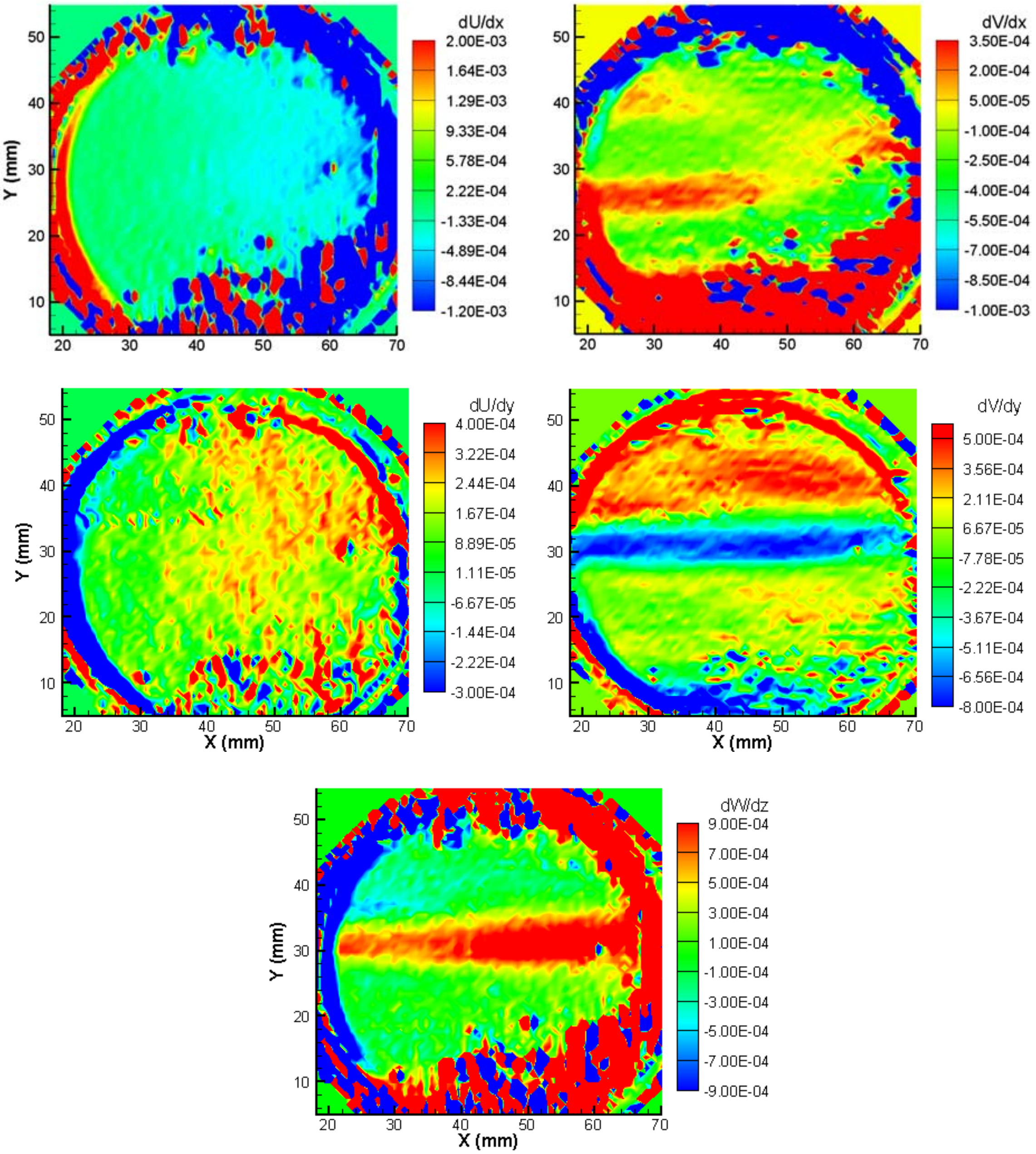

Figure 35: Location 1 Plane 2 Velocity Gradients

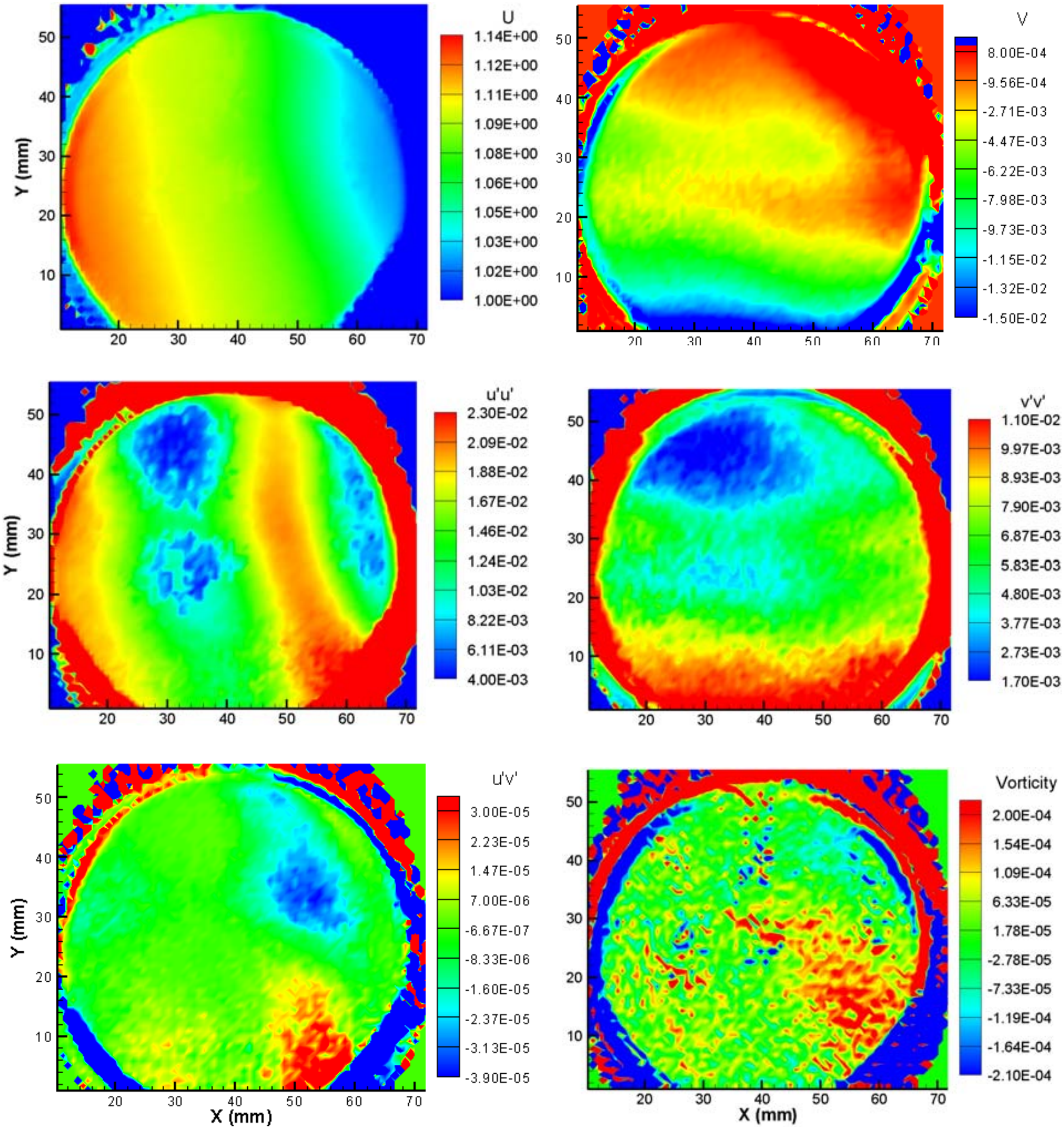

Figure 36: Location 2 Plane 1 Mean Velocities, Fluctuating Velocities, and Vorticity

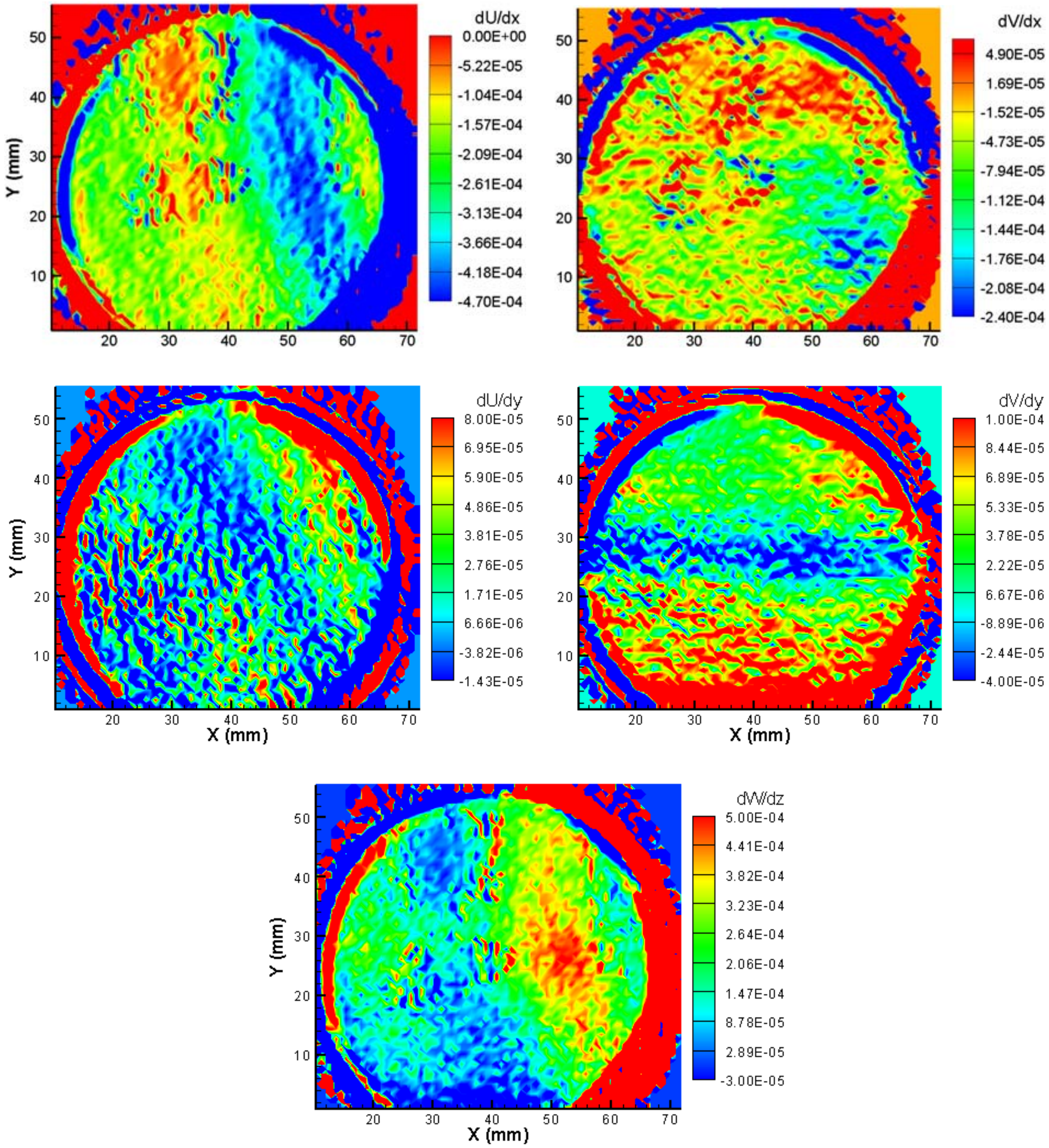

Figure 37: Location 2 Plane 1 Velocity Gradients

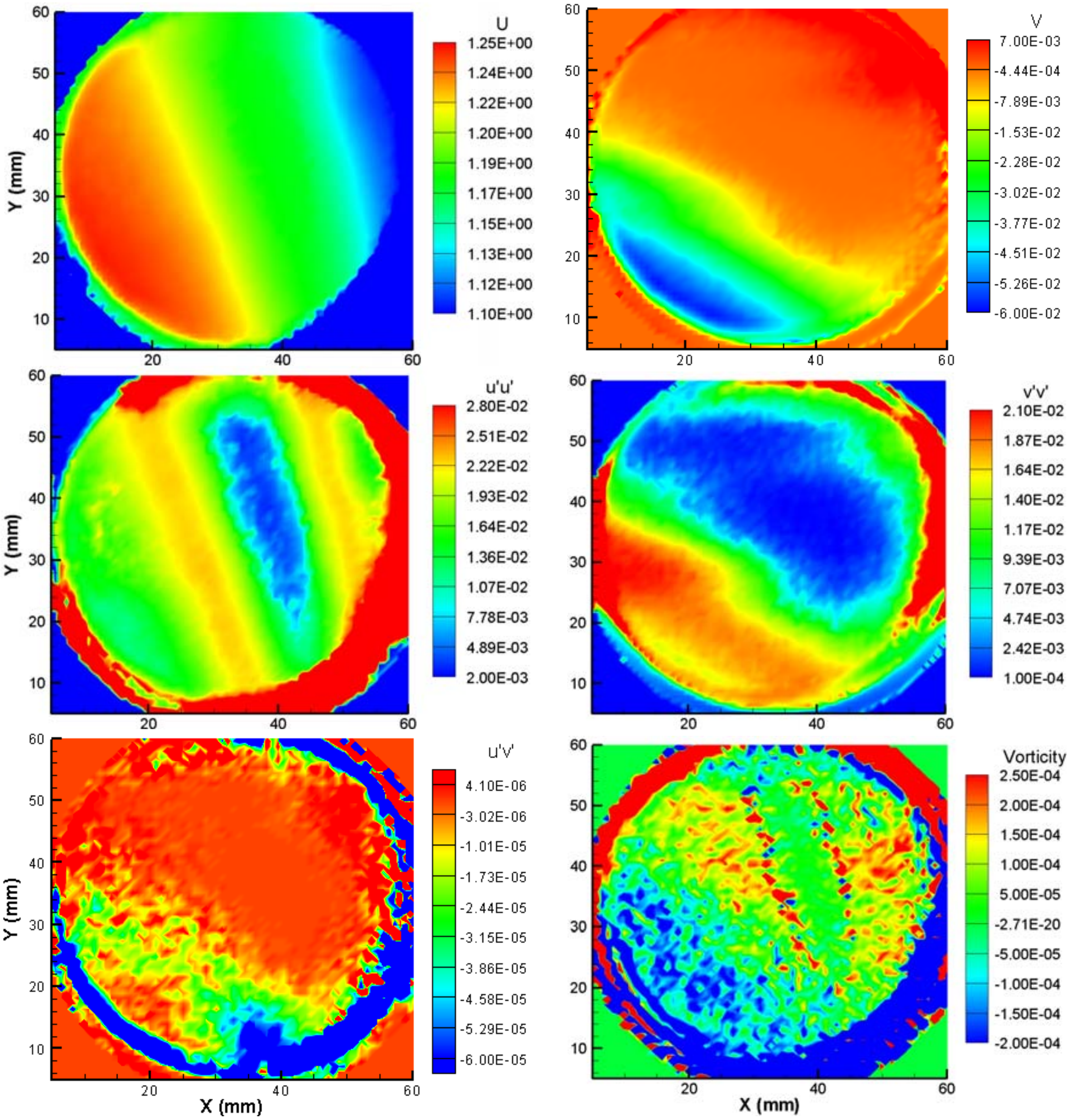

Figure 38: Location 2 Plane 2 Mean Velocities, Fluctuating Velocities, and Vorticity

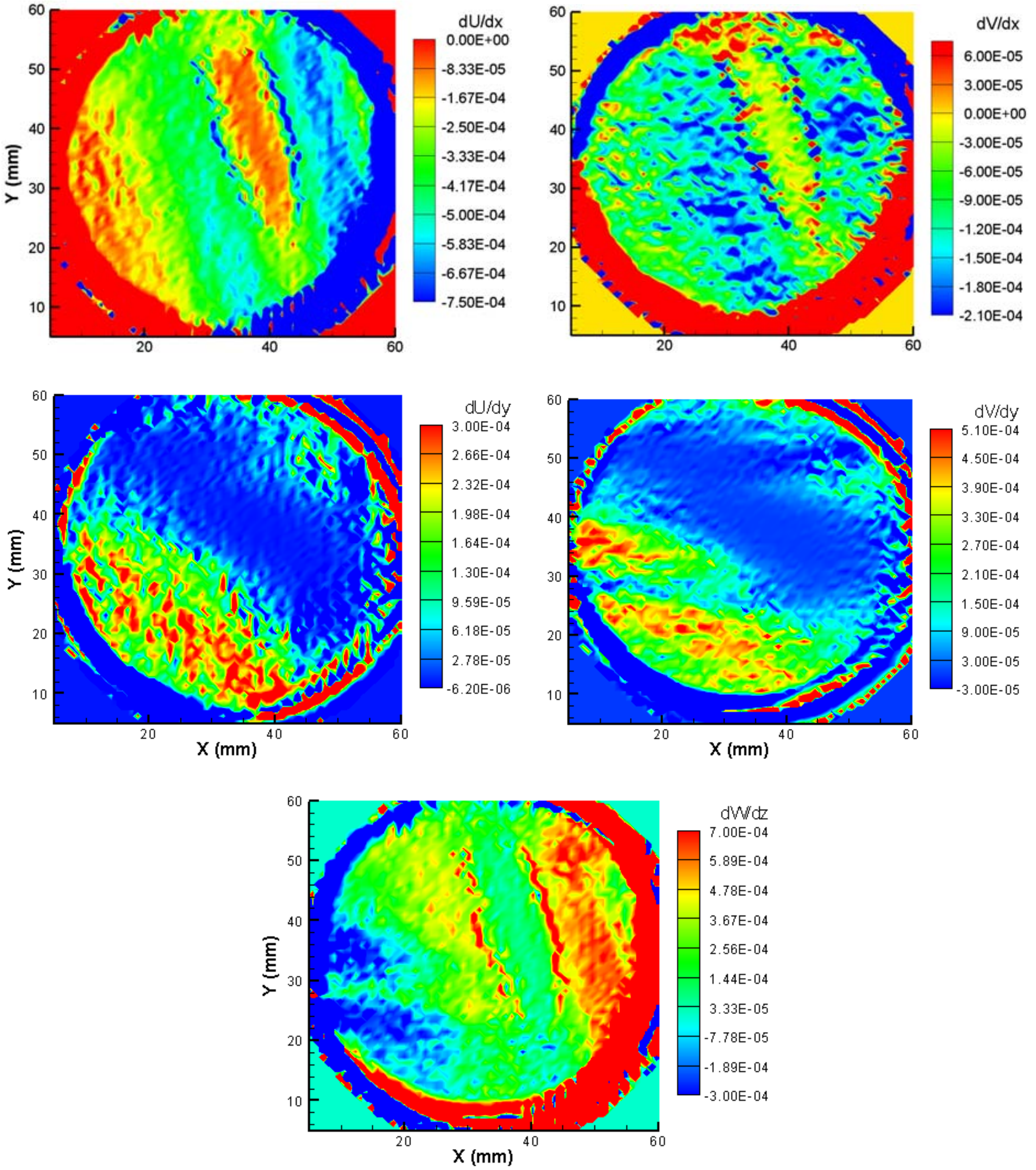

Figure 39: Location 2 Plane 2 Velocity Gradients

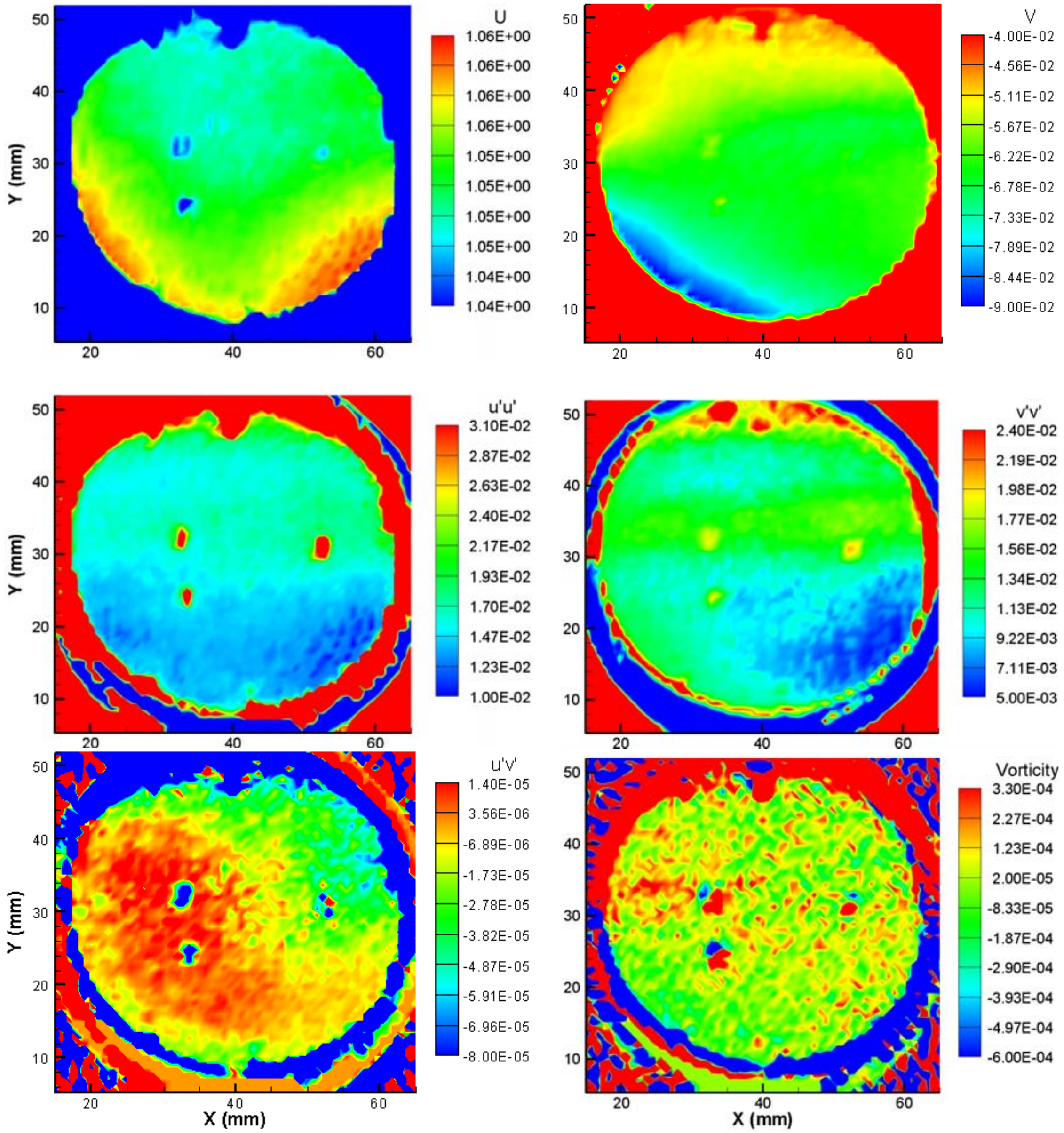

Figure 40: Location 5 Plane 5 Mean Velocities, Fluctuating Velocities, and Vorticity

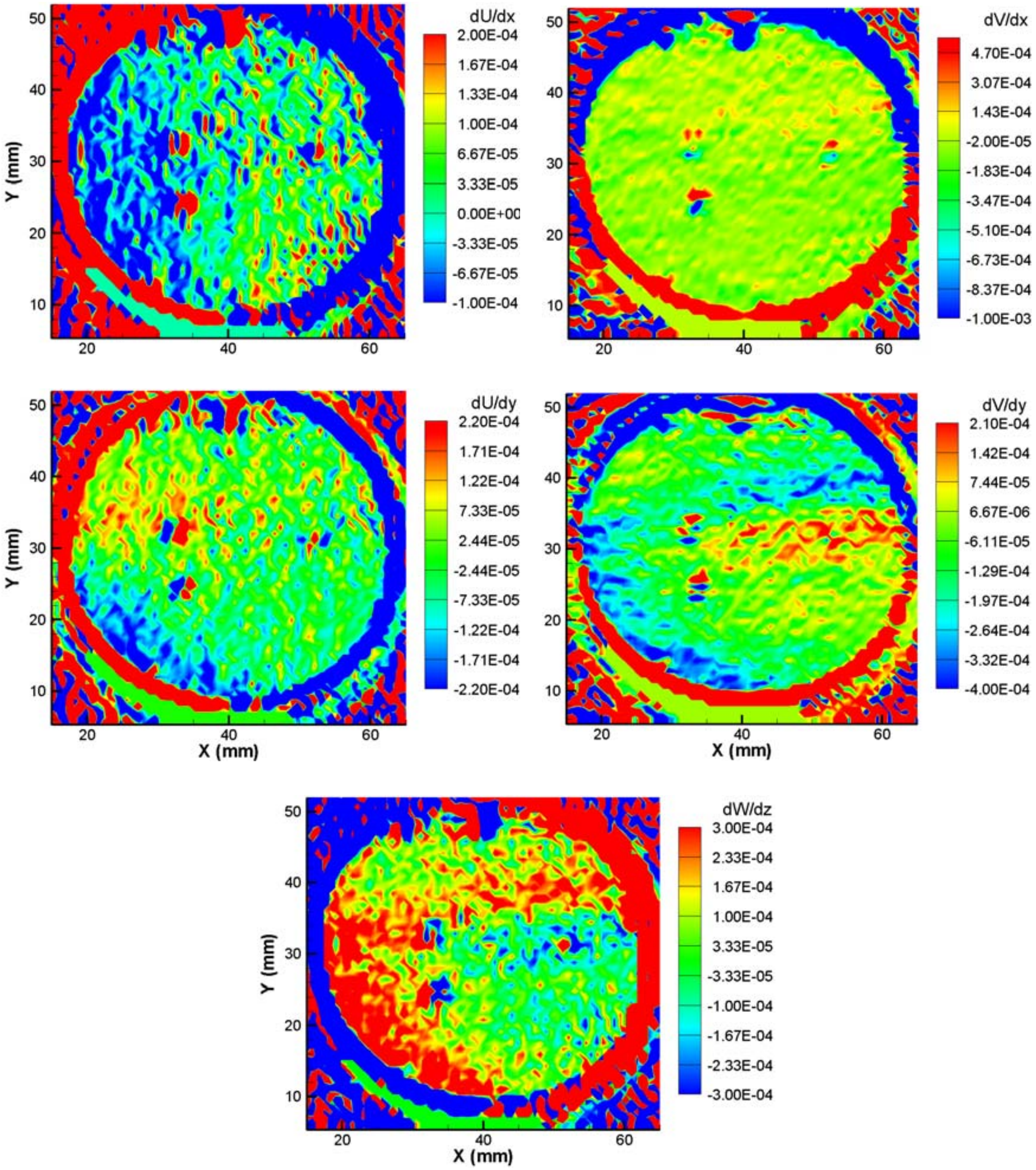

Figure 41: Location 5 Plane 5 Velocity Gradients

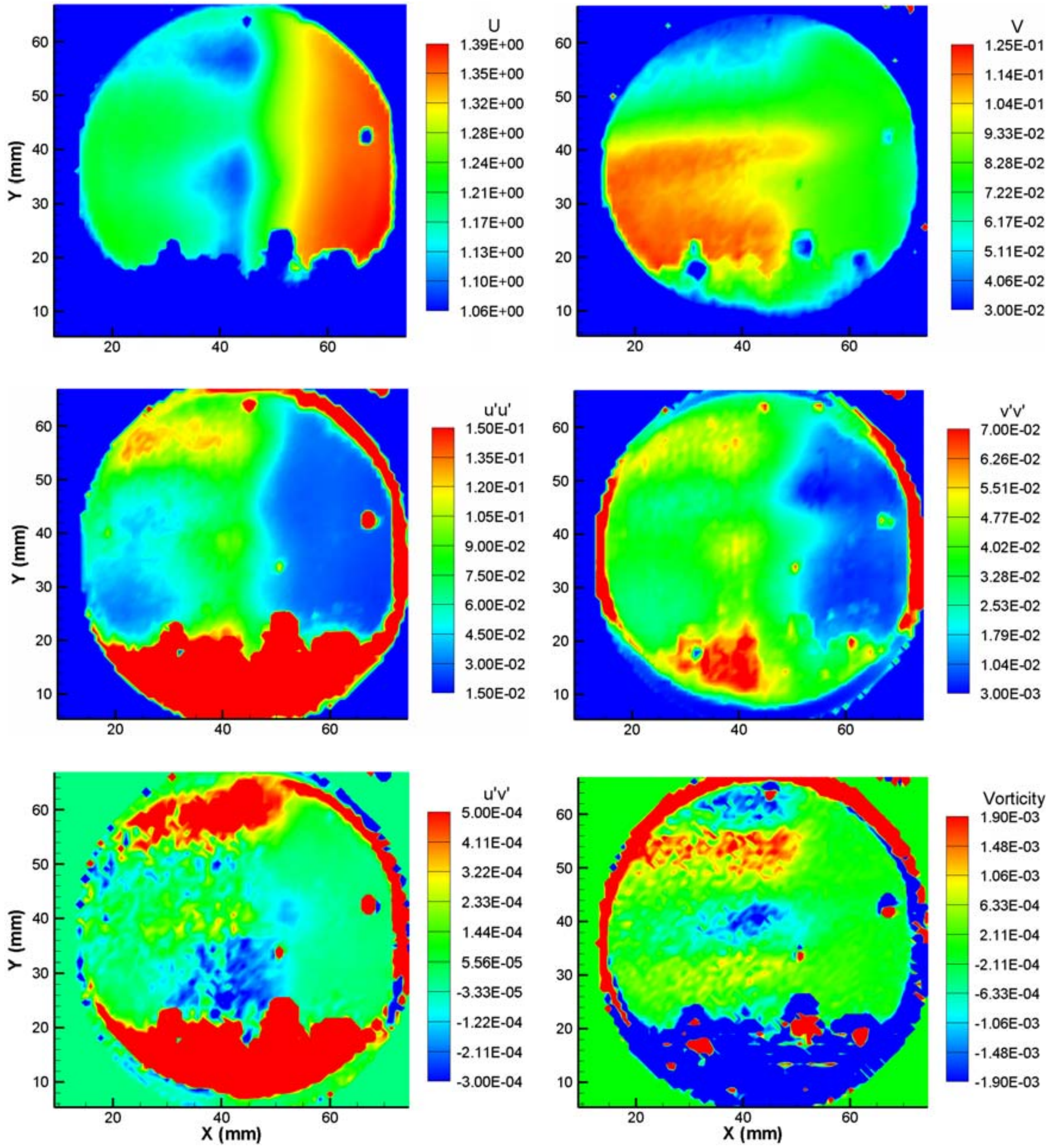

Figure 42: Location 6 Plane 6 Mean Velocities, Fluctuating Velocities, and Vorticity

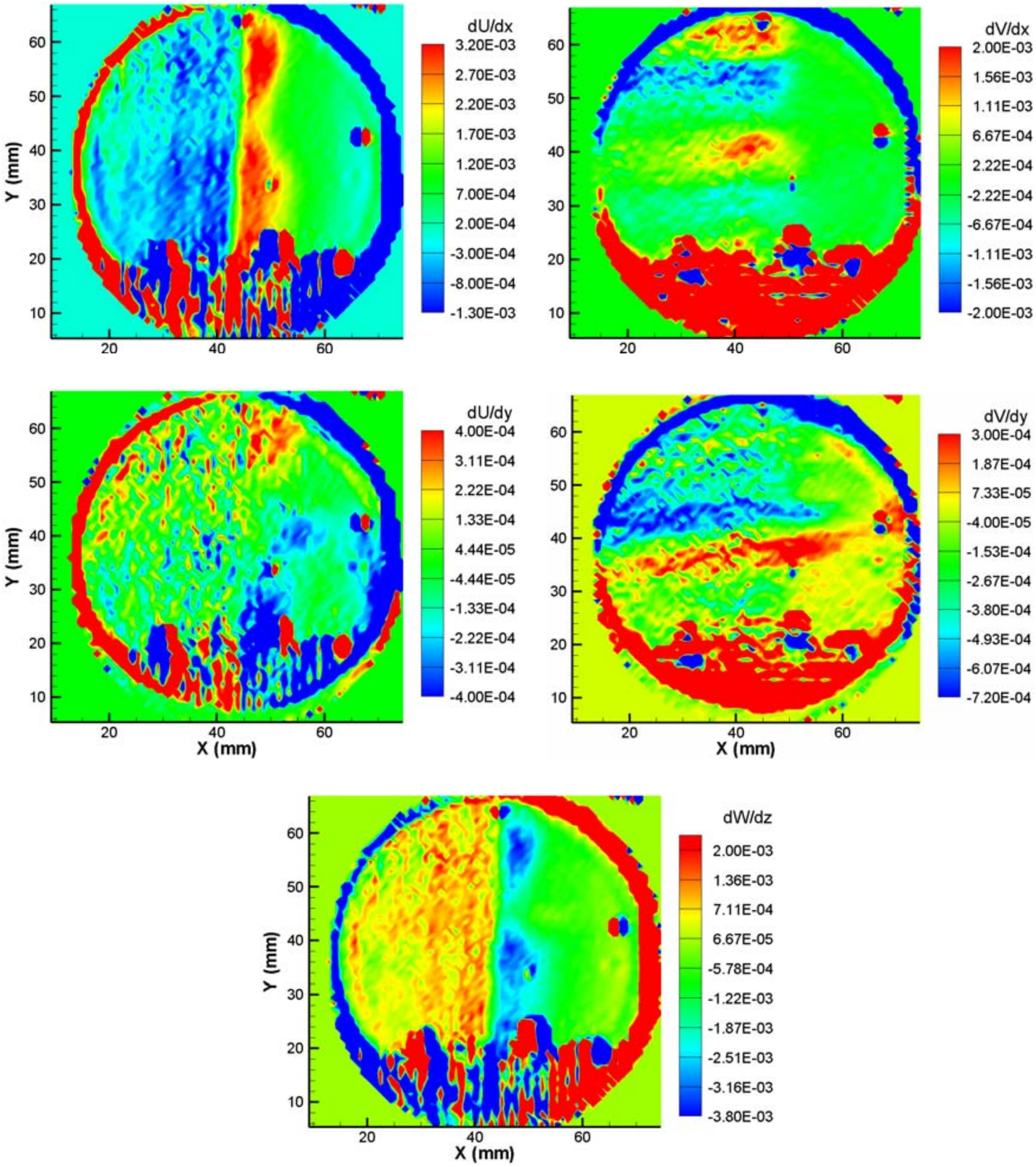

Figure 43: Location 6 Plane 6 Velocity Gradients

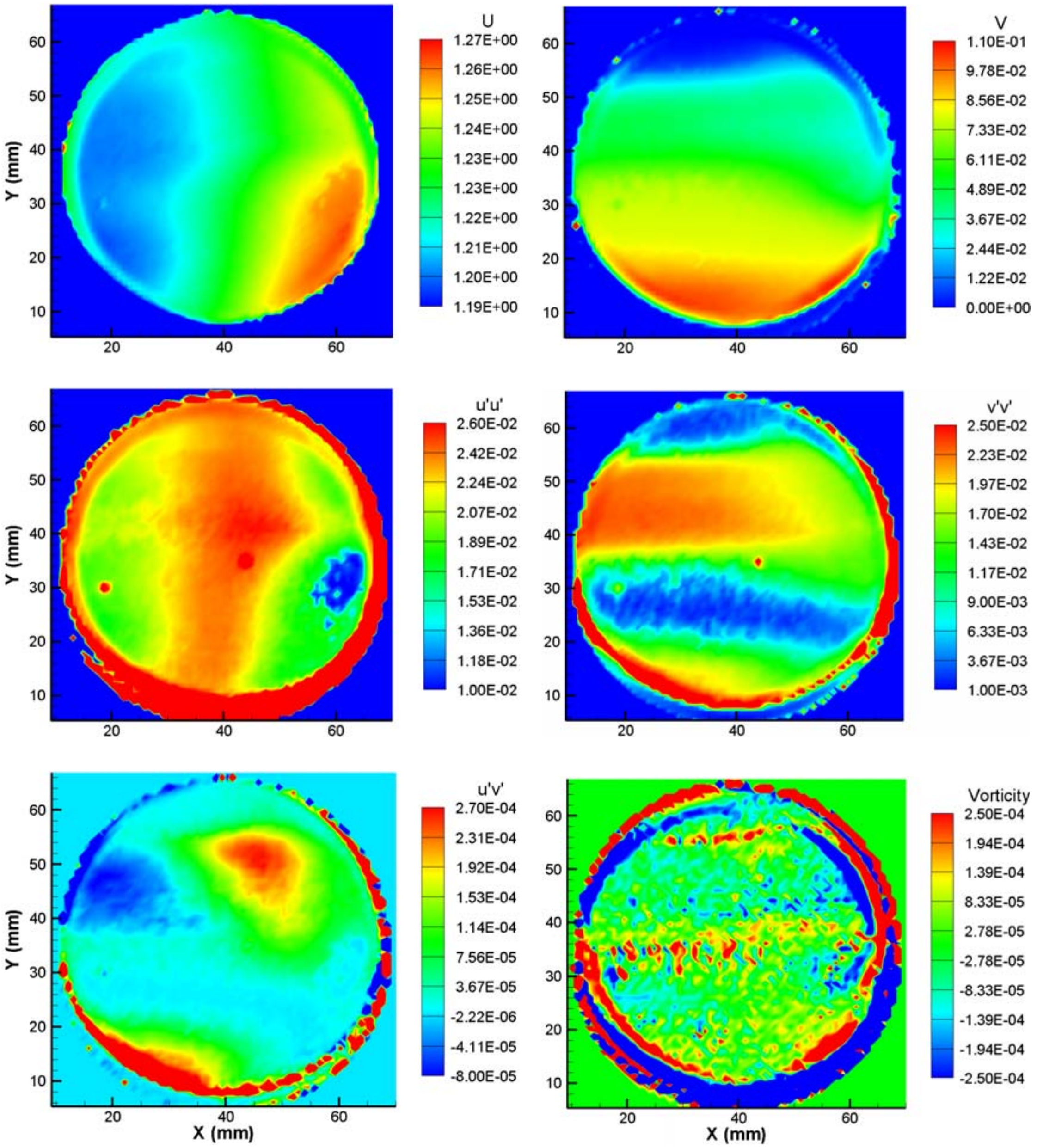

Figure 44: Location 6 Plane 7 Mean Velocities, Fluctuating Velocities, and Vorticity

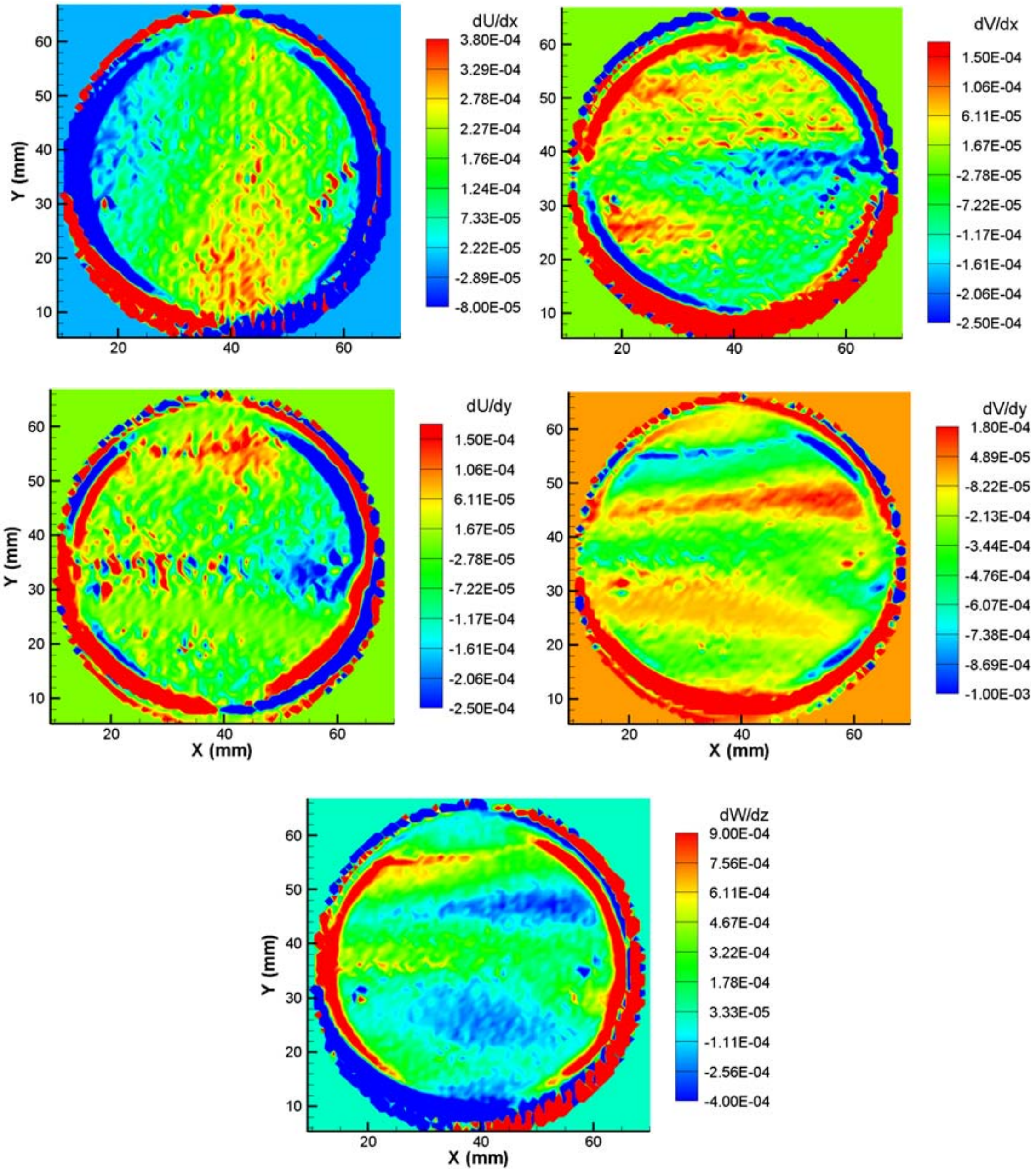

Figure 45: Location 6 Plane 7 Velocity Gradients

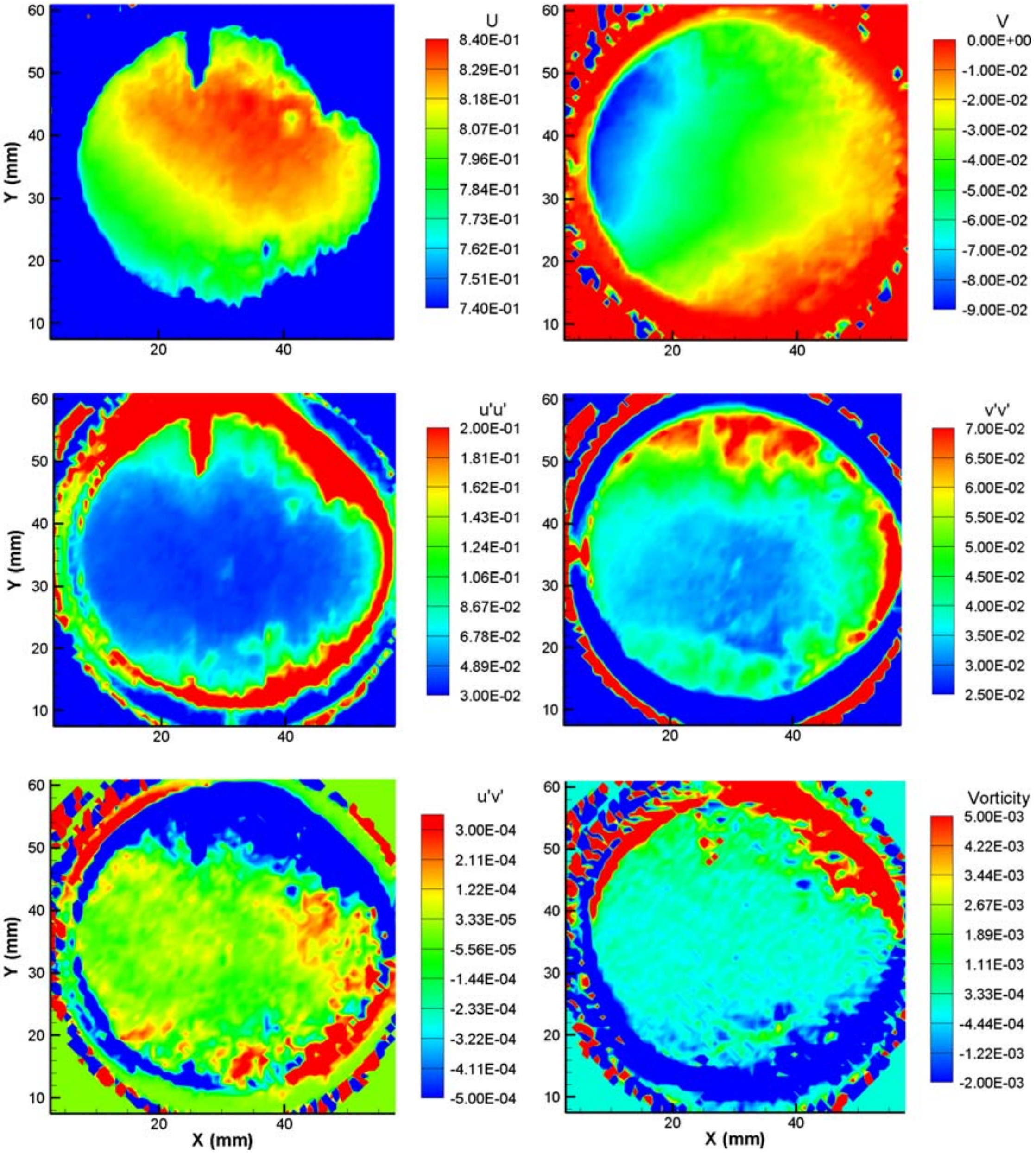

Figure 46: Location 9 Plane 8 Mean Velocities, Fluctuating Velocities, and Vorticity

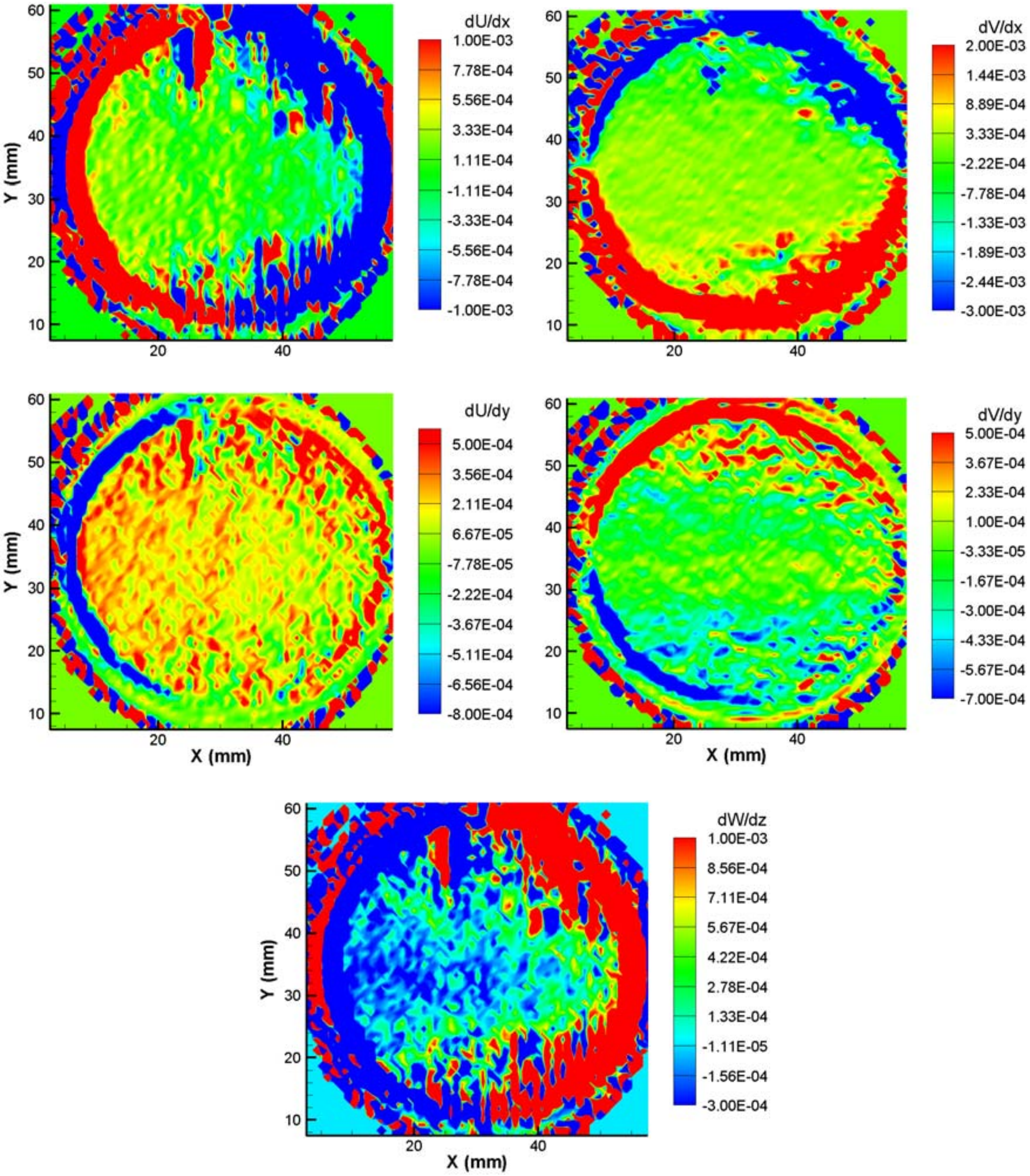

Figure 47: Location 9 Plane 8 Velocity Gradients

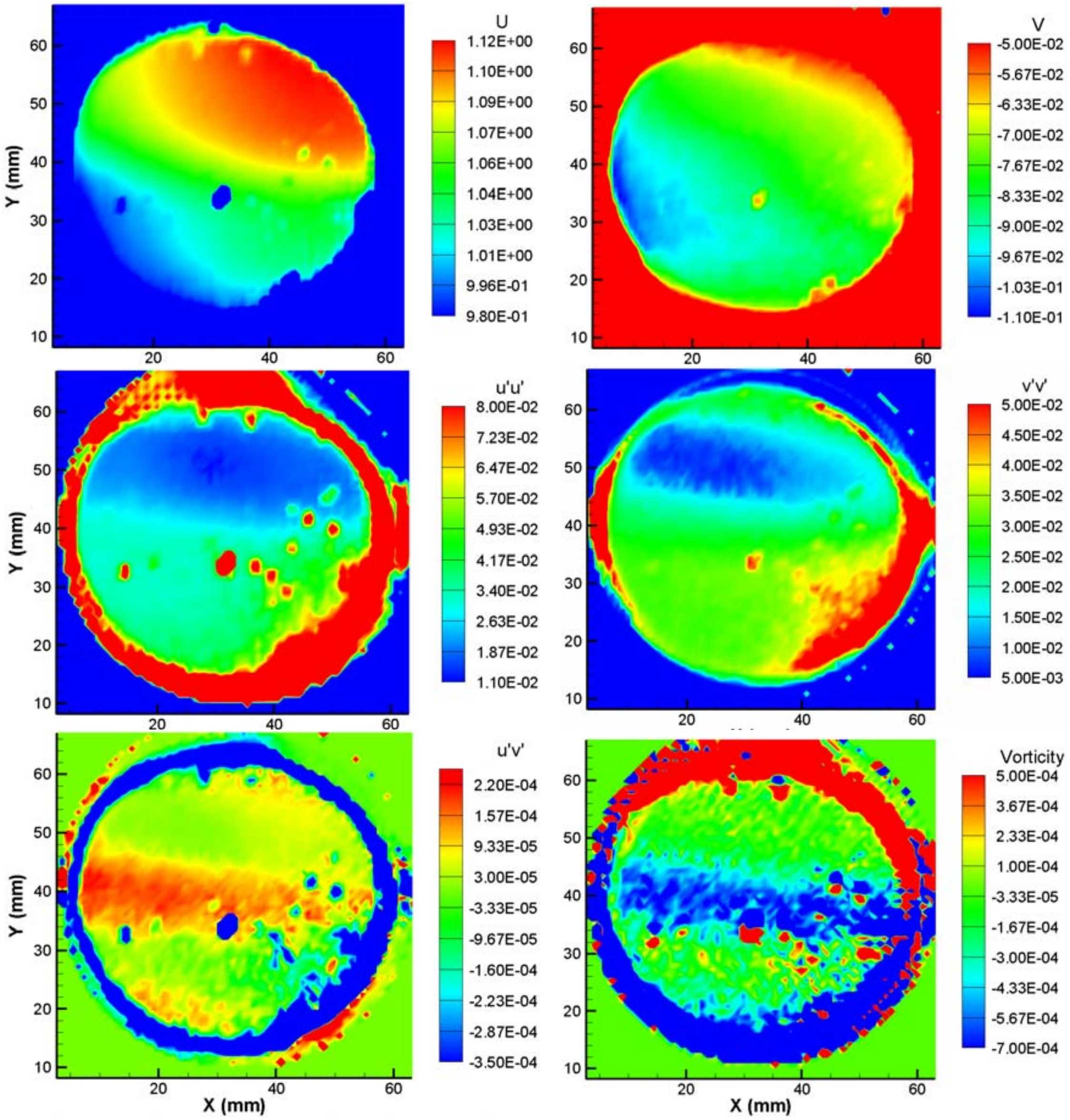

Figure 48: Location 9 Plane 11 Mean Velocities, Fluctuating Velocities, and Vorticity

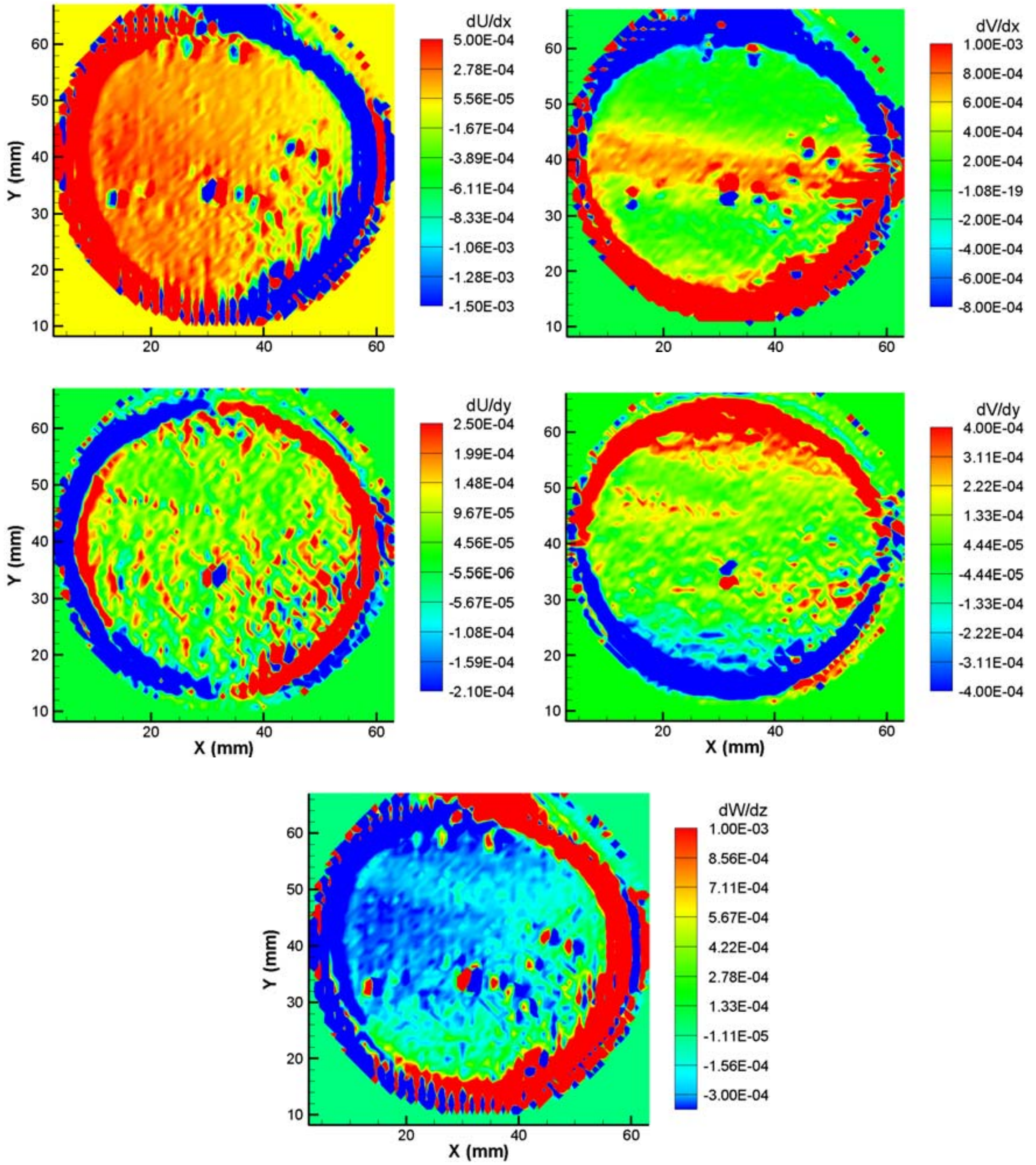

Figure 49: Location 9 Plane 11 Velocity Gradients

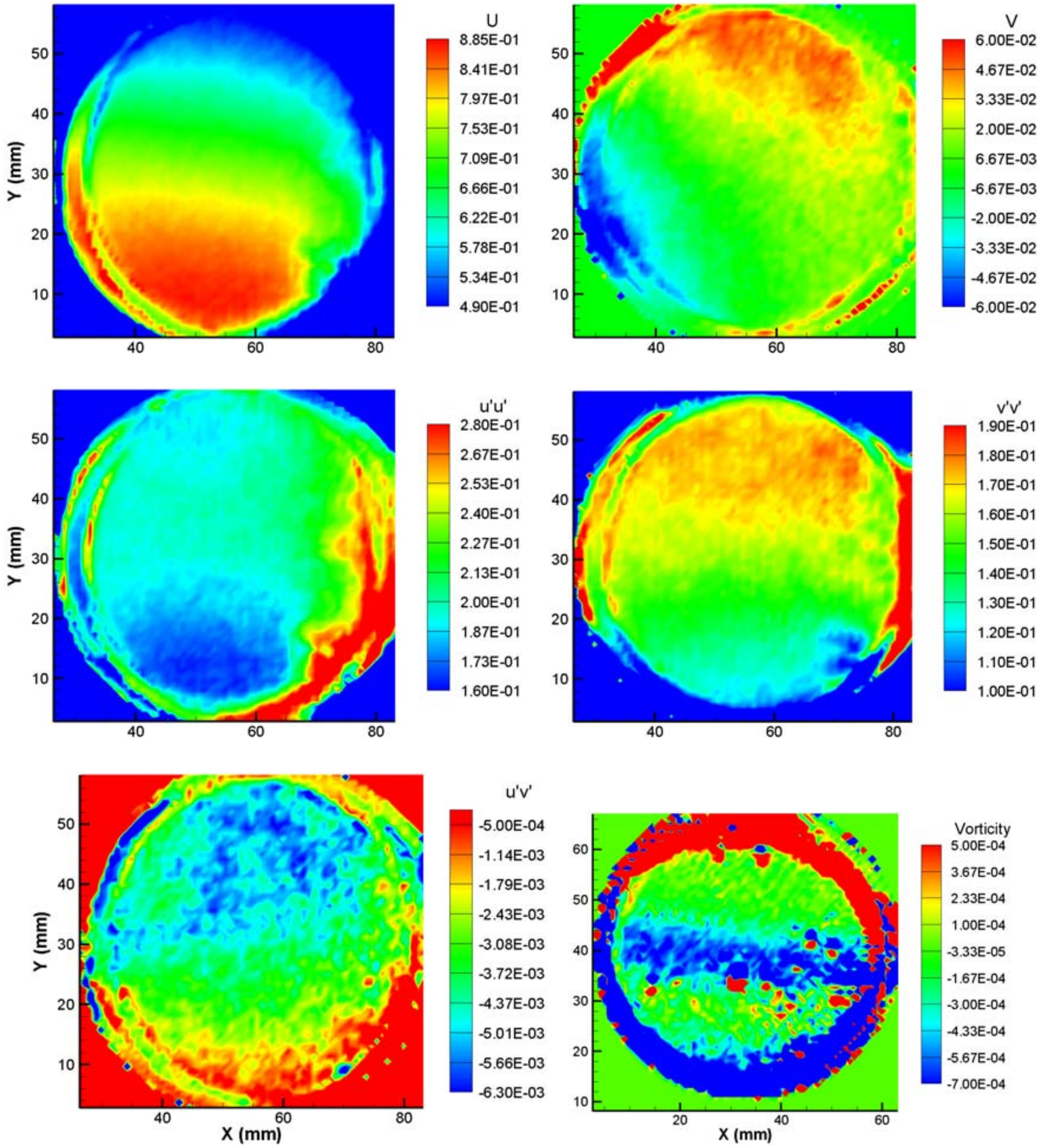

Figure 50: Location 10 Plane 8 Mean Velocities, Fluctuating Velocities, and Vorticity

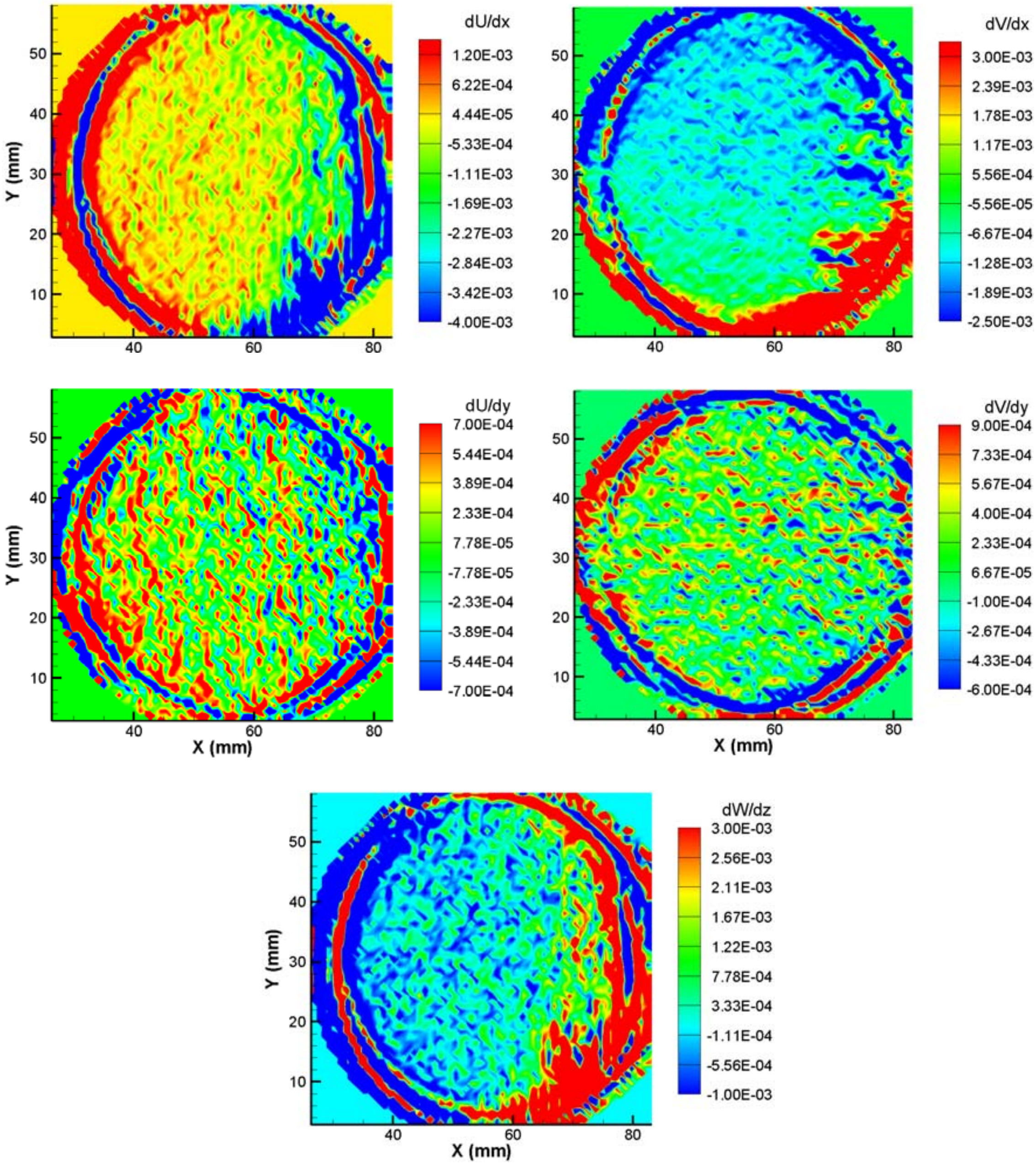

Figure 51: Location 10 Plane 8 Velocity Gradients

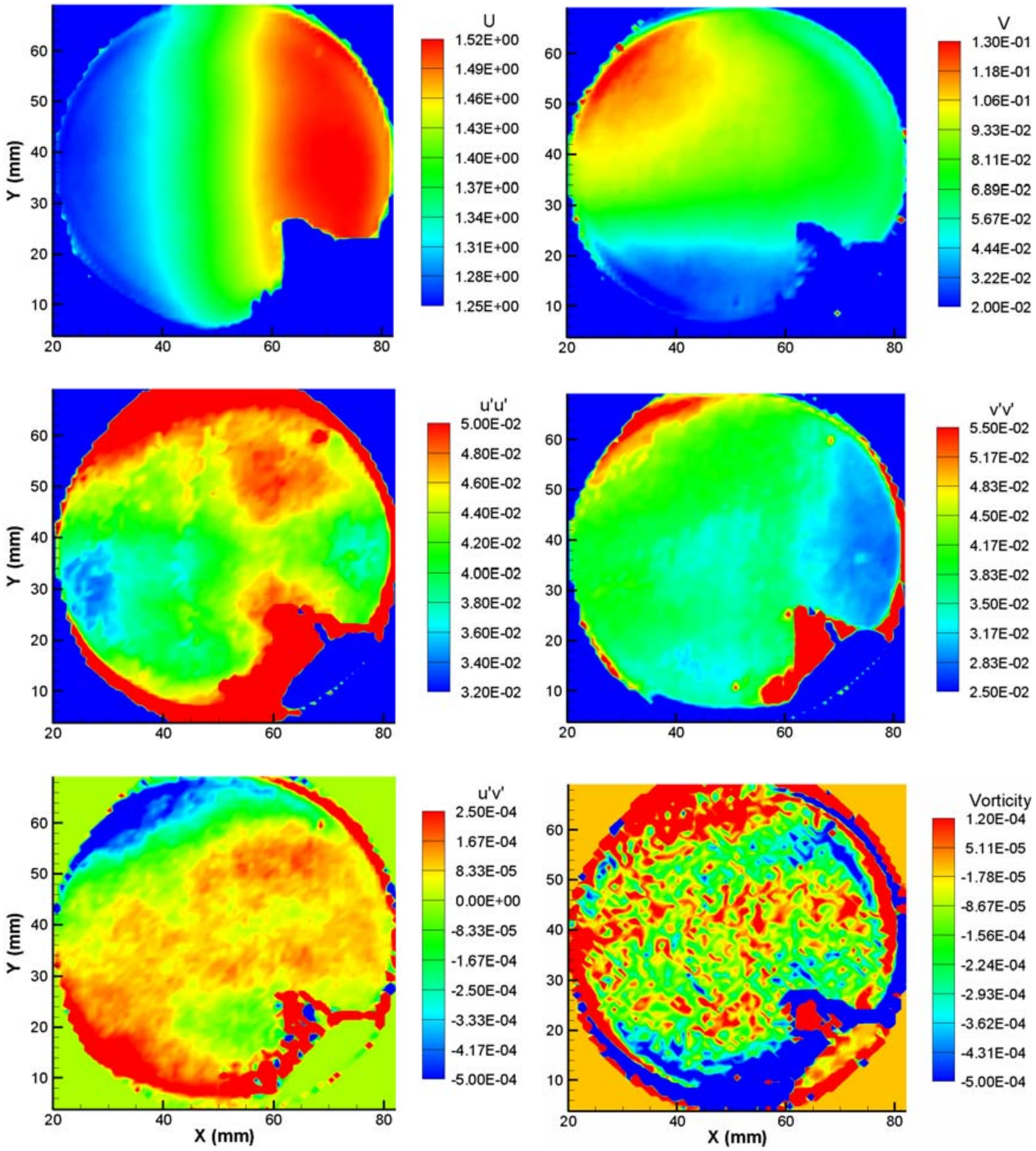

Figure 52: Location 10 Plane 9 Mean Velocities, Fluctuating Velocities, and Vorticity

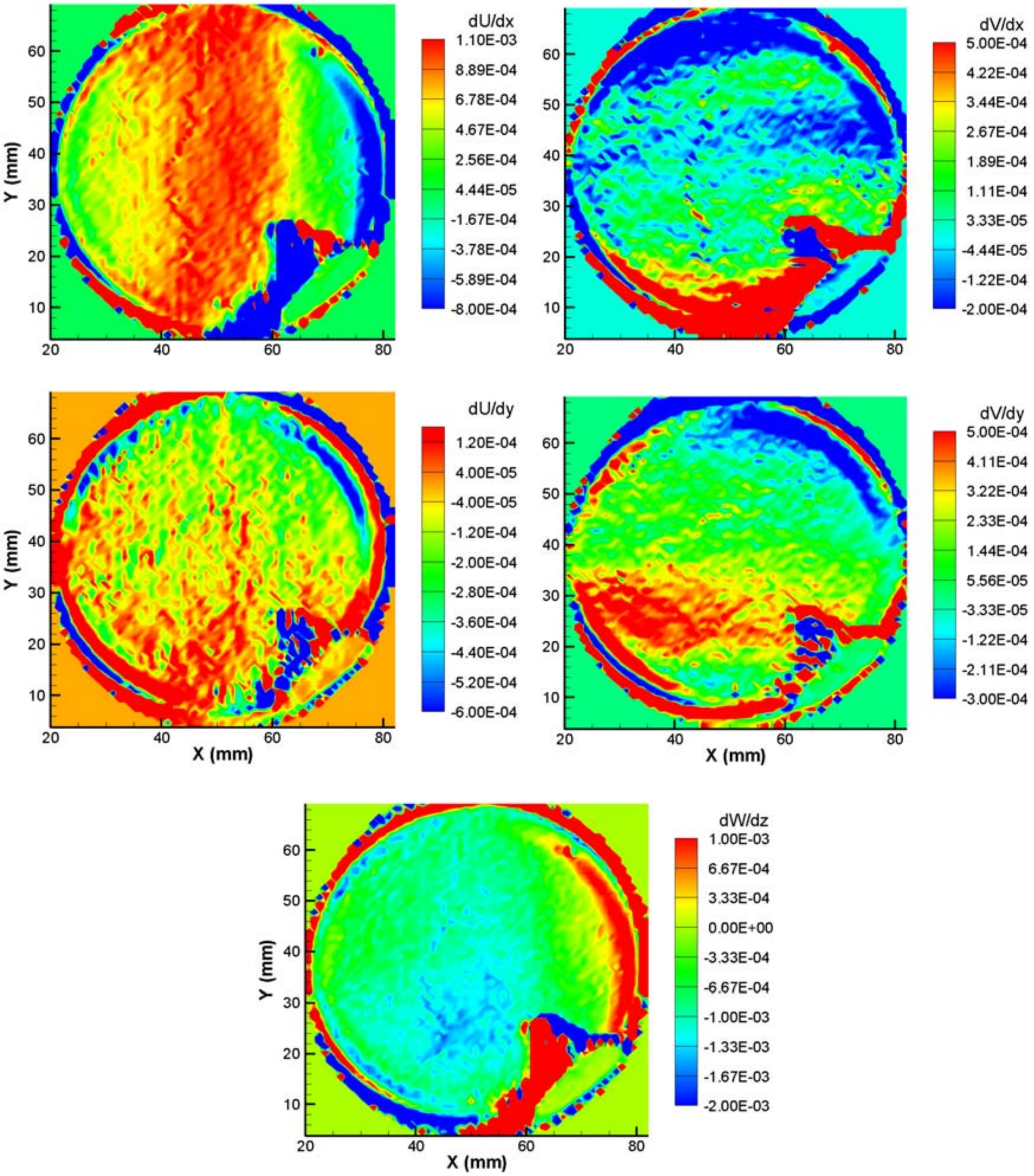

Figure 53: Location 10 Plane 9 Velocity Gradients

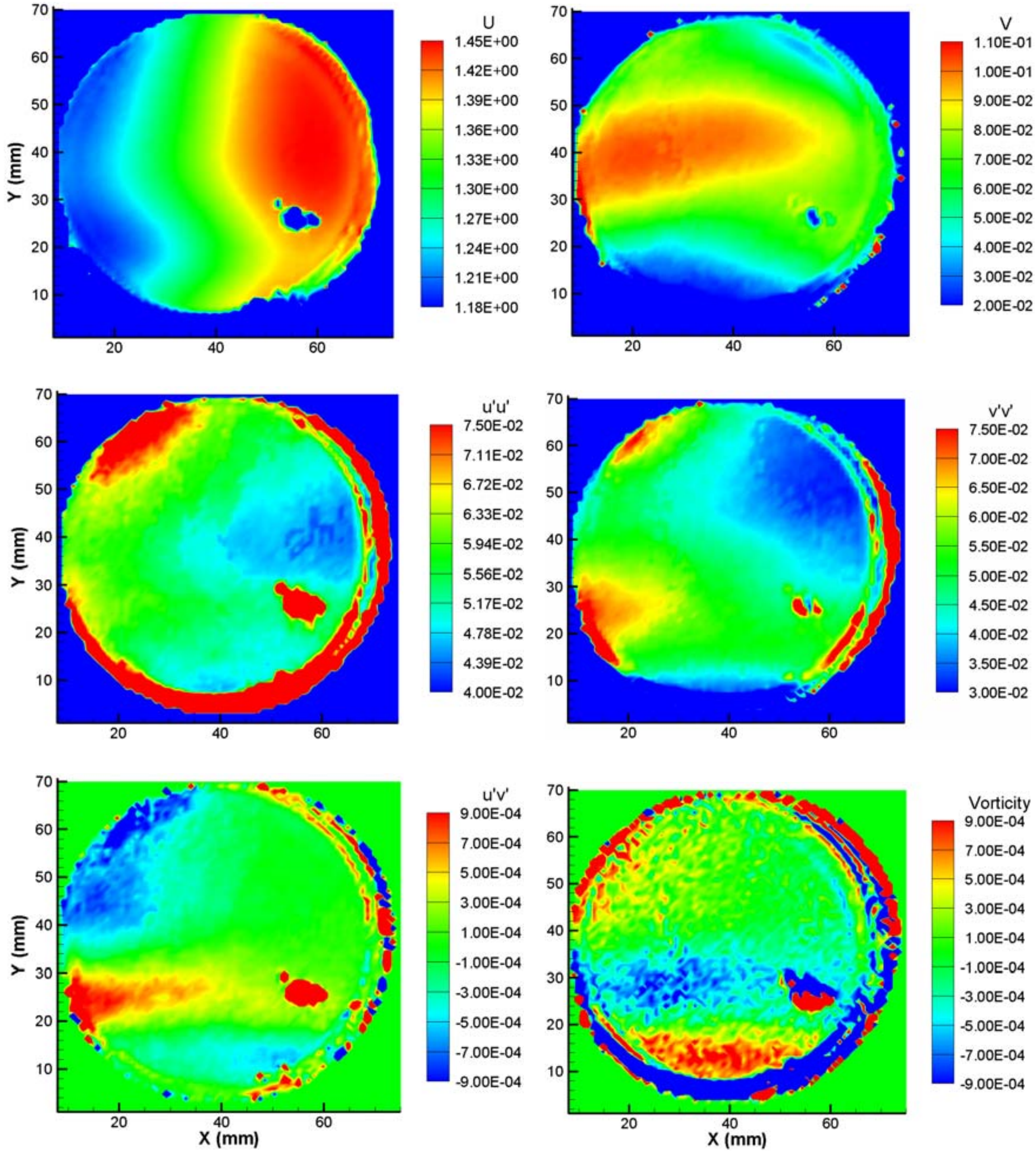

Figure 54: Location 10 Plane 10 Mean Velocities, Fluctuating Velocities, and Vorticity

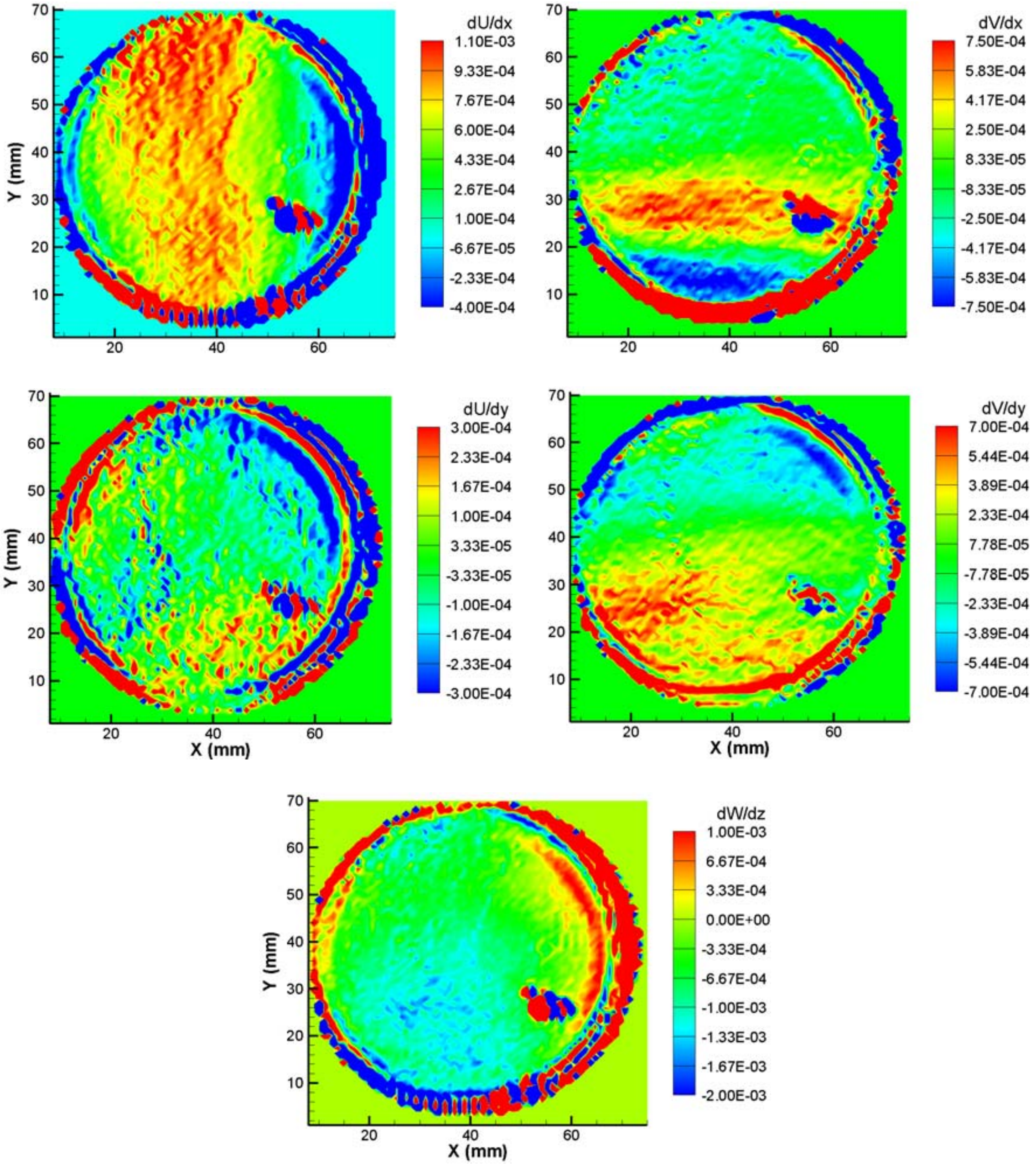

Figure 55: Location 10 Plane 10 Velocity Gradients

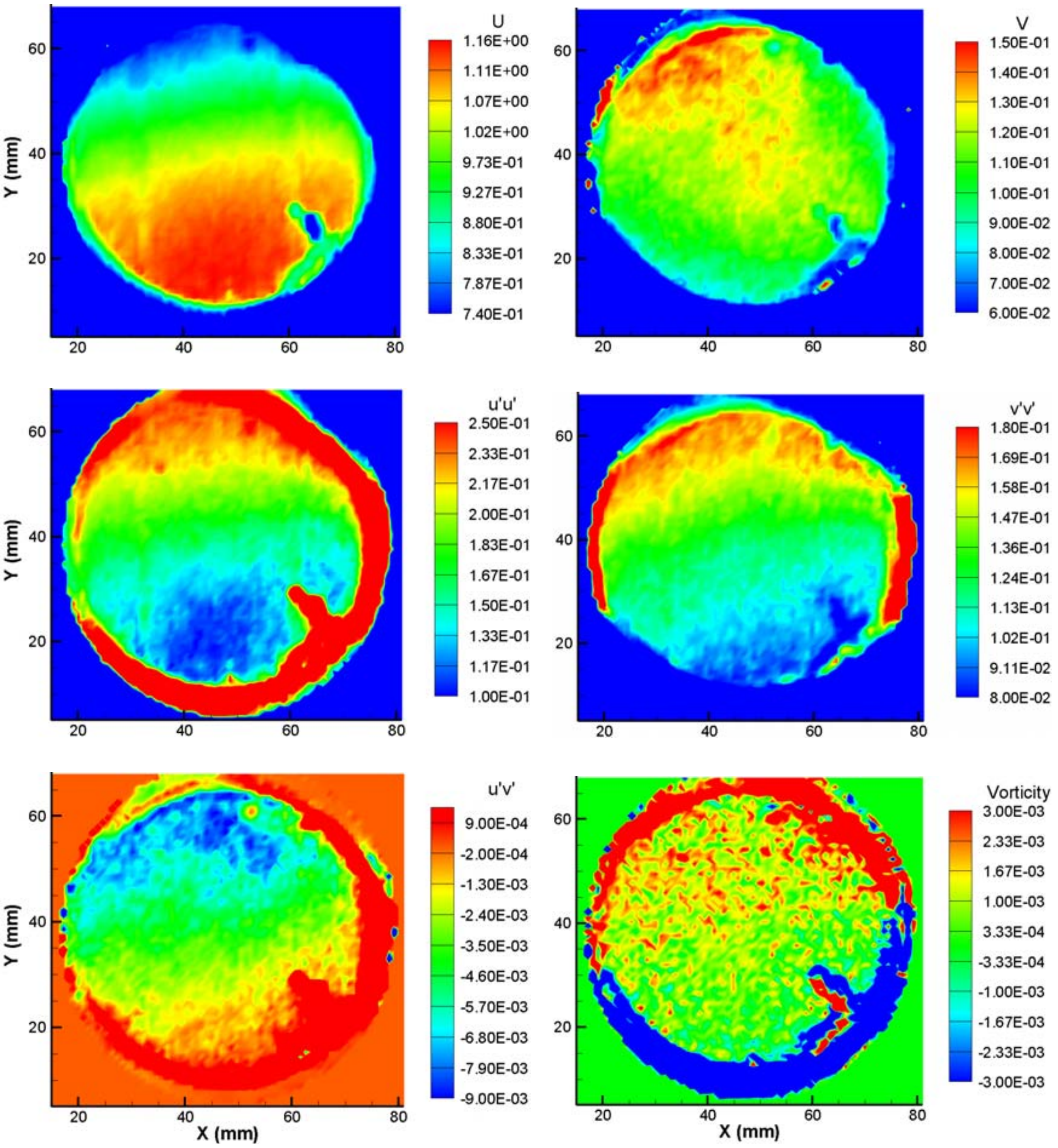

Figure 56: Location 10 Plane 11 Mean Velocities, Fluctuating Velocities, and Vorticity

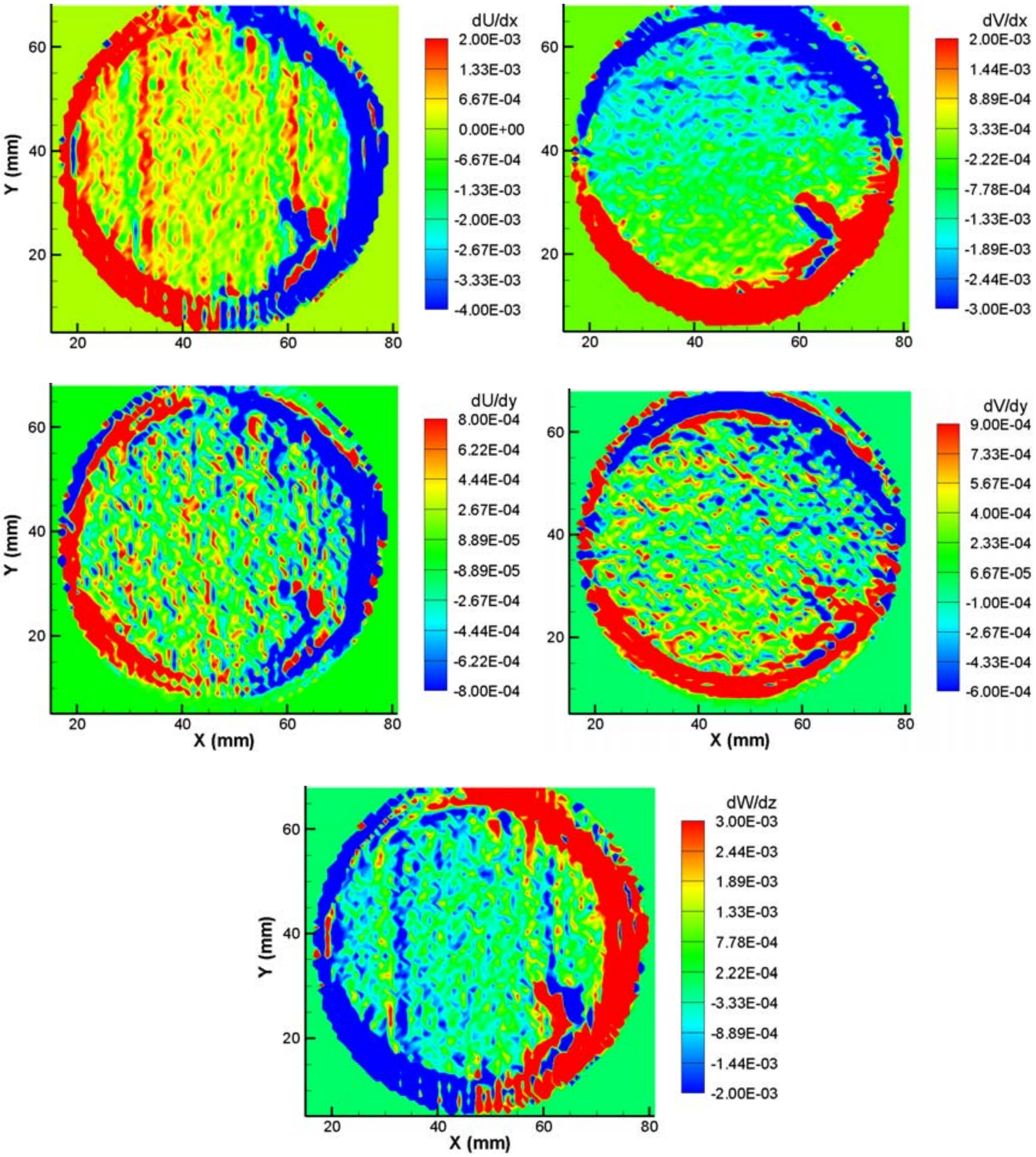

Figure 57: Location 10 Plane 11 Velocity Gradients

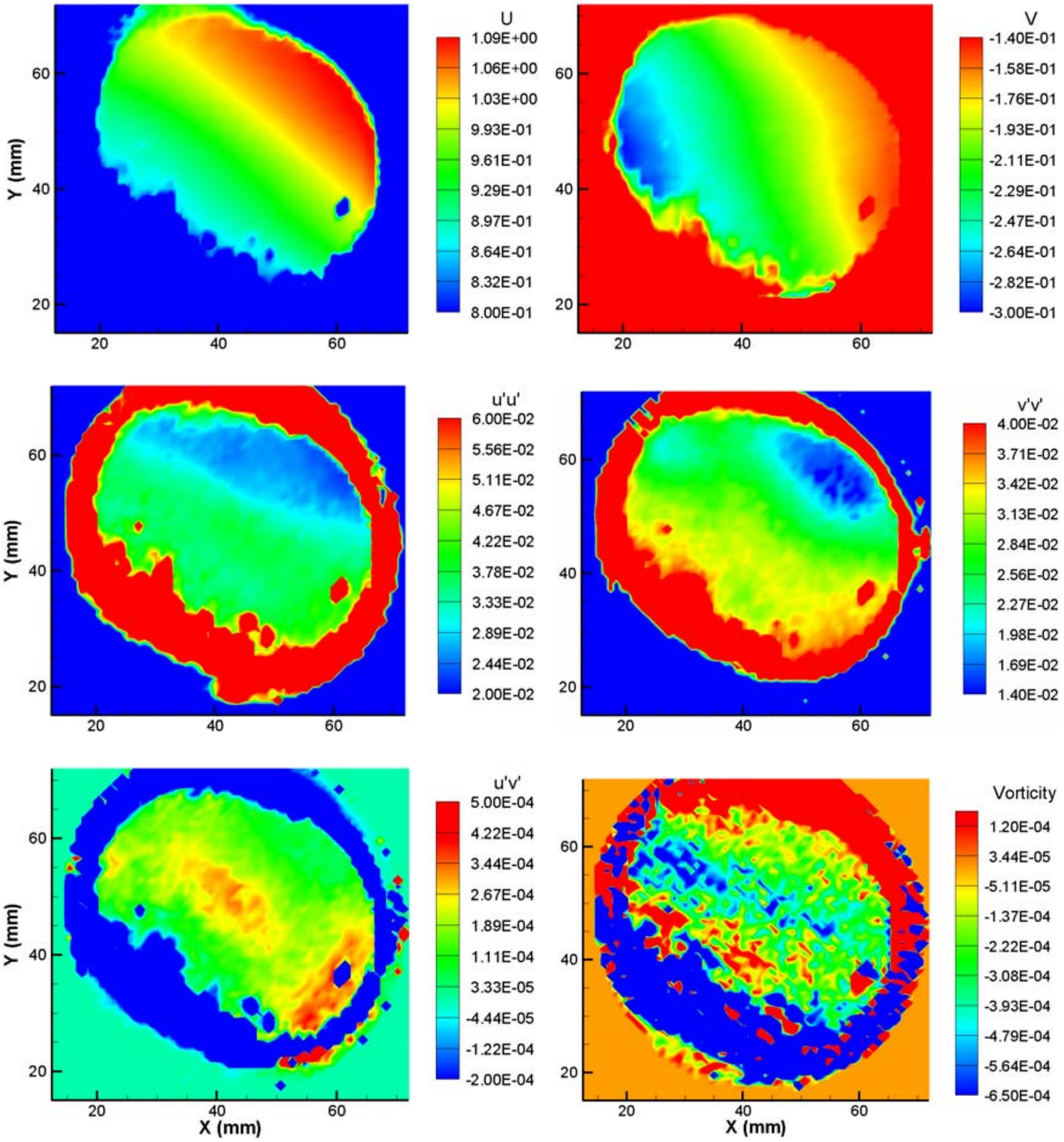

Figure 58: Location 13 Plane 12 Mean Velocities, Fluctuating Velocities, and Vorticity

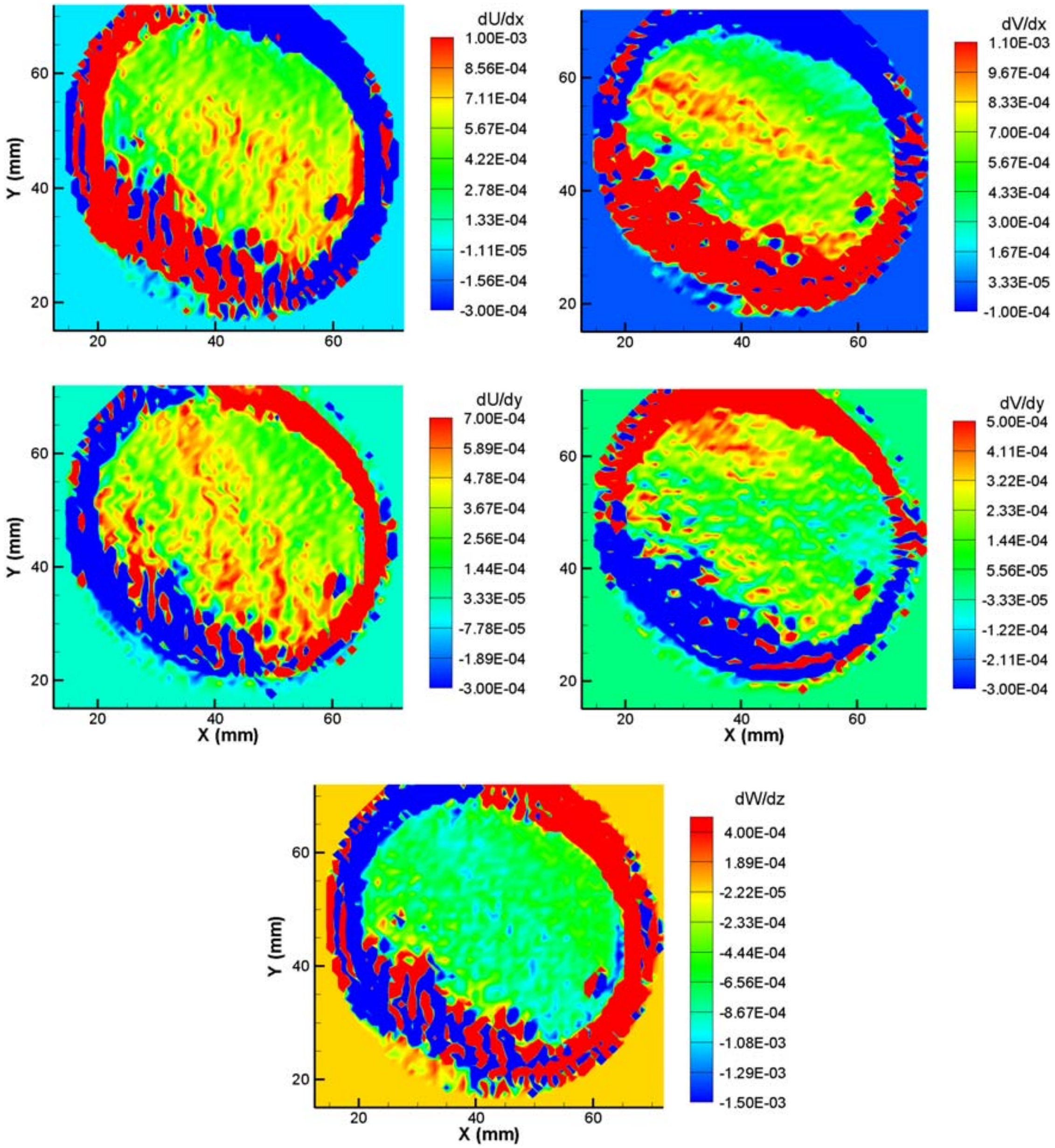

Figure 59: Location 13 Plane 12 Velocity Gradients

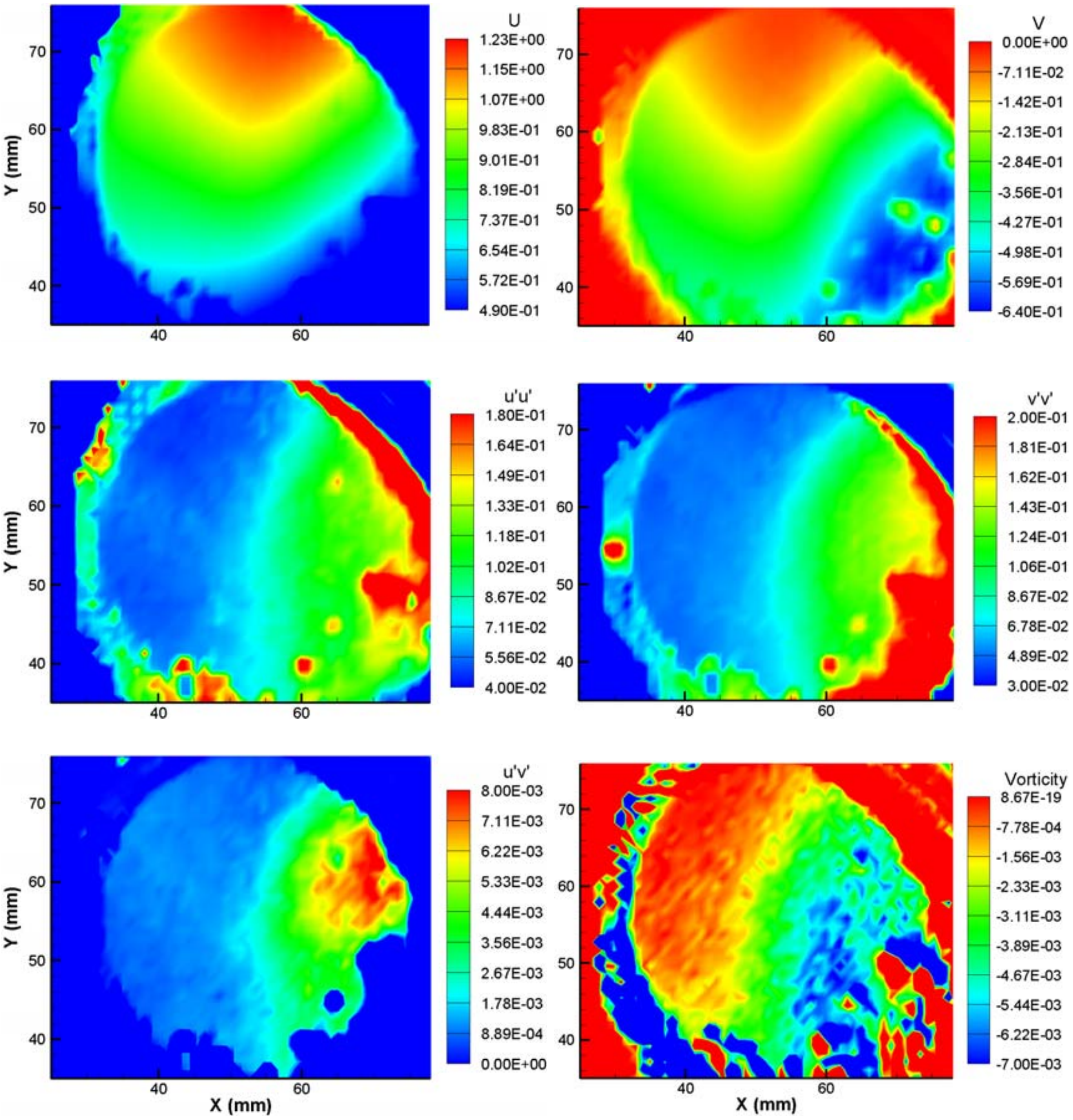

Figure 60: Location 13 Plane 14 Mean Velocities, Fluctuating Velocities, and Vorticity

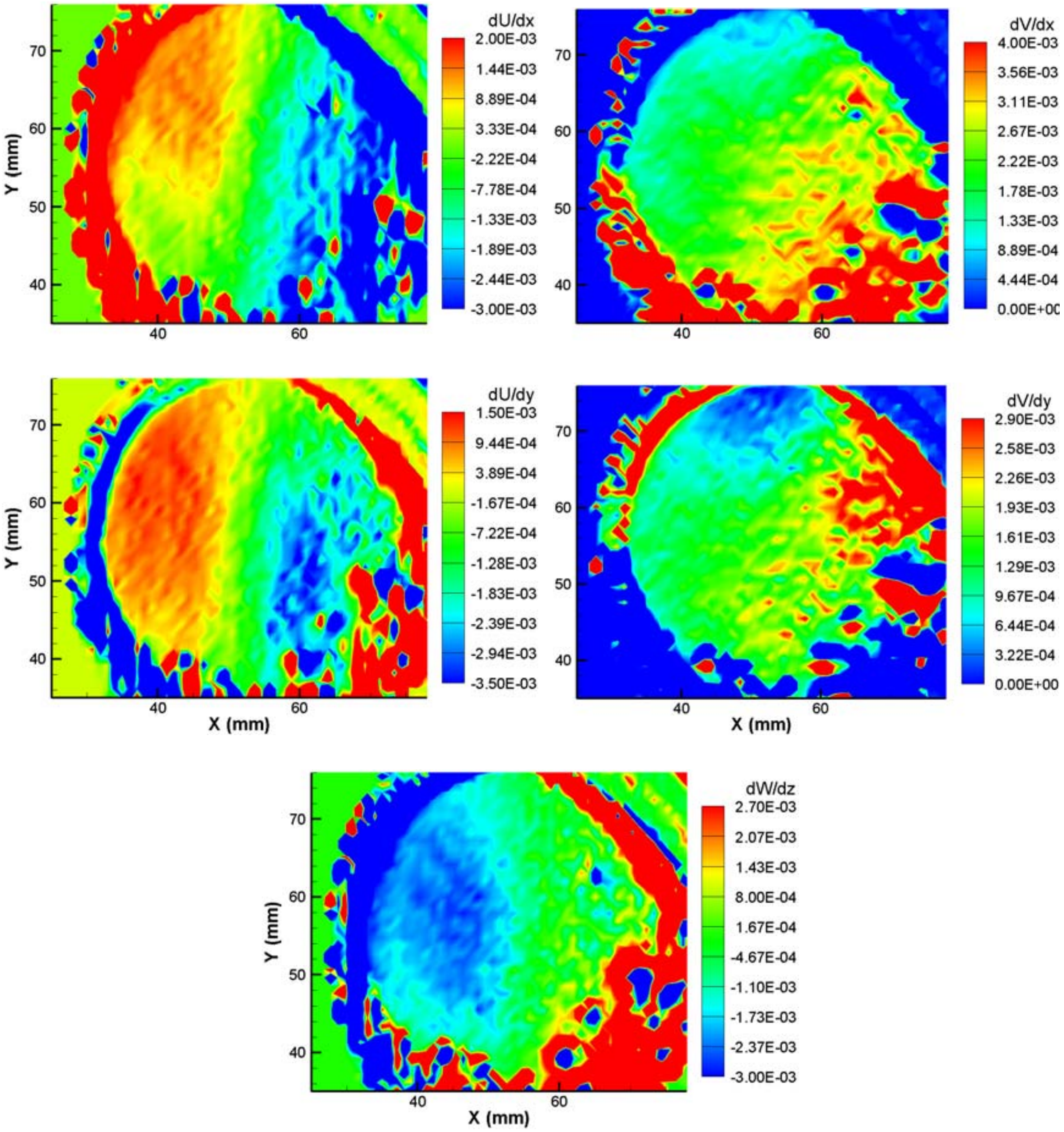

Figure 61: Location 13 Plane 14 Velocity Gradients

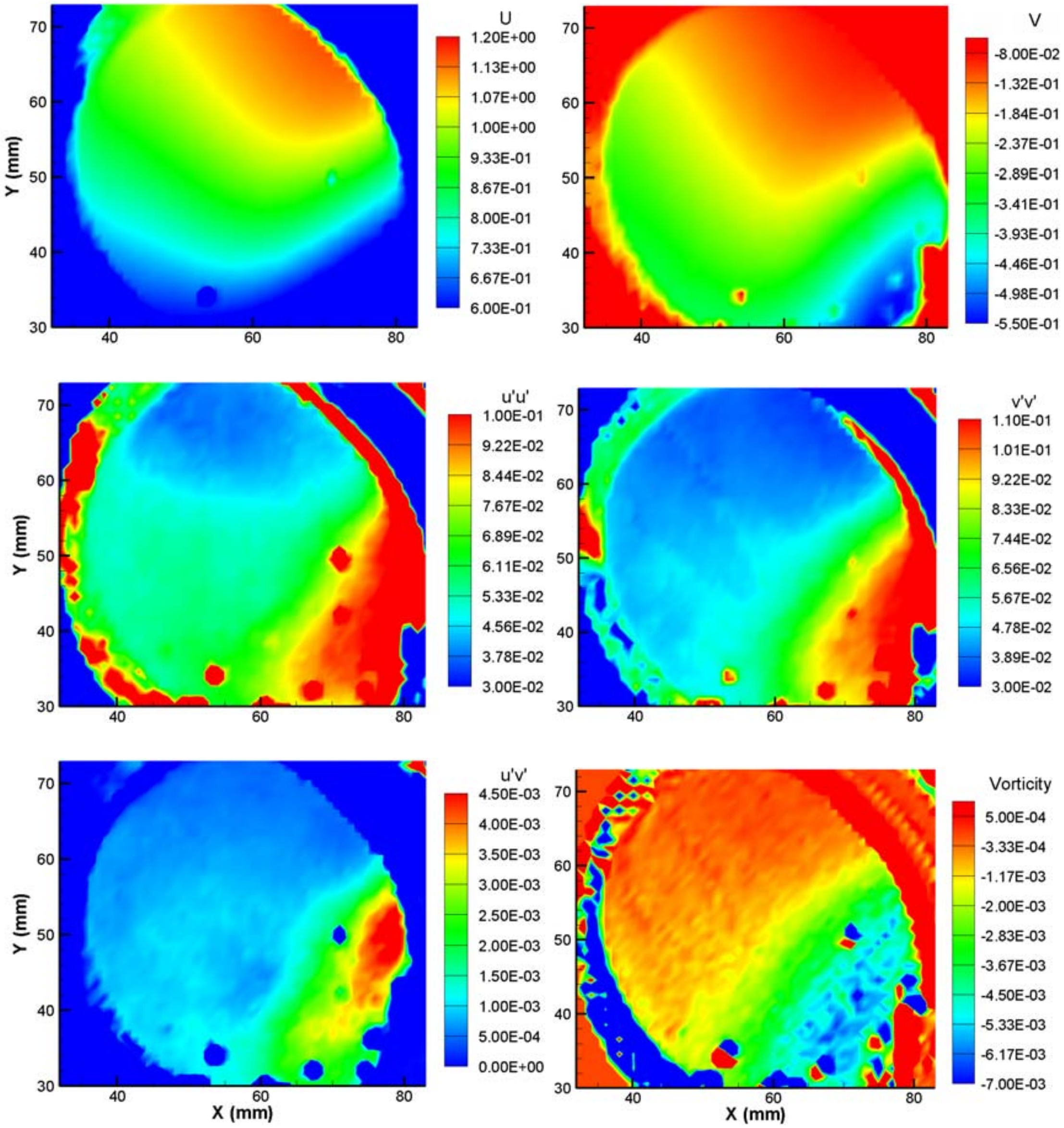

Figure 62: Location 13 Plane 15 Mean Velocities, Fluctuating Velocities, and Vorticity

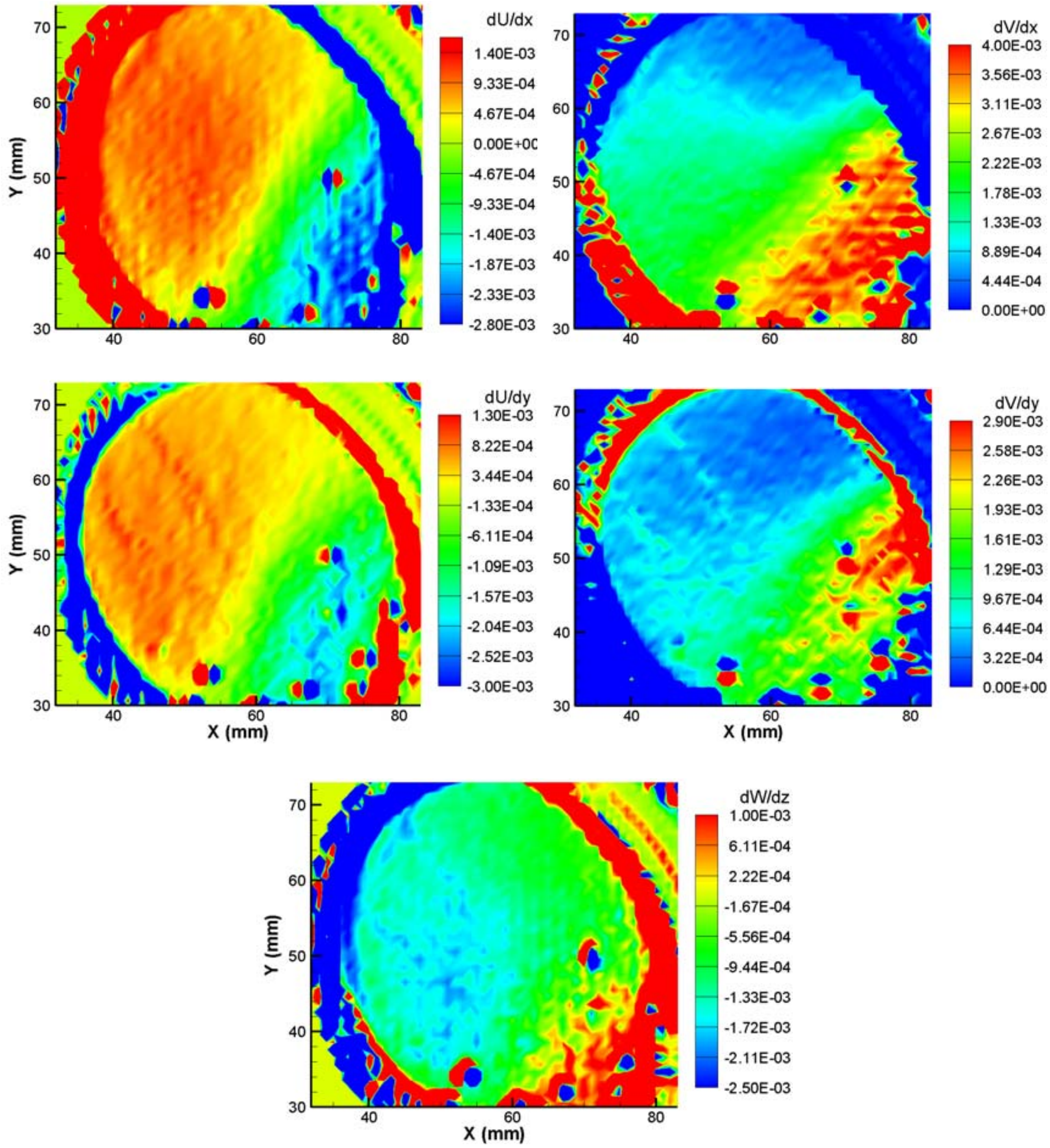

Figure 63: Location 13 Plane 15 Velocity Gradients

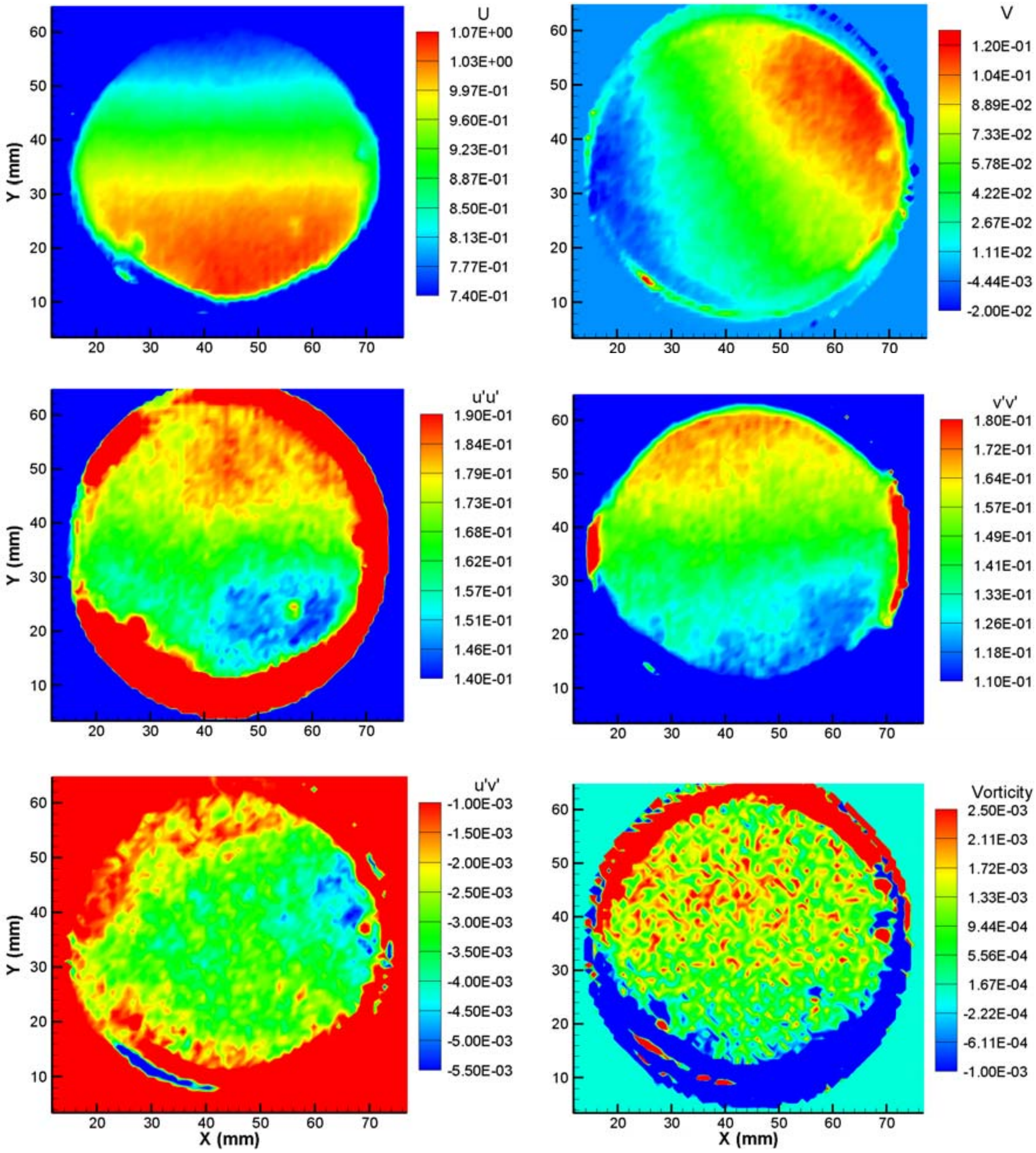

Figure 64: Location 14 Plane 12 Mean Velocities, Fluctuating Velocities, and Vorticity

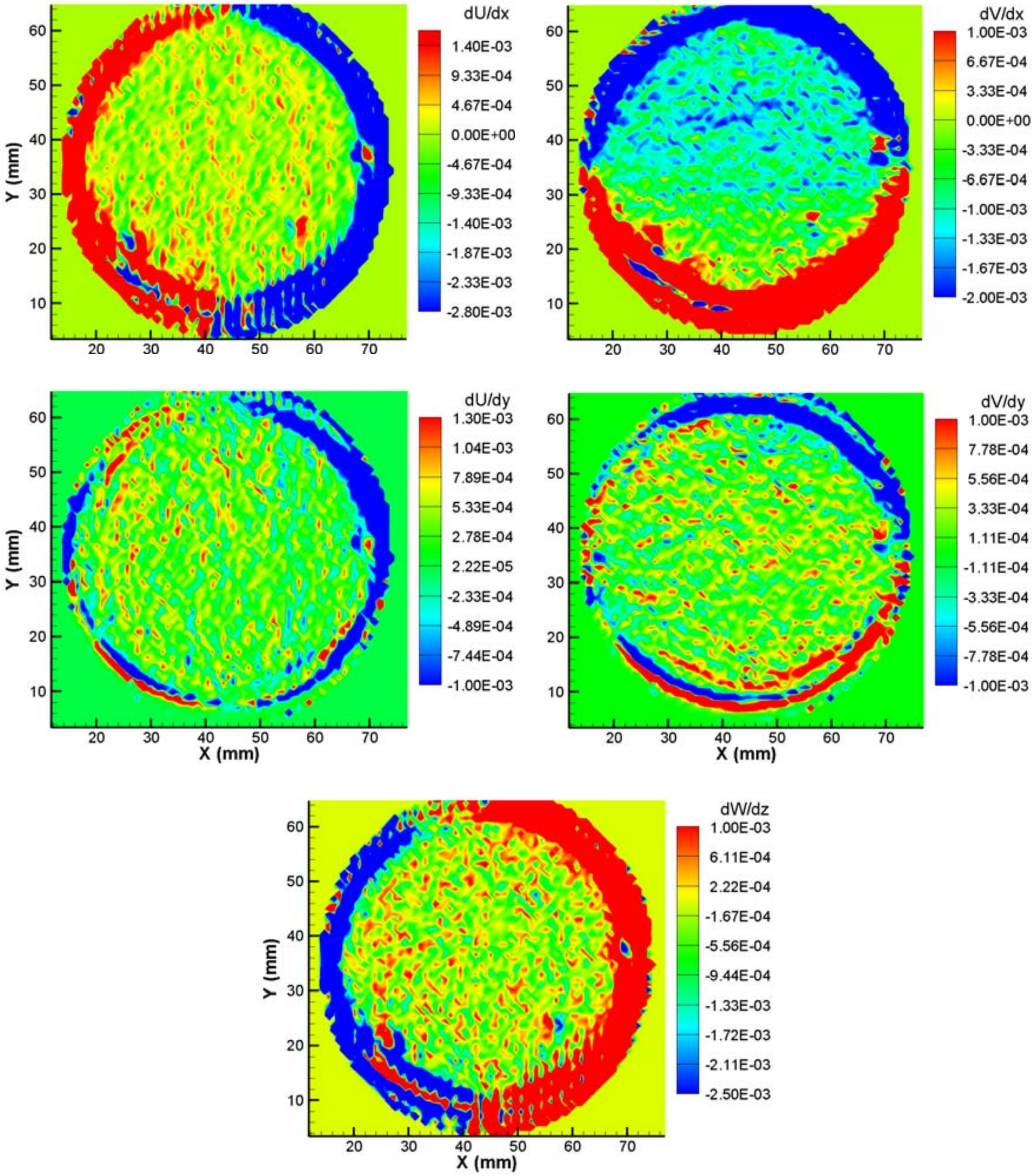

Figure 65: Location 14 Plane 12 Velocity Gradients

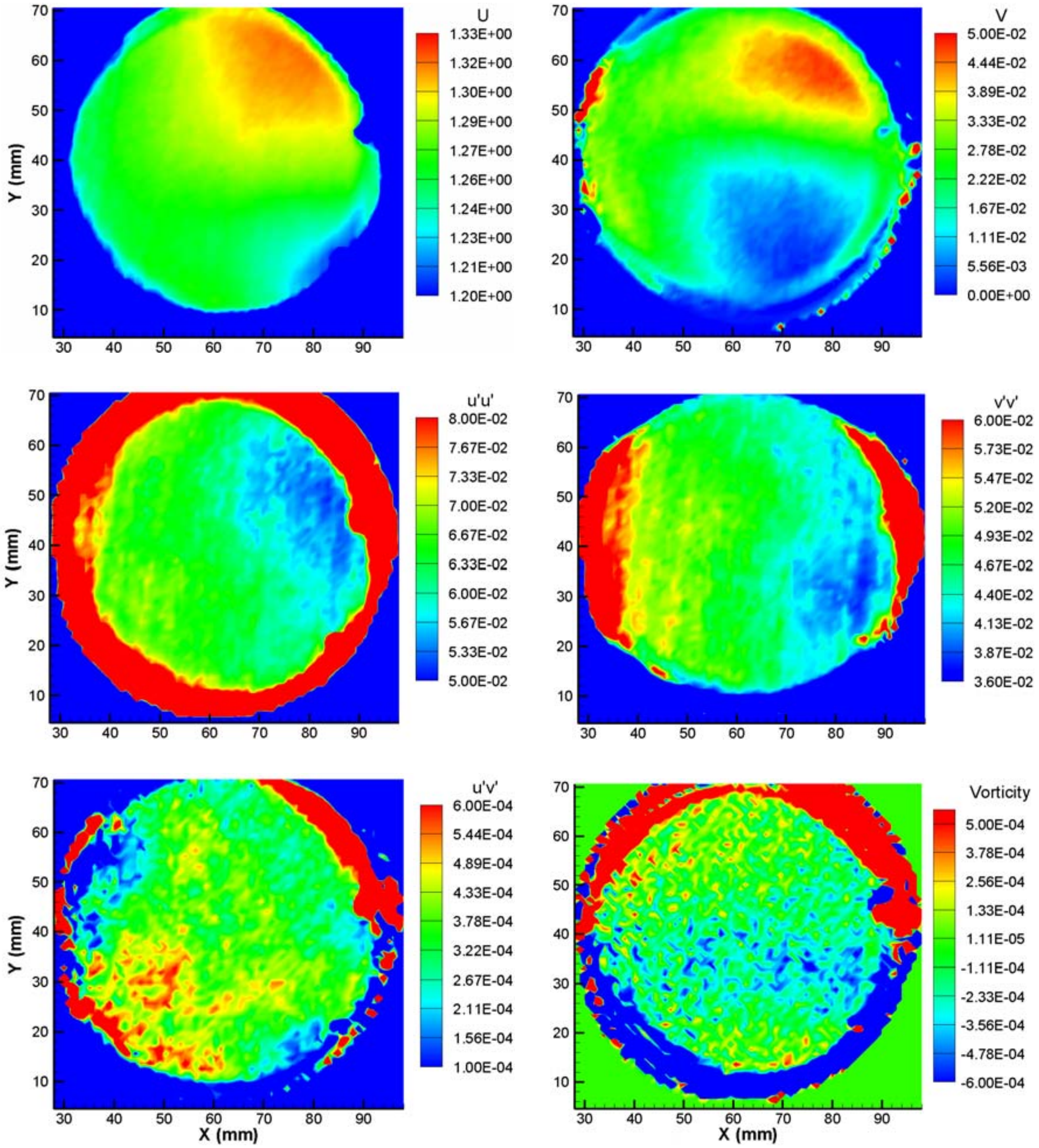

Figure 66: Location 14 Plane 13 Mean Velocities, Fluctuating Velocities, and Vorticity

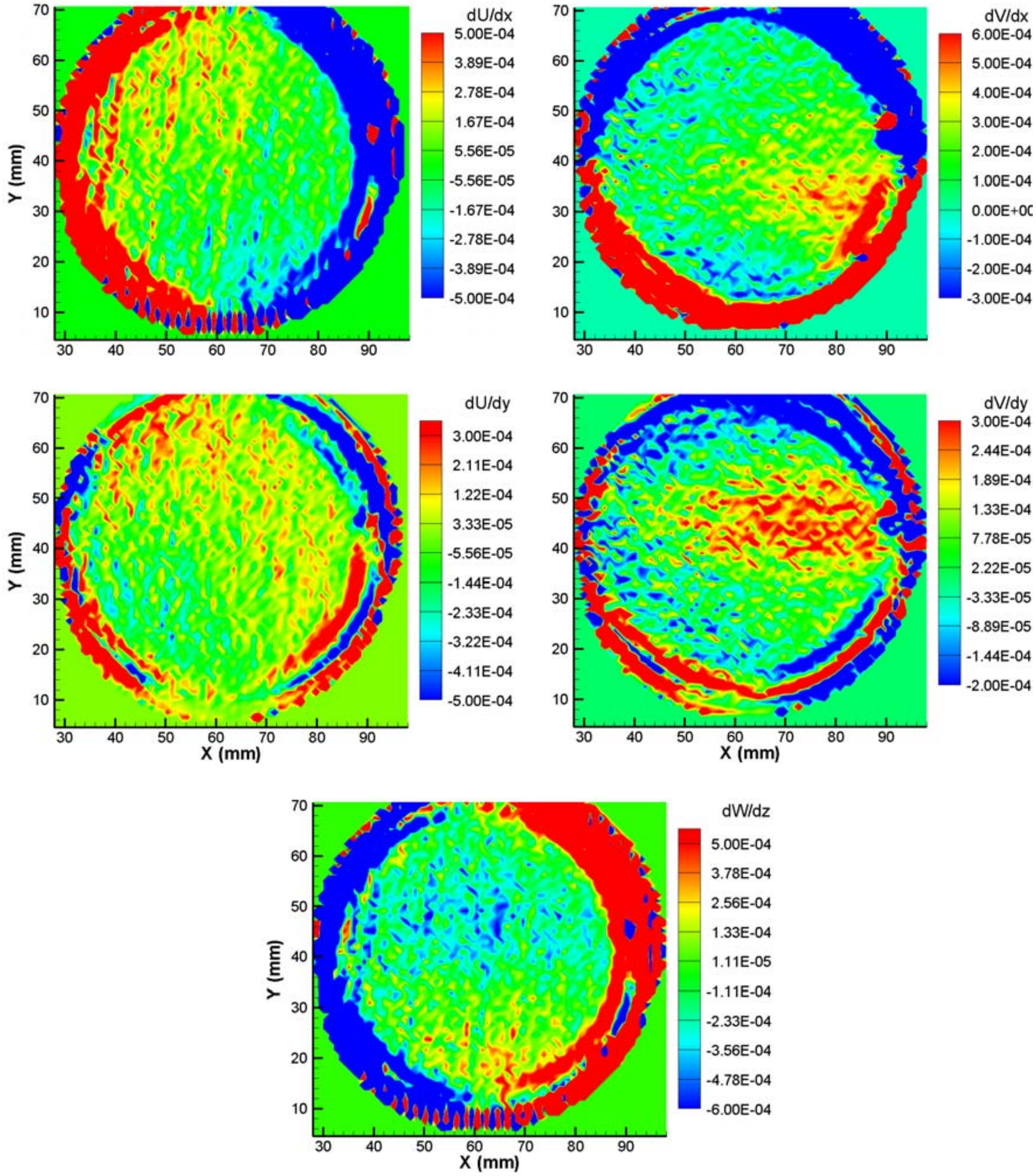

Figure 67: Location 14 Plane 13 Velocity Gradients

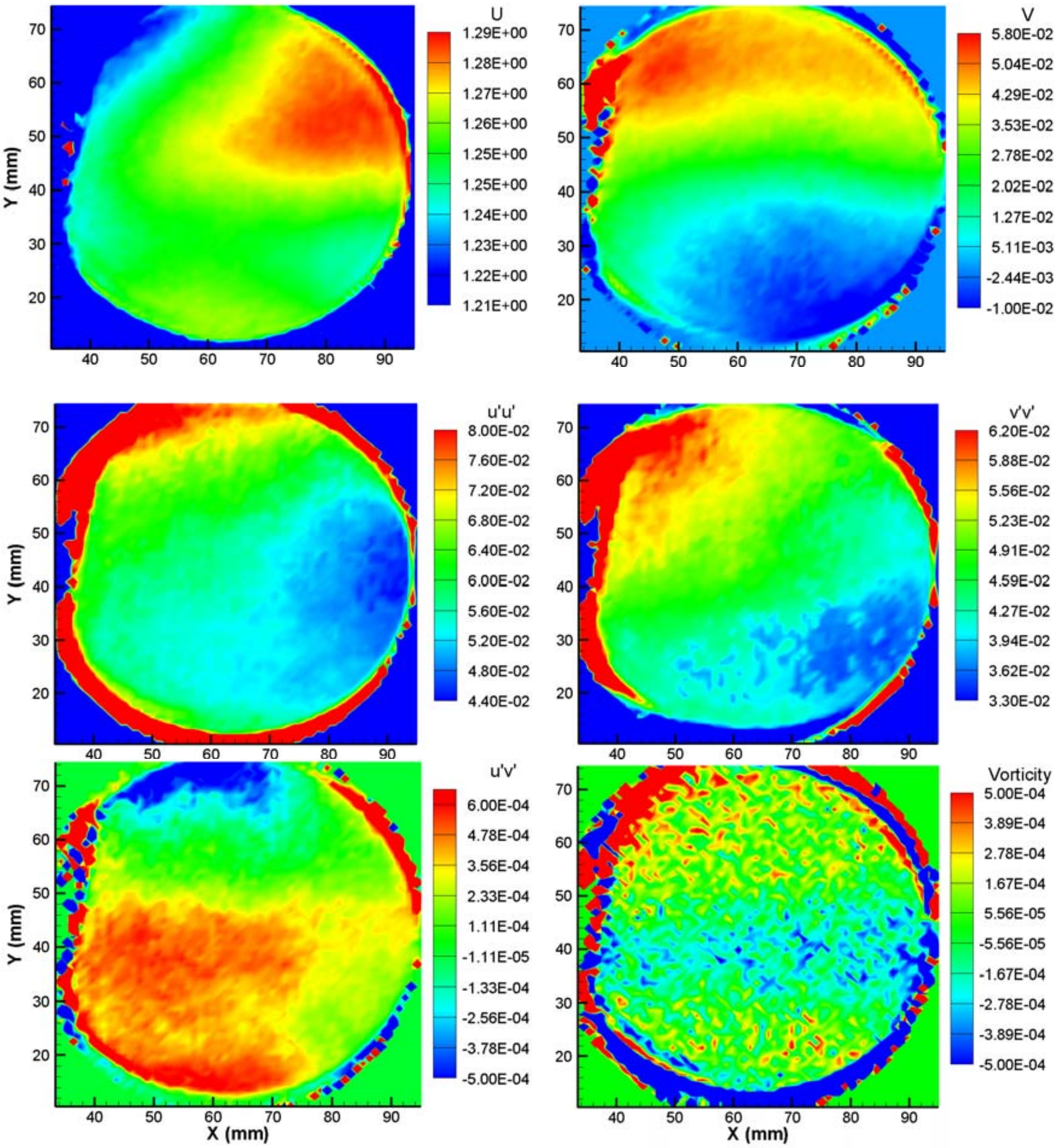

Figure 68: Location 14 Plane 14 Mean Velocities, Fluctuating Velocities, and Vorticity

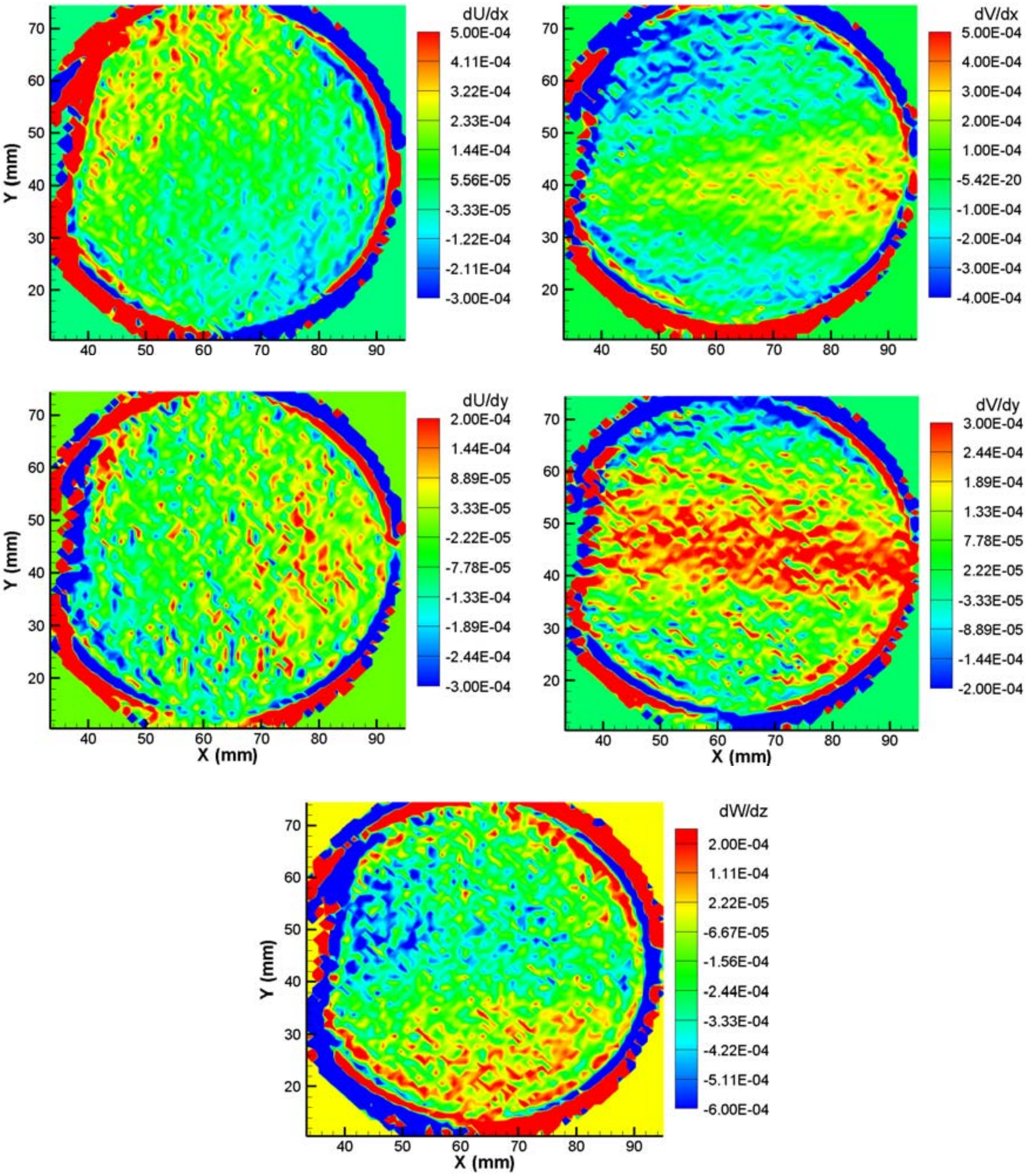

Figure 69: Location 14 Plane 14 Velocity Gradients

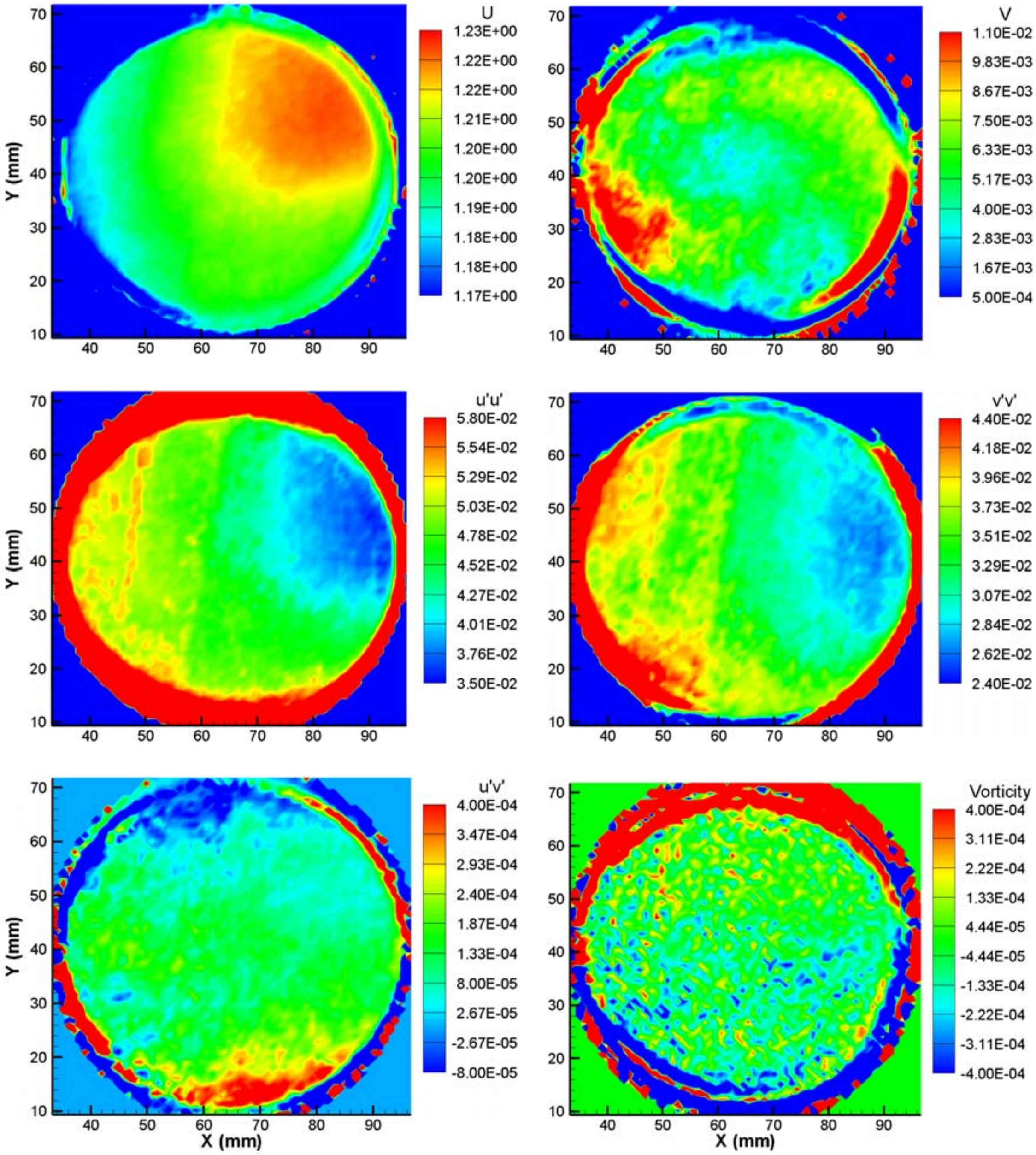

Figure 70: Location 14 Plane 15 Mean Velocities, Fluctuating Velocities, and Vorticity

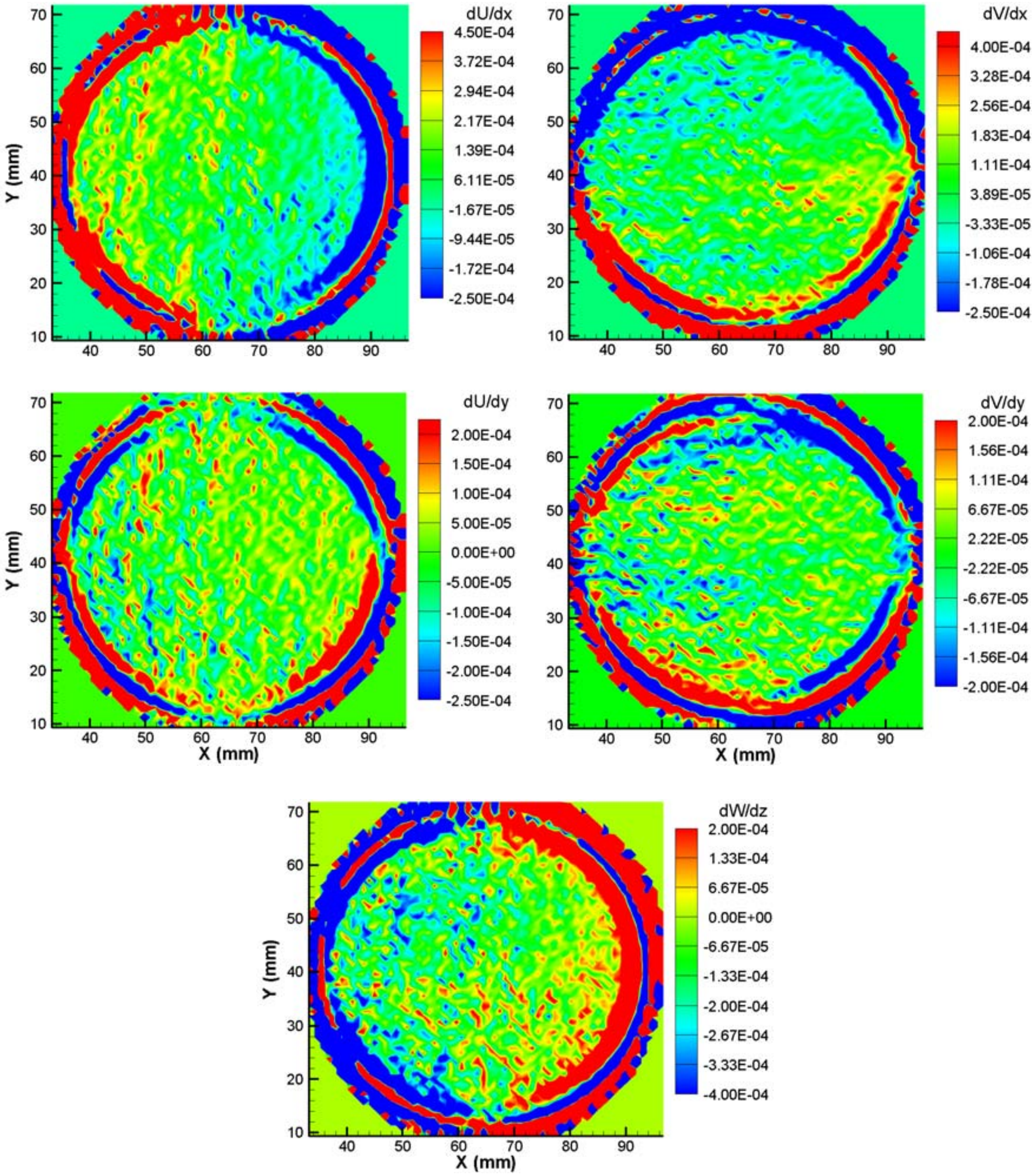

Figure 71: Location 14 Plane 15 Velocity Gradients

VITA

Name: Nathan Ryan Tichenor

Address: H.R. Bright Building, Rm. 701
3141 TAMU
College Station, TX 77843-3141

Education: B.S., Aerospace Engineering, Texas A&M University, 2005
M.S., Aerospace Engineering, Texas A&M University, 2007